Ulm University Medical Center
Department of Internal Medicine II
Head: Prof. Dr. W. Rottbauer

Tiny Golden Angles and Nonuniform Self-Gating: MRI of Nonuniform Motion

Dissertation

to obtain the Doctoral Degree
of Human Biology (Dr. biol. hum.)
of the Medical Faculty
of Ulm University

submitted by
Stefan Wundrak
born in Düren, Germany

2016

Acting Dean	:	Prof. Dr. rer. nat. Thomas Wirth
First Reviewer	:	Prof. Dr. rer. nat. Volker Rasche
Second Reviewer	:	Prof. Dr. rer. nat. Armin Nagel
Third Reviewer	:	Prof. Dr. sc. tech. Sebastian Kozerke
Date of Graduation	:	15.4.2016

Contents

Abbreviations

b-SSFP	fully balanced Steady State Free Precession.
BLAST	Broad-use Linear Acquisition Speed-up Technique.
CMR	Cardiovascular Magnetic Resonance.
DFT	Discrete Fourier Transform.
ECG	Electrocardiogram.
FFE-EPI	Fast Field Echo Echo-Planar Imaging.
FFT	Fast Fourier Transform.
FLASH	Fast Low Angle Shot Sequence.
GRASP	Golden Angle Radial Sparse Parallel MRI.
HASTE	Half Fourier Acquisition Single Shot Turbo Spin Echo.
HF	High Frequency.
IDFT	Inverse Discrete Fourier Transform.

MFISTA	Monotone Fast Iterative Shrinkage-Thresholding Algorithm.
MIP	Mutual Incoherence Property.
MR	Magnetic Resonance.
NUFFT	Nonuniform Fast Fourier Transform.
nuSG	Nonuniform Self-Gating.
PCA	Principal Component Analysis.
PD	Proton Density.
PINOT	Parallel Imaging and Noquist in Tandem.
RF	Radio Frequency.
RIP	Restricted Isometry Property.
ROI	Region Of Interest.
SENSE	Sensitivity Encoding.
SNR	Signal-to-Noise Ratio.
SSFP	Steady State Free Precession.
T1-FFE	T1 weighted Fast Field Echo.
TE	Echo Time.
TMJ	Temporomandibular Joint.
TR	Repetition Time.
TSENSE	SENSE with temporal filtering.
TV	Total Variation.
tyGRASP	tiny Golden Angle Radial Sparse Parallel MRI.

UNFOLD UNaliasing by Fourier-encoding the Overlaps in the temporaL Dimension.

Chapter 1

Introduction

1.1 Motivation and Aim of this Thesis

In this thesis, solutions to two previously unsolved problems in MR imaging of nonuniform motion will be proposed: first, the combination of golden angle ordering with b-SFFP sequences for real-time imaging, and second, the self-gated imaging of nonuniform motion. The advantages of the proposed methods will be shown for two clinical applications.

Cardiovascular MR

Cardiovascular magnetic resonance (CMR) has become the gold standard in the assessment of cardiac function [119]. To assess cardiac function in CMR, routinely a stack of short axis cine images (Figure 1) is acquired and evaluated for the left and right ventricular volume. The volume ejected by the heart during each stroke (stroke volume) is the difference of the volume of the contracted heart (end-systolic volume) and the volume of the relaxed heart (end-diastolic volume) [103]. The ejection fraction is calculated by dividing the stroke volume by the end-diastolic volume and is used to determine the severity of a systolic dysfunction, for instance due to congenital diseases, ischemia, or

myocarditis [103].

The standard MR acquisition protocol for functional CMR is a b-SSFP sequence [114] in combination with the ECG-gated cine method that partially records the data during several heart beats. This method requires however several seconds of patients' breath hold, and the gating method does not work in case of severe arrhythmia.

For this reason, radial real-time cine methods using the principles of compressed sensing were developed, that acquire the necessary data during a single heart beat [45]. However, the essential incoherent sampling trajectories require an abruptly changing gradient scheme. In combination with a b-SSFP sequence and its sensitive steady state this may lead to severe, eddy current induced image artifacts [14].

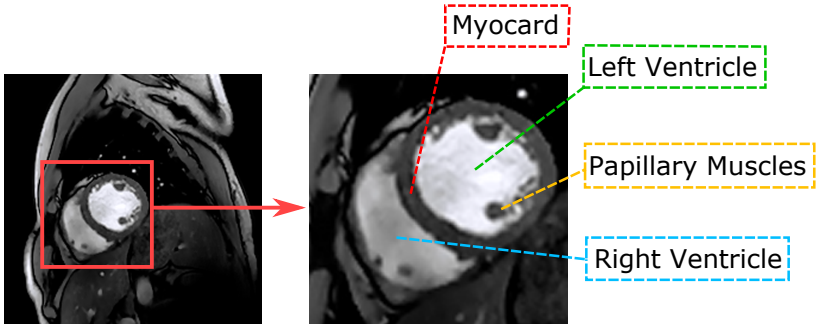

Figure 1: Magnetic resonance image of the human heart in short axis geometry, showing cross-sections of the left and right ventricle. The blood pool of the two ventricles appears bright, while the myocard and the papillary muscles appear dark. The image was acquired using a b-SSFP sequence (balanced Steady State Free Precession).

MRI of the Temporomandibular Joint

Assessment of the masticatory motion of the temporomandibular joint (TMJ) is of interest for a variety of pathologies, e.g. the intra-articular derangement of the articular disk. A major question during the assessment of the TMJ is therefore the dynamic relation of the discus articularis to the condyles and fossa mandibularis [118] (Figure 2).

Contrast of the articular disc to the surrounding tissue is mainly achieved due to the low T2 relaxation time of its fibrocartilagenous tissue [115]. Therefore, the preferred image sequence for dynamic imaging of the TMJ is the b-SFFP sequence due to its fast T2/T1 contrast [157].

Recently developed real-time cine methods allow the real-time imaging of the TMJ during its movement [60]. However, just as in CMR, the incoherent radial sampling trajectories lead to eddy current induced image artifacts in combination with the b-SSFP sequence [14, 153].

For CMR gated imaging still provides higher image quality in terms of SNR and temporal resolution than real-time imaging. However, the nonuniform and non reproducible motion of the TMJ prevented the use of gated imaging so far.

In this thesis, solutions to both problems will be proposed: a golden angle real-time cine method that does not affect the steady state of the b-SSFP sequence, and a self-gated method that works even in the case of nonuniform motion such as severe cardiac arrhythmia or the moving TMJ.

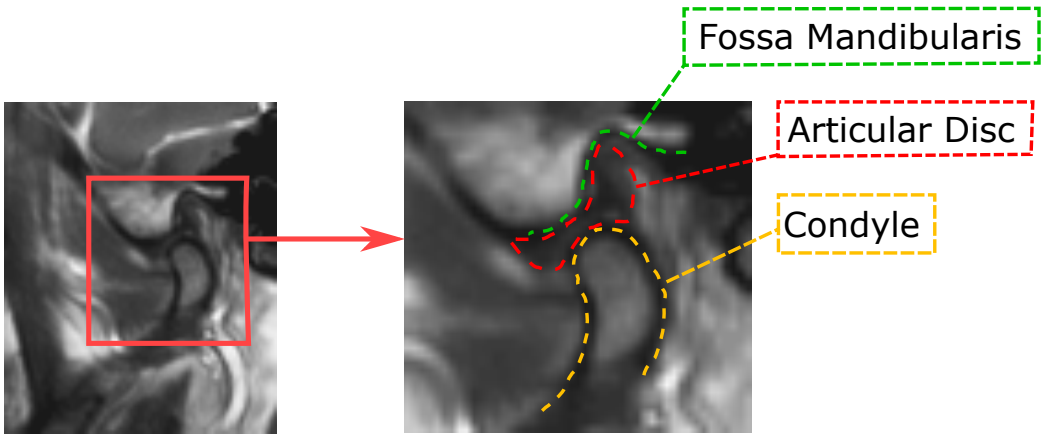

Figure 2: Parasagittal magnetic resonance image showing the anatomy of the temporomandibular joint. The articular disc between the condyle and the fossa mandibularis appears dark due to the low T2 relaxation time of its fibrocartilagenous tissue [115] and the T2/T1 image contrast of the b-SSFP sequence (balanced Steady State Free Precession).

1.2 Thesis Outline

Chapter 2 gives a brief introduction to magnetic resonance imaging and the fundamental techniques this work is based on, as well as a short introduction to CMR and TMJ imaging.

Chapters 3 gives a short summary of the methods used in this work.

Chapters 4 to 6 contain the reprinted journal articles.

In Chapter 4 the new tiny golden angle profile ordering is proposed that has similar optimal properties as the golden angle ordering but with a smaller angular increment and therefore allows the combination of golden angle ordering with b-SSFP sequences.

In Chapter 5 it is shown that the new tiny golden angles enable sparse and parallel imaging using the *golden angle radial sparse parallel MRI* (GRASP) technique and the new tyGRASP method is proposed.

In Chapter 6 a new self-gating method is introduced, that solves the problem of gated imaging of nonuniform motion, in particular for cardiac arrhythmia and motion of the TMJ.

Chapter 7 summarizes the results of the reprinted publications and Chapter 8 discusses the results and gives a conclusion.

Chapter 2

Background

This chapter gives a very compact introduction from MRI physics to practical MRI imaging. A detailed introduction can be found in [13], [18] and [42], which are also used as base references for this chapter. Even though nuclear magnetic resonance describes a quantum mechanical phenomenon, it can be described accurately using classical mechanics if a large number of protons is considered [123]. The following will only consider and start with the classical descriptions of nuclear magnetic resonance.

2.1 Magnetic Resonance Imaging

2.1.1 Bloch Equations

The signal that is used to create image contrast in magnetic resonance imaging comes from protons, dominantly water molecules. The protons of one spin-ensemble are polarized along a strong magnetic field $\vec{B_0} = (0, 0, B_0)^T$ (vector in z-direction), which leads to a steady state magnetization $\vec{M_0} = (0, 0, M_0)^T$ oriented in the direction of $\vec{B_0}$. The Bloch equations describe the magnetization vector $\vec{M} = (M_x, M_y, M_z)^T$ as a function of time

$$\frac{d\vec{M}(t)}{dt} = \vec{M}(t) \times \gamma\vec{B}(t) - \left(\frac{M_x(t)}{T2}, \frac{M_y(t)}{T2}, \frac{M_z(t) - M_0}{T1}\right), \tag{2.1}$$

where the magnetic field is usually described as $\vec{B}(t) = \vec{B}_G(t) + \vec{B}_0$ with the static main field $\vec{B}_0$ and a time dependent magnetic field $\vec{B}_G(t)$. The first term describes the precession of the nuclear magnetization $\vec{M}$ dependent on the gyromagnetic ratio, $\gamma = 42.56 Mhz/Tesla$ for hydrogen.

The second term is the relaxation term, that models the longitudinal and transverse relaxation. The longitudinal relaxation is described by the tissue specific parameter $T1$, with M_z being the nuclear magnetization in z-dimension. The transverse relaxation is described by the tissue specific parameter $T2$.

The precession frequency, or Larmor frequency, $\omega_0 = \gamma B_0$, that is only dependent on the strength of the main magnetic field B_0 follows directly from the first term of eq. 2.1.

To move the magnetization $\vec{M}$ out of the steady state, a magnetic field $\vec{B}_1$ that rotates at the Larmor frequency perpendicular to $\vec{B}_0$ is used. The force induced by $\vec{B}_1$ lets $\vec{M}$ spiral out of the z-direction towards the xy-plane. The tip angle α between $\vec{M}$ and the z-axis is defined by the strength and duration of the $\vec{B}_1$ field. When the $\vec{B}_1$ field is turned off, the magnetization vector $\vec{M}$ continues to precess and starts to relax towards its steady state along $\vec{B}_0$ and the magnitude M_0. In case of an $\alpha = 90°$ tip angle, the longitudinal and transverse relaxation of the magnetization (Figure 3) can be derived directly from the Bloch equations as (2.1):

$$M_z(t) = M_0(1 - e^{-t/T1})$$
$$M_{xy}(t) = M_0 e^{-t/T2}$$

The magnetization vector $\vec{M}$ precesses at the Larmor frequency and emits an electromagnetic signal whose strength is proportional to the current transverse magnetization

$M_{xy}(t)$. The decay of this signal is specific to the tissue dependent parameters $T1$ and $T2$, and is the main source of contrast between tissues in magnetic resonance imaging.

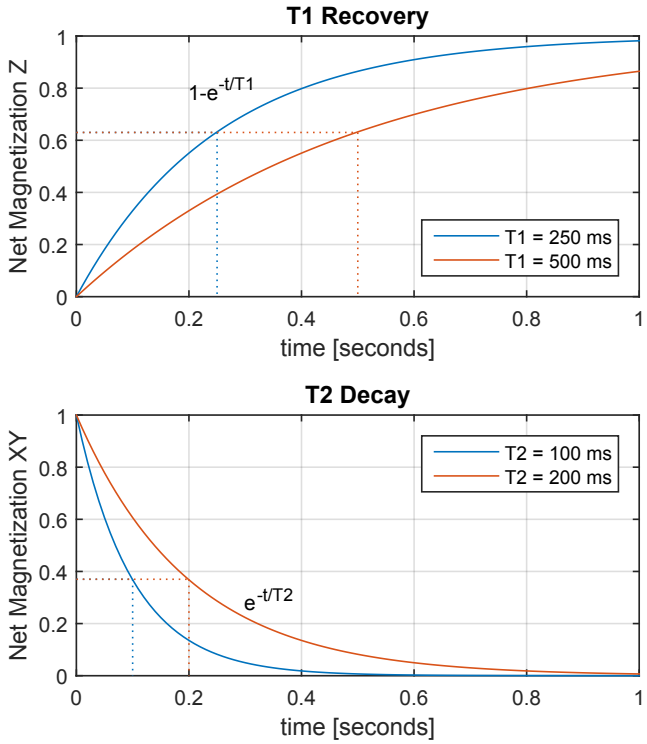

Figure 3: Magnetization relaxation curves showing T1 recovery and T2 decay. The T1 and T2 values are tissue specific properties describing the longitudinal and transverse relaxation of the magnetization. Since the magnetization relaxes exponentially, the relaxation function can be fully described using a single time constant that is defined at the point where $1 - 1/e = 63.2\%$ has been recovered or $1/e = 36.8\%$ has been decayed (dotted lines).

2.1.2 Spatial Encoding

Gradient coils are used to create a linear field gradient [13, p.215]

$$\vec{G} = \frac{dB_z}{dx}\vec{e}_x + \frac{dB_z}{dy}\vec{e}_y + \frac{dB_z}{dz}\vec{e}_z = (G_x, G_y, G_z)^T \tag{2.2}$$

where $(\vec{e}_x, \vec{e}_y, \vec{e}_z)$ is the canonical basis of the Cartesian coordinate system. The field gradient results in a locally variable magnetic field $\vec{B}_G(r) = \vec{G} \cdot \vec{r}\vec{e}_z$ that specifies a spatial variation of the z-component of the magnetic field for each location $\vec{r} = (x, y, z)^T$. $\vec{B}_G$ is superimposed on the magnetic field $\vec{B}_0$ and locally changes the Larmor frequency which allows spatial encoding of the excitation and the received signal (Figure 4). The spatial encoding is done in two steps. First, the preselection of a subvolume, and second, the 2D or 3D spatial encoding of this subvolume.

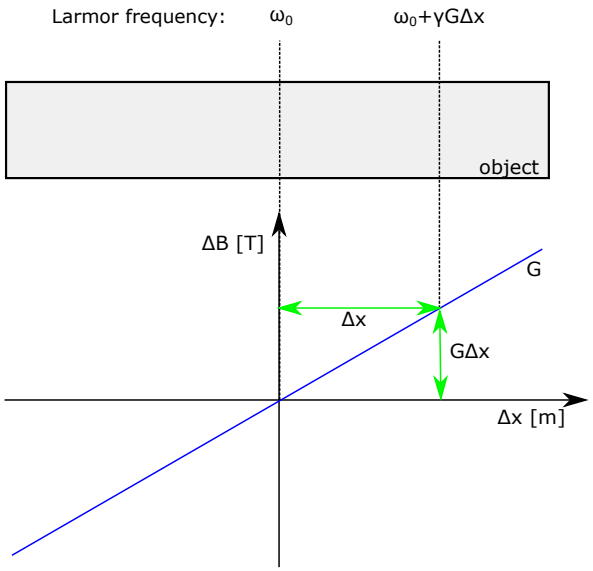

Figure 4: Superimposed field gradient G locally changes the magnetic field B and therefore the Larmor frequency ω in an object dependent on the location x (one-dimensional case). Here ω_0 is the base frequency, $\gamma G \Delta x$ describes the frequency offset caused by the field gradient G, and γ the gyromagnetic ratio. This principle is used for spatial encoding by the slice selection gradient, the frequency encoding gradient, and the phase encoding gradient.

Slice Selection Gradient

A bandwidth limited RF pulse, using a *sinc*-shaped envelope, in combination with a linear field gradient G_z, excites only protons that precess within the range of Larmor

frequencies defined by the bandwidth of the excitation pulse. This allows the selective excitation of a subvolume (or slab) of the object.

Frequency Encoding Gradient

Superimposing a linear gradient G_x in x-direction leads to a spatially varying precessing frequency difference to ω_0 of

$$\omega(x) = \gamma G_x x. \tag{2.3}$$

Applying this gradient during the read-out leads to a controlled dephasing along the x-axis. The phase at location x and time t is described by

$$\phi(x,t) = \int_0^t \omega(x,\tau)d\tau = \gamma \int_0^t G_x(\tau)x d\tau. \tag{2.4}$$

Usually, the k-space notation is used, which normalizes the time t to the substitute k_x using

$$k_x = \gamma \int_0^t G_x(\tau)d\tau, \tag{2.5}$$

which reduces equation (2.4) in k-space notation to

$$\phi(x,k_x) = k_x x. \tag{2.6}$$

The receiver coil integrates the signal of all locations x of the objects transverse magnetization $m(x) = M_{xy}(x)$ which leads with the phase shifts from equation (2.6) to the complex one dimensional signal equation

$$s(k_x) = \int_{FOV} m(x)e^{-i2\pi k_x x}dx, \tag{2.7}$$

where FOV is the field of view.

Phase Encoding Gradient

The encoding of the second dimension y is very similar to the frequency encoding, except this time the gradient G_y is applied for a short time span T after excitation which leads to a controlled dephasing along the y-axis. Analog to the equations 2.4 to 2.6, using T instead of t (and k_y instead of k_x) one derives

$$s(k_y) = \int_{FOV} m(r) e^{-i2\pi k_y y} dy, \tag{2.8}$$

with the only difference that k_y is this time constant during readout and only a single phase shift will be acquire during each readout. As a consequence, the readout has to be repeated many times in order to acquire the signal for different values of k_y.

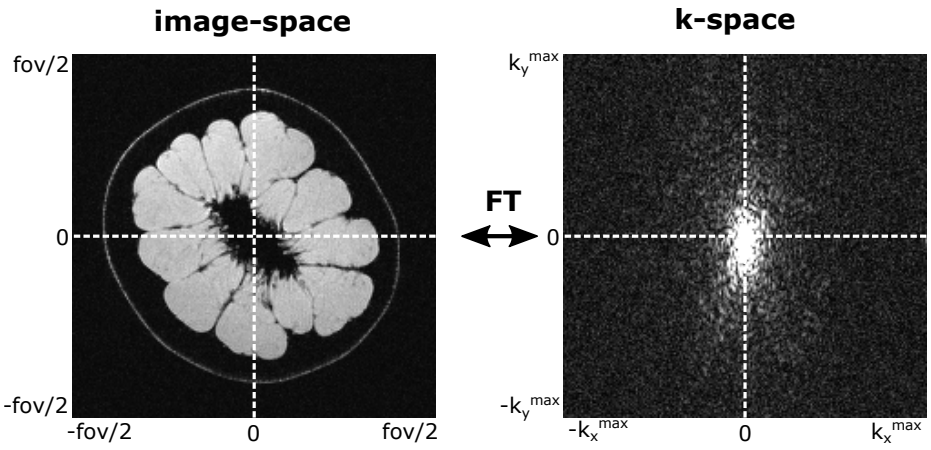

Figure 5: K-space and image-space are dual to each other by the Fourier transform (FT). That means, the signal in k-space equals the distribution of the transverse magnetization (image) in the spatial domain. Abbreviations: field-of-view (fov).

K-Space

Frequency encoding and phase encoding are independent from each other if the encoding directions are orthogonal and may be combined. This leads with $\vec{k} = (k_x, k_y)$, or more

general $\vec{k} = (k_x, k_y, k_z)$, to the more dimensional signal equation

$$s(\vec{k}) = \int_{FOV} m(\vec{r}) e^{-i2\pi\vec{k}\vec{r}} d\vec{r}. \tag{2.9}$$

This equation, which denotes the k-space, is equivalent to the n-dimensional Fourier transform. Therefore, the signal s in k-space equals the distribution of the transverse magnetization m in the spatial domain (Figure 5).

$$s(\vec{k}) \overset{FT}{\Leftrightarrow} m(\vec{r}). \tag{2.10}$$

As a consequence, in the discrete case the distribution of the transverse magnetization (or image) m can be reconstructed from the signal s by applying a fast Fourier transform (FFT), presuming the k-space was fully sampled at the Nyquist rate.

2.1.3 Image Sequences

A vast number of MRI sequences exists. The following focuses on the sequences which are relevant for the core of this work and assumes that basic MRI sequences are already known by the reader. For a detailed overview of MR sequences see [13].

Gradient Echo

In gradient echo sequences spins are dephased using a prephasing gradient and then refocused by a frequency encoding gradient to form an echo (Figure 6). During gradient echo sequences typically small flip angles are used. Therefore, no lengthy period is needed for T_1 recovery [13, p. 580] and a short TR may be used which makes this class of sequences well suited for dynamic imaging [56].

If the transverse magnetization reaches zero before the next RF pulse is applied, the sequence is called a spoiled gradient echo. Spoiling of the transverse magnetization is done by by applying an additional gradient spoiler and often supplemented by phase

cycling the RF-pulse. The spoiled gradient echo sequence shown in Figure 6 is called FLASH [56] or T1-FFE, due to the T1-weighted contrast of this sequence. Spoiled gradient echo sequences are well suited for real-time imaging [135].

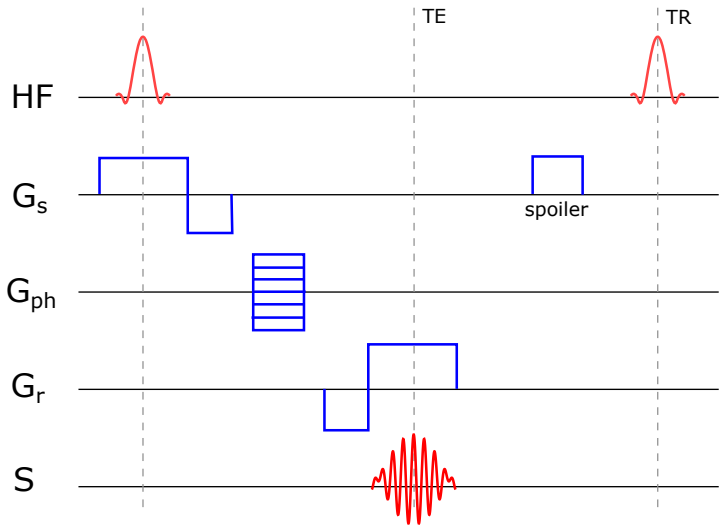

Figure 6: Sequence diagram of a spoiled gradient echo sequence. The HF pulse tips the net magnetization out of alignment with the main magnetic field (red, top row). The slice selection gradient selects a slab or volume in space (row G_s, left). The phase encoding gradient encodes one spatial dimension (row G_{ph}). The spins are dephased using a prephasing gradient and then refocused by a frequency encoding gradient to form an echo (rows G_r and S). A spoiler gradient after each echo is used to spoil the remaining transverse magnetization. Abbreviations: high frequency (HF), slice selection gradient (G_S), phase encoding gradients (G_{ph}), read-out gradient (G_r), signal (S), echo time (TE), repetition time (TR), see [13].

Balanced SSFP

If the transverse magnetization is not spoiled and non-zero before each excitation pulse, and reaches a steady state, the sequence is called *steady state free precession* (SSFP). Since SSFP sequences use a combination of pulses over several TR, additional echos, called Hahn echos [57], are formed. For this reason, SSFP sequences may form complex spin trajectories whose analysis is beyond the scope of this work.

Balanced SSFP sequences [90] are SSFP sequences where the integral of switched gradient pulses equals zero over TR. The difference to a non-balanced SSFP sequence is shown in Figure 7. Due to the fully balanced gradients, dephasing and rephasing just cancel each other (under ideal conditions) which means that just before the following RF-pulse the spins are fully focused again into a single magnetization vector. In total, it appears as if only relaxation effects affected the magnetization vector between the two RF-Pulses. In particular, at $TE = TR/2$ the field inhomogeneity-induced phases are nearly completely refocused [114]. Therefore, the steady state contrast depends mainly on $T2$ instead of $T2^*$, in contrast to other gradient echo sequences. The signal equation is [114]

$$M_S = M_0 \frac{\sin\alpha}{1 + cos\alpha + (1 - cos\alpha)(T1/T2)} e^{-TE/T2};\ TR \ll T1, T2. \tag{2.11}$$

For an optimal flip angle α the signal approaches $M_S = \frac{1}{2} M_0 \sqrt{T2/T1}$ and if $T1 \approx T2$ the maximum signal is close to 50% of M_0. This is why the b-SSFP sequence results in the best signal-to-noise ratio per time of all known sequences.

On the downside, the steady state of the b-SSFP sequence is very sensitive to off-resonances. A relative off-resonance of v (Hz) results in a dephasing of $\theta = 2\pi v TR$ within TR and thus the magnetization vector rotates by θ around the z-axis during two excitation pulses. In fact, the dephasing starts at an angle of $\theta/2$ from the x-axis and ends at $-\theta/2$, and the magnetization is refocused during the echo at $TE = TR/2$ [114]. Figure 8 plots the signal in relation to the phase offset and shows that the signal suddenly breaks down if the dephasing is near $\theta = \pi$. Thus, the image may exhibit sudden signal drops that typically manifest as dark-banding artifacts, where the location of the bands depends on the local shim.

In addition to the static homogeneity of the magnetic field, the b-SSFP sequence is also very sensitive to eddy current induced inhomogeneities. In particular, the permanently and abruptly changing gradient scheme of non-linear phase encoding schemes [14] or due to the large angular increment of golden angle radial acquisition schemes [152] leads to

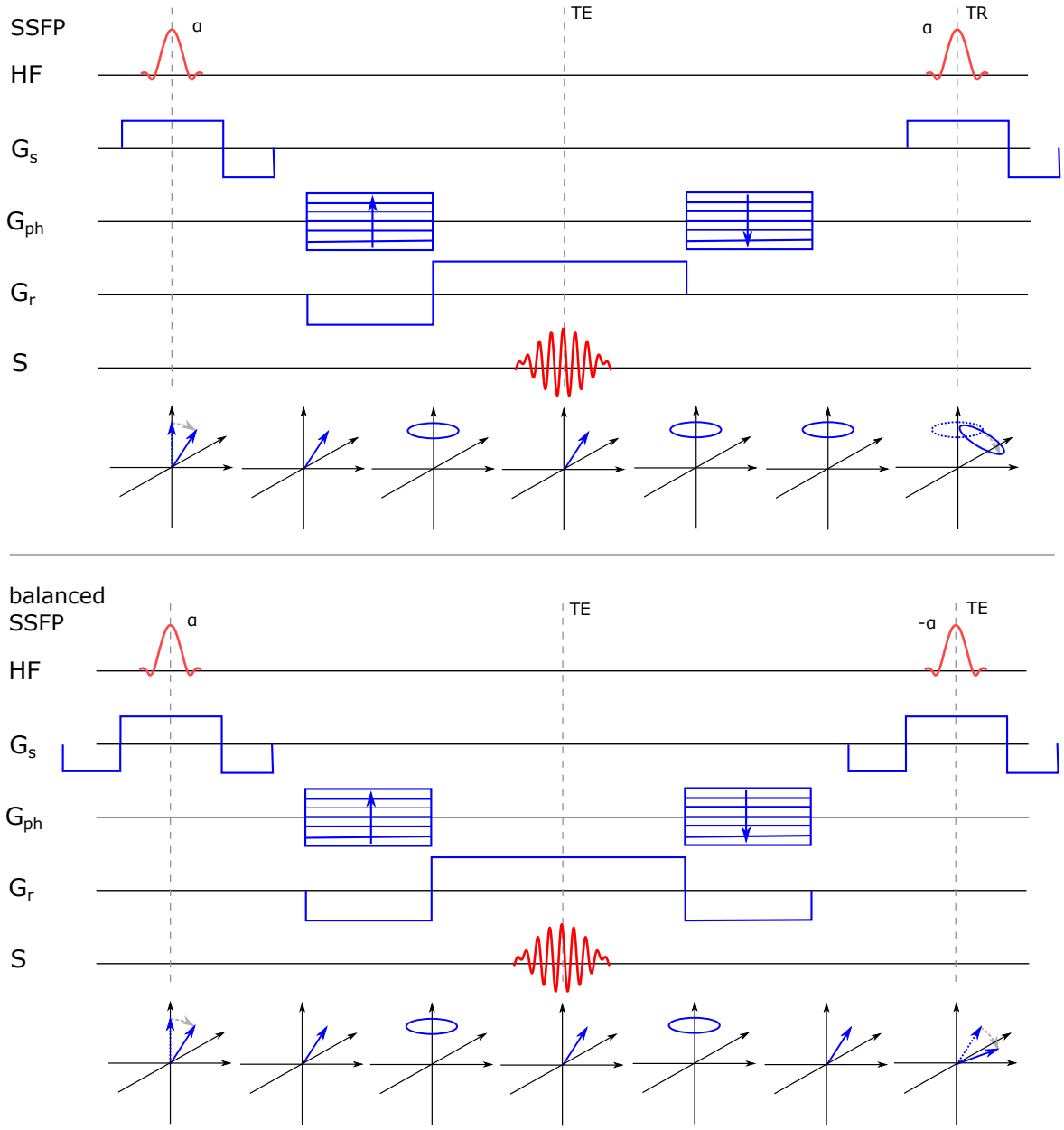

Figure 7: Steady state free precession (SSFP) and fully balanced SSFP sequence and their associated evolution of the net magnetization (bottom). For SSFP the the readout-gradient (row G_r) is not balanced, resulting in a dephased magnetization at the time of the second HF pulse [114]. For the balanced SSFP sequence all three gradients (G_s, G_{ph}, and G_r) are fully balanced, which leads, under ideal conditions, to a single magnetization vector at the time of the second HF pulse. Abbreviations: high frequency (HF), slice selection gradient (G_S), phase encoding gradients (G_{ph}), read-out gradient (G_r), signal (S), echo time (TE), repetition time (TR), see [114].

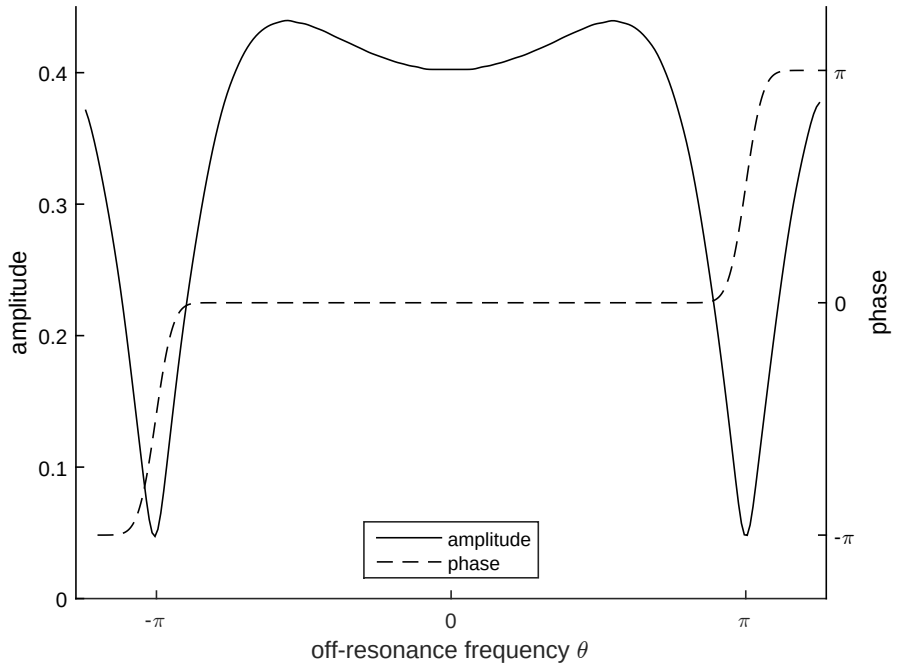

Figure 8: Steady state signal amplitude and phase for a b-SSFP sequence at TE = TR/2 in relation to the phase offset $\theta = 2\pi vTR$ between two pulses due to an off-resonance frequency v. A strong signal loss appears if the dephasing is near π, leading to the characteristic banding artifacts of b-SSFP sequences. Abbreviations: balanced steady State Free Precession (b-SSFP), echo time (TE), repetition time (TR). See [114].

rapidly changing eddy currents in the conducting part of the magnet, and in turn to rapidly varying field inhomogeneities. This usually leads to strong signal fluctuations and strong image artifacts [14].

2.2 Radial Imaging

Cartesian k-space trajectories use a combination of frequency- and phase-encoding to sample the k-space on a Cartesian grid. Beside Cartesian k-space sampling trajectories also non-Cartesian sampling trajectories are used. The most prominent examples are spiral trajectories [16], and radial trajectories [72]. This work focuses on the use of radial trajectories due to its beneficial features regarding motion and aliasing artifacts [111]. In radial MRI the k-space is sampled with a set of radial profiles traversing the k-space center.

The resulting sampling pattern shows a decreasing sampling density with increasing distance to the k-space center. In particular, k_0 is sampled during each readout (Figure 9) and the surrounding of the k-space center is strongly oversampled.

For radial trajectories, two or three frequency encoding gradients in x-, y-, and z-direction are superimposed to generate a single frequency encoding gradient with an arbitrary orientation [72, 111], which equals the angle of the associated radial k-space profile. No phase encoding gradient is used. In the two-dimensional case, for a Nyquist coverage of the high frequencies $N = \pi/2 \cdot d$ radial profiles are needed (if the profiles are spaced uniformly), where d is the diameter of the field-of-view in pixels. Even though nominally more sample points are needed than for a Cartesian trajectory of the same resolution, radial trajectories are robust to a certain degree of undersampling and in practice a sampling density below the Nyquist rate is used, e.g. $N = d$ profiles.

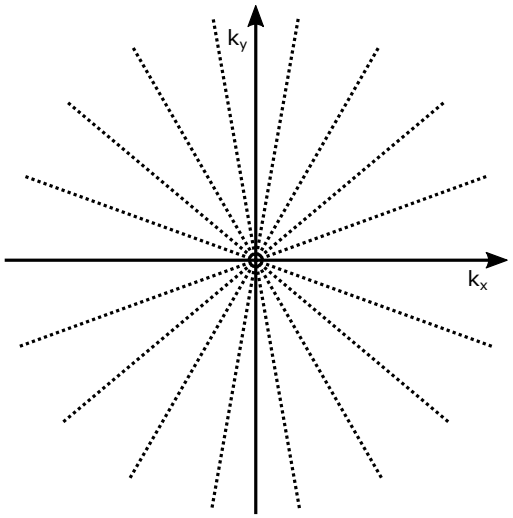

Figure 9: Radial two-dimensional k-space sampling trajectory with 9 radial profiles. Since each profile traverses the k-space center, the sampling density around the k-space center is much denser than on the circumference and the origin k_0 is sampled during each read-out.

2.2.1 Non-Cartesian Reconstruction

For non-cartesian trajectories the gradient encoded signal equation from 2.9 becomes [89]

$$s(\vec{k_n}) = \int_{FOV} m(\vec{r}) e^{-i2\pi \vec{k}_n \vec{r}} d\vec{r}, \tag{2.12}$$

where $s(\vec{k}_n)$ indicates that the signal is sampled at the non-cartesian sampling points $\vec{k}_n$. To reconstruct an image from the k-space samples s, the weighted inverse discrete Fourier transform ($IDFT$) may be used [84, 82]:

$$\hat{m}(\vec{r}) = \sum_{n=0}^{N_s-1} w(\vec{k_n}) s(\vec{k_n}) e^{i2\pi \vec{k}_n \vec{r}}. \tag{2.13}$$

The weighting function w accounts for the nonuniform density of the k-space sampling trajectory, and $\hat{m}$ is the image with the inherent artifacts to be expected by the discrete

Fourier transform. If the sampling density approaches the Nyquist rate, then $\hat{m} \approx m$ at the locations $\vec{r}$.

2.2.2 Discrete Matrix Notation

This section introduces the compact matrix / vector notation using linear algebra that will be used throughout the rest of this work [107]. In discrete form the acquisition process can be modeled, analog to equation (2.13), using the discrete Fourier transform (DFT)

$$\hat{s}(\vec{k}_n) = \sum_{j=0}^{N_m-1} m(\vec{r}_r) e^{-i2\pi \vec{k}_n \vec{r}_j}. \tag{2.14}$$

where $\vec{r}_j$ is the sequence of Cartesian image coordinates inside the field-of-view. This is a linear transformation and might thus be written in matrix form

$$s = DFT(m) = Am, \tag{2.15}$$

where $s \in \mathbb{C}^{N_s}$ is the complex signal, $m \in \mathbb{C}^{N_m}$ the complex image vector, and $A \in \mathbb{C}^{N_s \times N_m}$ the Fourier matrix defined by equation (2.14). Note, that two- or three-dimensional images and k-spaces are represented by one-dimensional vectors. Similar, the weighted IDFT from equation (2.13) might be written in matrix form as

$$\hat{m} = IDFT(Ws) = BWs = A^H Ws, \tag{2.16}$$

where A^H denotes the complex conjugate transposed of A, and W the diagonal sampling density compensation matrix with $W_{n,n} = 1/w(k_n)$ [106]. The relation $B = A^H$ follows directly from the diagonal symmetry of the Fourier matrix and the relation $\overline{e^{ix}} = e^{-ix}$. The matrix A is called the *system matrix*. It is $\hat{m} \approx m$ in case a W is found such that $A^H W \approx A^\dagger$, where $A^\dagger$ is the pseudoinverse of A [7].

2.2.3 Gridding Reconstruction

The complete evaluation of the inverse discrete Fourier (IDFT) transform is computational not practical. Even the explicit representation of A in computer memory is usually not feasible due to the large dimensions of A.

Therefore, practically a convolution interpolation (gridding) method is used [112], that interpolates an arbitrary k-space sampling pattern onto a Cartesian grid using a convolution kernel, which then allows the use of the Fast Fourier Transform (FFT). The gridding method is a fast and accurate approximation of the IDFT and is composed of the following steps [61]:

1. Convolution of k-space with gridding kernel
2. Resample result onto Cartesian grid
3. Apply FFT
4. Apodization Correction

The signal s from equation (2.12) is sampled using the sampling function T (k-space trajectory) which has the value 1 at the non-Cartesian sampling points and otherwise 0. The gridding method uses a convolution with the gridding kernel C and a subsequent discretization using a Dirac comb function III [8] with

$$\hat{m}[r] = FT^{-1}\{[\frac{s(k) \cdot T(k)}{w(k)} * C(k)]III(Gk)\}(r) \cdot a(r), \tag{2.17}$$

where $r \in [-N/2; N/2-1]$ are the discrete pixel locations, $*$ is the convolution operator, FT^{-1} the inverse Fourier transform, G the number of k-space pixels, $a(r) = 1/FT^{-1}\{C(k)\}(r)$ the apodization correction, and $k \in [-0.5; 0.5]$ the k-space locations. The density compensation function w compensates for the varying sampling density of the sampling function T.

Selection of the exact gridding kernel, kernel width, kernel sampling, and oversampling ratio has been subject to a long debate [61, 116, 112, 8, 120, 49, 48]. The optimal kernel

is the *sinc* function of infinite extent [91], but in practice usually the finite Kaiser-Bessel window is used [61] to minimize aliasing side lobes. The difference between gridding and the weighted IDF can be made arbitrary small by selecting the right oversampling ratio and gridding kernel [7], leading to a trade-off between accuracy and computation time. Practically, the improved gridding method proposed in [49] (NUFFT) is used often, that uses interpolation kernels which are numerically optimized to minimize the approximation error.

Note, that equation (2.17) formulates the IDFT transform. The matching DFT, that will be needed for iterative image reconstruction, is expressed similar without the density compensation w as

$$\hat{s}[k] = FT\{[\frac{m(r)}{a(r)} \cdot III(r)] * C(r)\}(k) \cdot T(k). \tag{2.18}$$

2.3 Parallel Imaging and SENSE

The knowledge of the spatial sensitivity profile of the receive coils implies spatial information about the origin of the detected MR signals, that is complementary to the spatial encoding by image gradients [72]. If more than one receive coil is used in parallel, this spatial information might be used during the reconstruction process to resolve the ambiguities (aliasing) due to k-space undersampling, resulting in an acceleration of the MR scan [107].

2.3.1 Coil Sensitivity Maps

Each coil of a coil array has a complex local coil sensitivity profile S_i. This sensitivity map is practically estimated using a reference scan m_{bc} using the homogeneous main body coil and a second scan m_i using the coil array. The complex coil sensitivity maps S_i include the coil sensitivities relative to the homogeneous body coil, as well as the coil

induced phase shifts relative to the body coil. S is calculated using a complex division of the form

$$S_i = m_i / m_{bc}. \tag{2.19}$$

Care has to be taken in image regions without or a very low signal, since the division with small numbers leads to noise amplification. Careful masking of areas not containing sufficient signal is required with successive interpolation of void regions [137] under the assumption that S contains only low image frequencies. Other work used an iteratively regularized solution of (2.19) [4].

Alternatively, in autocalibrating parallel MRI methods, the sensitivity maps are included as additional unknowns to equation (2.21) with a regularizing term that enforces smoothness of the sensitivity maps [133, 156]. This results in a non-linear problem, that is more difficult to solve, with the benefit of not needing a separate sensitivity profile scan.

2.3.2 Parallel Image Reconstruction

In the following, parallel imaging using *image-based* reconstruction methods is presented. A second class of reconstruction methods exists, that are *k-space-based* and will not be covered in this work. For more details regarding k-space-based methods see [54], and the relation between both methods [134, 6].

For parallel imaging the acquisition model (2.15) is modified, such that $s \in \mathbb{C}^{N_s N_c}$ holds the k-space samples of all N_c receiver coils and the linear model $A \in \mathbb{C}^{N_s N_c \times N_m}$ of the acquisition process combines the coil sensitivities S and the nonuniform Fourier transformations F into the block diagonal matrix $\hat{F}$

$$s = \begin{bmatrix} s_1 \\ \vdots \\ s_{N_c} \end{bmatrix}, S = \begin{bmatrix} S_1 \\ \vdots \\ S_{N_c} \end{bmatrix}, \hat{F} = \begin{pmatrix} F & \dots & 0 \\ \vdots & \ddots & \vdots \\ 0 & \dots & F \end{pmatrix} \text{ and } s = \hat{F}Sm = Am, \tag{2.20}$$

where $s_i \in \mathbb{C}^{N_s}$ is the data recorded by the i^{th} of N_c coils with N_s samples in k-space, S_i is an estimation of the coil sensitivity of the i^{th} coil, and $m \in \mathbb{C}^{N_m}$ the image vector.

In principle, parallel image reconstruction is a deconvolution problem, where the convolution with an aliasing kernel (or point-spread-function) $K = A^H A$ during the image reconstruction with A^H, is undone using a deconvolution matrix K^{-1} leading to the reconstruction equation [106]

$$m = K^{-1}A^H s = (A^H A)^{-1}A^H s. \tag{2.21}$$

The direct inversion of K is, due to the size of K, computational not feasible. Instead, an iterative approach is used solving the equation (2.21) for m in the following form

$$(A^H A)m = A^H s, \tag{2.22}$$

for example using a conjugate gradient solver since the coefficient matrix $A^H A$ is positive definite [106]. In theory, an unique solution m exists if $N_c N_s >= N_m$, that means the number of coils exceeds the undersampling factor R. In practice, the undersampling is limited by noise and the increasingly ill-conditioned posed problem for large reduction factors R. Various regularization methods have been proposed in the literature to solve the amplification of noise [66, 75, 74].

The main computational efforts during this process are the vector matrix multiplications with A and A^H, or more specifically the gridding and inverse gridding operations described by equations 2.17 and 2.18.

2.4 Compressed Sensing

The Shannon/Nyquist theorem [121] states that to fully capture all information of a signal, one must sample at twice the sampling rate than the signals bandwidth. Surprisingly, it was discovered in 2004 independently by Donoho [35] and Candés et al. [24], that the compressed sensing (CS) method is under certain conditions able to reconstruct an image (or signal) from a measurement that was sampled incomplete, below the Nyquist sampling rate. There are three preconditions for compressed sensing [21, 81, 2] in order to work:

1. P1 - Sparsity in ψ: The signal must be compressible in some base ψ.
2. P2 - Incoherence with ϕ: The measurement base ϕ and the sparsity base ψ must be incoherent.
3. P3 - Random sub-sampling X: The sub-sampling must be random and uniform

A signal or image x is compressible if a linear basis $\psi \in \mathbb{C}^{N_x \times N_X}$ exists that transforms the signal into a sparse representation x' with

$$x = \psi x'. \tag{2.23}$$

The signal x' is *k-sparse* if only k of the coefficients in x' are non-zero. The signal x is compressible if x' has few large and many small coefficients [22].

In a compressed sensing framework the measurement process takes fewer measurements at a sampling rate below the Nyquist theorem. The measurement process uses a measurement matrix $A \in \mathbb{R}^{N_b \times N_x}$ and a random sub-sampling matrix X to take the samples b

$$b = Ax = X\phi x = X\phi\psi x'. \tag{2.24}$$

If ϕ and ψ are mutually incoherent, a compressed sensing framework is able to fully

recover x from the sub-sampled measurement b using a non-linear reconstruction algorithm [21]. The art of compressed sensing is to find a good pair of a measurement matrix ϕ (that needs to be a model of the sensing hardware) and a fitting sparse representation matrix ψ with low coherence. It was shown by [37] that the mutual incoherence property (MIP) is a practical condition to measure the coherence

$$\mu = \sqrt{n} \cdot max_{i \neq j} |\phi_i^T \psi_j|. \tag{2.25}$$

The value of μ is inverse proportional to how many samples are minimally needed to recover a k-sparse signal - a lower μ indicates a lower k. Other related conditions for suitable matrices exists, e.g. the restricted isometry property (RIP) [25].

2.5 Sparse MRI

It is well known that most images, including medical and MRI images, are compressible. Many image compression methods (e.g. JPEG 2000 [128]) are based on a transformation into a sparse representation of the image and are storing only the most significant coefficients. Thus, the first precondition for compressed sensing is given in MRI.

Unfortunately, the second and the third preconditions are not directly fulfilled in MRI. The Fourier sampling matrix used in MRI exhibits a maximal high coherence with the common sparsity transformations for medical images (e.g. finite difference or wavelet transform) [68, 2]. For example, the low scale wavelets obviously correlate with the low Fourier frequencies. Fortunately, it was shown first empirically [81, 23] and recently more formally [68, 2] that compressed sensing in this setting works if variable-density sampling instead of uniform random sampling is used. That means, low k-space frequencies are to be sampled denser than the high k-space frequencies.

Choosing the incoherent sub-sampling matrix X in MRI means choosing a specific sub sampled k-space trajectory. Incoherent sampling trajectories suited for compressed sens-

ing were first described by Lustig et al. [81]. Examples are Cartesian trajectories with Gaussian random phase encoding or non-Cartesian radial trajectories that were already demonstrated in the original work by Candès [23].

In case of MR imaging, the acquisition process is modeled by the discrete linear imaging equation $s = Am = X\phi m$ where ϕ is the *sensing matrix* in terms of compressed sensing (Section 2.4) and A the system matrix as introduced in equation (2.15). The reconstruction problem is to find the image m for a given signal s. In case of undersampled data ($N_s < N_m$), the linear system of equation is under-determined and no unique solution, but a set of solutions exists. The reconstruction algorithm has to select the *right* solution, that is assumed to be sparsest solution of the set [35]. To select the sparsest solution under the sparsity transform ψ l0-minimization is used [36]

$$\underset{m:Am=s}{\operatorname{argmin}} \|\psi m\|_0. \tag{2.26}$$

Unfortunately, l0-minimization is a NP-hard problem in general [51]. Donoho [36] showed that l1-minimization is able to exactly recover k-sparse solutions with a high probability using

$$\underset{m:Am=s}{\operatorname{argmin}} \|\psi m\|_1. \tag{2.27}$$

The l1-minimization favors sparse solutions, in contrast to l2-minimization, which penalizes large values and favors small values. This optimization problem is called *basis pursuit* [27]. The l1-minimization problem is not only convex but also insensitive to noise added during the measurement process $s = Am + \epsilon$. Considering noise ϵ, the equation (2.27) becomes

$$\underset{m}{\operatorname{argmin}} \ \|\psi m\|_1 \ \text{ subject to } \|Am - s\|_2^2 < \epsilon. \tag{2.28}$$

This system might be solved using a non-linear conjugate gradient solver [88] in combination with the unconstrained La-Grange formulation of equation (2.28) suggested by

[81]:

$$\underset{m}{\operatorname{argmin}}\{\|Am - s\|_2^2 + \lambda\|\psi m\|_1\}. \tag{2.29}$$

The variable λ should be chosen such that $\|Am - s\|_2^2 \approx \epsilon$ [79]. In practice, the following objective function is minimized:

$$f(m) = \|Am - s\|_2^2 + \lambda\|\psi m\|_1. \tag{2.30}$$

The non-differentiable *absolute* function that is part of the l1-Norm is modified to become differentiable using the approximation $abs(x) \approx \sqrt{x^2 + \epsilon}$, which is also known as *corner rounding* [81]. The gradient of equation (2.30) is similar to equation (2.22)

$$\frac{\delta}{\delta m} f(m) = 2A^H Am - 2A^H s + \lambda\psi^H \frac{\psi m}{\sqrt{(\psi m)^H \odot (\psi m) + \epsilon}}, \tag{2.31}$$

where the square root, division, and vector-vector multiplication $\odot$ are element-wise operations.

Equation (2.29) can also be interpreted as a l1-regularized reconstruction, where λ balances the data fidelity of m to the signal s and the sparsity of m under ψ, to suppress aliasing and noise amplification. The nonlinear conjugated gradient method provides an easy solution to solve equation (2.29) but even with corner rounding the Hessian can have a very high curvature leading to a slow convergence [110, 108]. More advanced gradient descent algorithms such as MFISTA [10, 9] and split-Bregman-type algorithms [52, 109] handle non-smooth regularizers exactly without corner rounding and a higher convergence rate.

2.6 Time-Resolved MRI

Time-resolved MRI, or dynamic MRI, adds a temporal dimension by capturing an object in a changing state frame by frame. In a frame-by-frame acquisition process the maximal frame rate is limited by the acquisition time needed for a single frame, which is in turn limited by physical constraints (gradient strength and slew rate) and physiological constraints (nerve stimulation) [132].

The spatial resolution specifies to what minimal distance two lines can be resolved in an image and the unit for spatial resolution is usually *line pairs per millimeter* [38]. Accordingly, temporal resolution specifies to what frequency a blinking pixel may be resolved and the unit is cycles per second or Hertz. Just as an insufficient spatial resolution (in relation to the object) leads to *spatial blurring*, an insufficient temporal resolution (in relation to the moving object) leads to *temporal blurring*.

Important applications for time-resolved MRI are cardiovascular magnetic resonance (CMR) [158], functional MRI of the brain [77], time resolved angiography [53], joint kinetics (e.g. TMJ [20], knee [62] or wrist [17]), and imaging of the vocal tract [138].

Similar to equation (2.20), dynamic imaging can be formulated by combining the measurements for each frame into a single vector s, and by combining the Cartesian or nonuniform Fourier transforms for each frame F_n of N_f frames into the block-diagonal matrix $\hat{F}$

$$s = \begin{bmatrix} s_1 \\ \vdots \\ s_{N_f} \end{bmatrix}, \hat{F} = \begin{pmatrix} F_1 & \dots & 0 \\ \vdots & \ddots & \vdots \\ 0 & \dots & F_{N_f} \end{pmatrix} \text{ and } s = \hat{F}m = Am, \tag{2.32}$$

where $s_i \in \mathbb{C}^{N_s}$ is the data recorded for the n^{th} of N_f frames with N_s samples in k-space, and $m \in \mathbb{C}^{N_m N_s}$ is the dynamic image vector.

2.6.1 l2-Methods for Accelerating Time-Resolved MRI

To accelerate time-resolved MRI beyond the limits of the gradient system, k-space subsampling may be used. Two general sources of information are used to unfold the aliased images: sensitivity encoding as described in section 2.3 and spatiotemporal redundancy. Many methods were proposed that use one or both sources, the most relevant of them are listed in Table 1.

As described in Section 2.3, undersampling k-space leads to an underdetermined system of equations, with infinite valid solutions. All methods shown in Table 1 calculate the least square (l2-norm) solution and the spatiotemporal redundancy is either exploited by constraining or through regularization of the linear system. The reconstruction equation of those methods may be written in the generalized Tikhonov form [155, 131, 142]:

$$\hat{m} = \underset{m}{\operatorname{argmin}} \, |Am - s|_P^2 + |m - m_0|_Q^2, \tag{2.33}$$

with $|x|_Q^2$ being the weighted norm $x^T Q x$. The equation has the explicit solution

$$\hat{m} = (A^H P A + Q)^{-1}(A^H P s + Q m_0). \tag{2.34}$$

The methods mainly differ in the method of regularization (choice of P and Q) and the way the system is constrained to make it over-determined. The *k-t* BLAST method uses a training dataset in *x-f* space with low spatial but high temporal resolution to construct the temporal regularization matrix P. Using the Fourier transformed *k-t* space called *x-f* space leads to a compact representation that exploits quasi-periodic signal changes. The *k-t* PCA method is a generalization of *k-t* BLAST by constraining the system to the principal components of the training dataset, making it over-determined. The NoQuist method constrains the system to the dynamic parts of the image making it over-determined. The UNFOLD method is able to resolve non-overlapping aliasing using temporal low-pass filtering (choice of Q). All methods use Cartesian trajectories

and vary k-space sampling pattern in the phase encoding direction over time in order to decorrelate aliasing in the temporal dimension.

Table 1: Overview of linear methods that solve aliasing due to undersampling using spatiotemporal redundancies. For each method (left column) an according variant that works with parallel imaging exists (right column). The methods mainly differ by additional constraints that is applied to the objective function (second column) and by the regularization method (third column). Abbreviations: unaliasing by Fourier-encoding the overlaps in the temporal dimension (UNFOLD), sensitivity encoding (SENSE), SENSE with temporal filtering (TSENSE), field-of-view (FOV), reduced FOV method (NoQuist), parallel imaging and NoQuist in tandem (PINOT), k-t Broad-use Linear Acquisition Speed-up Technique (BLAST), principal component analysis (PCA).

Method	**Constraint**	**Regularization**	**Parallel Version**
UNFOLD [83]	Limit aliasing	Temporal low-pass	TSENSE [64]
NoQuist [19]	Dynamic parts of image	-	PINOT [58]
k-t BLAST [132]	Transform to x-f space	Training data	k-t SENSE [132]
k-t PCA [102]	Principal components in x-f space	Training data	k-t PCA/SENSE [102]

2.6.2 Compressed Sensing Time-Resolved MRI

The methods mentioned in the previous section all use the least square solutions of the system model. Compressed Sensing may also be used for dynamic imaging, exploiting sparsity in the temporal dimension similar to the methods in section 2.6.1, but using l1-norm regularization, enabling a higher undersampling factor.

Different sparsity transforms were suggested for the temporal dimension. Lustig et al.

[78] suggested using the wavelet transform for the spatial dimension and the Fourier transform for the temporal dimension. Gamper et al. used the Fourier transform for the temporal dimension [50]. Adluru et al. [3] suggested using the total variation (TV) transform in the spatial as well as in the temporal dimension. Feng et al. suggested using the temporal TV transform with an additional temporal Fourier transform [47].

The formulation of the reconstruction equation is the same as for non-dynamic compressed sensing in equation (2.29) in combination with the definitions for dynamic imaging from equation (2.32).

2.6.3 Golden Angle Radial MRI

Radial k-space trajectories are less sensitive to artifacts introduced by motion and therefore are often used for imaging of dynamic physiological processes [111]. Additionally, compared to Cartesian trajectories, radial trajectories are known to be robust to a certain level of azimuthal undersampling, which is used in time-resolved imaging to increase the temporal resolution. Sliding window reconstruction [111] is used to further increase the image update rate. Using the conventional radial sampling scheme, the width of the reconstruction window is fixed and must be selected before the acquisition is started. In most cases however, the optimal acquisition window size is not known a priori. Changing the acquisition window size requires rescanning of the subject with an adapted radial trajectory.

The golden angle $\psi_{gold} = \pi/\tau = 111.24...^{\circ}$ divides the semicircle by the golden ratio $\tau = (1 + \sqrt{5})/2$. The *golden angle trajectory* is the radial k-space trajectory where successive radial profiles are placed using a successive angle increment of ψ_{gold}. Note, that in this work a full revolution is defined by π instead of 2π due to the symmetry of the center-through trajectory that is used for most radial MRI sequences. The uniform angle increment is defined by $\psi_{uni} = \pi/P$ and provides the most uniform radial sampling trajectory for a given number of radial profiles P. If P cannot be predetermined prior to the acquisition, it was shown that the golden angle trajectory guarantees a near-optimal

uniformity of the radial distribution for an arbitrary number of successive profiles [144]. The uniformity reaches a local maxima if P is an element of the Fibonacci series (Figure 10).

This means, that the number of profiles in the reconstruction window, and thus the degree of undersampling, can be adjusted retrospectively to adapt to different levels of motion. During the last years, the golden angle ordering scheme has found widespread use in various applications from real-time imaging, over self-gated acquisition, to single scan T1- and T2-mapping [60, 76, 101, 117, 41, 125].

Another advantage of the golden angle is, that the separation in training scan and main scan that is necessary for some reconstruction methods becomes obsolete in golden angle radial MRI, since the same scan may be reconstructed in any combination of spatial and temporal resolution. A generalization of the golden angle will be presented in the first part of this work in Chapter 3.

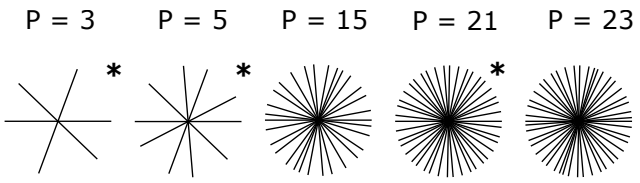

Figure 10: Golden angle k-space trajectory for various number of profiles P. Successive profiles are spaced by the golden angle increment $\psi_{gold} = \pi/r = 111.24...°$, where τ is the golden ratio $(1+\sqrt{5})/2$. Profile distributions where P is an element of the Fibonacci sequence $F_1 = 1; F_2 = 1; F_N = F_{N-1} + F_{N-2}$ exhibit a particular uniform distribution and are marked using the $*$ sign.

2.6.4 Golden Angle Radial Sparse Parallel MRI

In particular, radial trajectories with a golden angle ordering scheme have been used in combination with time-resolved parallel imaging and compressed sensing [33, 136, 34],

due to the intrinsic properties of this trajectory. First, the variable density sampling in k-space that oversamples the k-space center, second, the flexibility in the degree of retrospective undersampling, and last, the incoherent aliasing artifacts that are essential for compressed sensing [80, 26].

Feng et al. combined radial golden angle trajectories with parallel imaging and compressed sensing using temporal TV regularization into the iGRASP method [46]. This method will be extended in Chapter 4 of this work and is described in more detail in the following.

To combine parallel imaging and time-resolved imaging, the signal for all coils and all frames are combined into a signal vector s. The system equation according to equation (2.32) and equation (2.20) is

$$\hat{s}_n = \begin{bmatrix} s_{n,1} \\ \vdots \\ s_{n,N_c} \end{bmatrix}, \hat{s} = \begin{bmatrix} \hat{s}_1 \\ \vdots \\ \hat{s}_{N_f} \end{bmatrix}, \hat{S}_n = \begin{bmatrix} S_1 \\ \vdots \\ S_{N_c} \end{bmatrix}, S = \begin{bmatrix} \hat{S}_1 \\ \vdots \\ \hat{S}_{N_f} \end{bmatrix}, \tag{2.35}$$

$$\hat{F_n} = \begin{pmatrix} F_n & \dots & 0 \\ \vdots & \ddots & \vdots \\ 0 & \dots & F_n \end{pmatrix}, \hat{F} = \begin{pmatrix} \hat{F_1} & \dots & 0 \\ \vdots & \ddots & \vdots \\ 0 & \dots & \hat{F_{N_f}} \end{pmatrix} \text{ and } \hat{s} = \hat{F}Sm = Am, \tag{2.36}$$

where $b_{n,c}$ is the signal from the n^{th} frame and c^{th} coil, N_c the number of coils, N_f the number of frames, and F_n contains the nonuniform Fourier transform with the golden angle trajectory for the n^{th} time frame. Equation (2.36) becomes the fidelity term according to the compressed sensing framework of equation (2.30)

$$\underset{m}{\operatorname{argmin}}\{\|Am - s\|_2^2 + \lambda\|\nabla_t m\|_1\}, \tag{2.37}$$

with ∇_t being the temporal gradient operator. ∇_t in combination with the l1-norm is the *total variation* (TV) [21].

The temporal TV constraint expects the function of a single pixel over time to be approximately piece-wise constant. This model seems reasonable, if a piece-wise constant object changes mostly gradually over time (see Figure 11). In contrast, the Fourier transform, which may also be used for the sparsifying transform in the temporal dimension, models a cyclic and continuous pixel function over time.

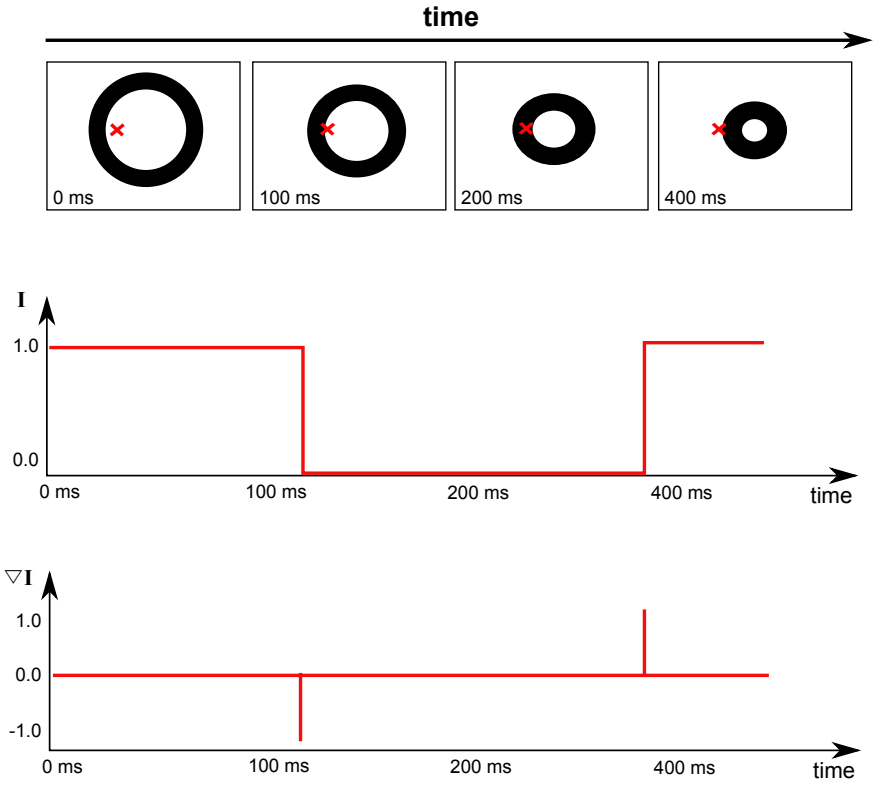

Figure 11: The intensity function (middle row) of a single pixel (red cross) from a cine image of a piece-wise constant object (top row) is also piece-wise constant in time if the object moves continuously. The finite difference ∇I (bottom row) of the intensity function I is therefore a sparse function and the finite difference often a suitable sparsifying transform for the reconstruction of cine images, e.g. of the contracting heart.

2.6.5 Gating and Self-Gating

Gating is an alternative time-resolved imaging method to resolve cyclic uniform motion that is to fast to be captured during a single motion cycle, even for rapid imaging sequences. The k-space for a single image of a specific motion phase is gradually filled during many cycles of a cyclic motion. The current motion phase is determined using a *gating signal*. For cardiac imaging the ECG signal is commonly used as gating signal [70] and for each cycle a reference (zero-phase) position is identified using the ECG's R wave. ECG-gating is the current gold standard for CMR and is used in clinical routine.

If no gating signal is available, self-gating methods may be used to retrospectively extract a gating signal from the k-space data itself. This method may be used for gating of the cardiac motion, but also for additional gating of the respiratory motion during cardiac scans [101].

For the image-based self-gating method suggested by Larson et al. [71] a preliminary image series m with low spatial and high temporal resolution is reconstructed using a sliding window reconstruction with window width w. The image series m is restricted to a region of interest (ROI) containing the myocardial wall. The 1D self-gating signal g is defined using the Pearson correlation ρ [40] of all images m_n to a selected template image m_t

$$g_n = \rho(m_t, m_n). \tag{2.38}$$

This technique performs well in comparison to other self-gating methods and may be combined with golden angle sampling [93, 130]. Usually, the 1D gating signal g has to be low-pass filtered, e.g. using a temporal median filter. Peaks of the signal are detected to identify a zero-phase (trigger point) for each motion cycle. The k-space profiles are sorted into time frames, based on the time interval to the neighboring peaks. Finally, the time frames are reconstructed frame-by-frame using gridding reconstruction. Cycles differing by more than a certain percentage in length from the mean cycle interval, for instance due to arrhythmia, are rejected.

2.7 Applications

Even though the core focus of this work is of a general nature, in a sense that it can be used for many applications, the results were demonstrated for two selected applications. A brief introduction to both applications is given in the following.

2.7.1 Cardiovascular Magnetic Resonance Imaging

Cardiovascular magnetic resonance imaging (CMR) is the assessment of the heart using magnetic resonance imaging techniques (Figure 12). CMR is used for the diagnosis of various cardiac diseases, e.g. valvular and congenital heart disease, or myocardial ischemia and infarction [103], using various MR techniques, e.g. ECG gating, myocardial perfusion imaging, or real-time imaging [113].

CMR has become the de facto standard in the assessment of cardiac function of both normal and abnormal ventricles and is e.g. superior to echocardiography [119].

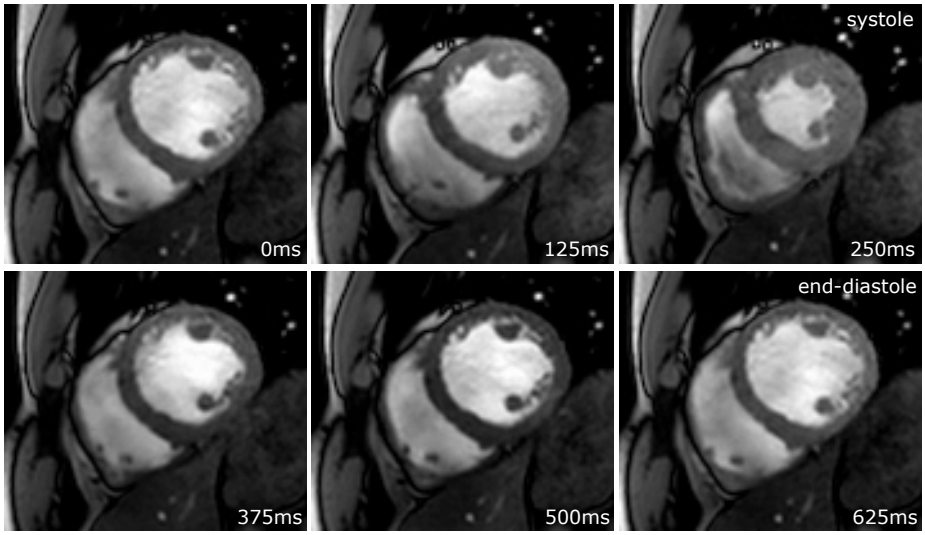

Figure 12: Cine magnetic resonance image of one cycle of a beating human heart in short-axis view, showing cross-sections of the left and right ventricle at consecutive points in time. The blood pool appears with a bright signal.

Prospective ECG triggered acquisition is the gold standard for cardiovascular magnetic

resonance imaging. Despite the use of rapid imaging sequences and accelerated parallel imaging for real-time imaging, the best spatial and temporal resolution is still achieved with ECG triggered, segmented breath-hold studies [70]. In absence of an ECG signal, retrospective self-gating (SG) might be used to reach a similar image quality [127, 71].

All gating methods have in common, that the gating signal is used to identify a zero-phase image (e.g. R wave) for each cycle. Under the assumption that all cardiac cycles are identical in motion, the partially sampled k-space of all cycles is combined into a fully sampled k-space.

In case of cardiac arrhythmia, the assumption of identical motion cycles is not valid. In practice, if the interval between two R waves deviates from the mean interval, the cycle is discarded. This leads to an increased acquisition time and sub-optimal image quality. Furthermore, the result misleadingly suggests a single motion cycle, concealing the arrhythmic cycles.

Balanced SSFP sequences have become the imaging method of choice for cardiac function at 1.5 Tesla [105]. Cardiac imaging benefits from the high SNR and intrinsic flow compensation of b-SSFP, which reduces artifacts and enhances the signal of inflowing blood [15].

2.7.2 MR Imaging of the Temporomandibular Joint

Temporomandibular joint dysfunction is a common problem that affects up to 28% of the population [124]. While only a few have organic diseases (e.g. arthritis, trauma, ankylosis, or neoplasia), the majority exhibits functional disorders, e.g. clicking sounds during mastication, facial pain, or limited joint motion [55]. Assessment of the motion of the TMJ therefore is of interest for a variety of pathologies, in particular the intra-articular derangement of the articular disc. One major question during the assessment of the TMJ is the dynamic relation of the discus articularis to the condyles and the fossa mandibularis [118].

While other modalities (axiography [104], sonography[69, 85], palpation) are also used for the examination of the TMJ, only MR imaging provides direct imaging of the disc-condyle complex, including the articular disc, and is considered the gold standard [141].

Early work on dynamic imaging of the TMJ started with the acquisition of a series of static images in different positions using differently sized bite blocks or incremental mouth opening devices [20, 31, 32]. These pseudo-dynamic images provided no accurate insight on the joint kinematics and are physiologically not equivalent to active movement of the mandibula [12, 39].

Therefore, various efforts have been made towards real-time imaging of the TMJ using fast imaging sequences like b-SSFP [1, 122, 5] and HASTE [140]. For these methods the patients were instructed to very slowly and continuously open and close the mouth, which requires some patient instruction and patient training. Due to the slow TMJ movement, these methods still do not reflect the true kinematics during a realistic joint motion.

Recently, real-time dynamic cine MRI using fast sequences in combination with radial trajectories were used for the imaging of the TMJ [60, 157] providing improved spatial and temporal resolution. However, imaging under realistic mastication speed is still limited by the limited spatiotemporal resolution of these methods. Table 2 shows an overview of previous work regarding time-resolved imaging of the TMJ.

During dynamic imaging of the articular disc the contrast to the surrounding tissue is achieved mainly due to the low T2 of the fibrocartilagenous tissue ($T2 \approx 26ms$ [115], $T2^* \approx 7ms$ [29]). For this reason, if FLASH sequences with T1 weighted contrast are used the articular disc is hardly visible. It was shown previously, that the b-SSFP sequence [90] enable the visibility of the articular disc with very short TE/TR due to its T1/T2 contrast [157] and is therefore the sequence best suited for dynamic imaging of the TMJ. However, the steady state of the b-SSFP sequence is very sensitive to off-resonances, especially if induced by abruptly changing eddy currents [14].

Table 2: Overview of time-resolved temporomandibular joint acquisition methods. The methods differ mainly in the used image sequence, its image contrast (second and third column), and the maximum achievable spatial and temporal resolution (fourth, sixth, and seventh row). Some methods are accelerated using an undersampled sampling scheme (8th column). Abbreviations: steady state free precession (SSFP), balanced SSFP (b-SSFP), half Fourier acquisition single shot turbo spin echo (HASTE), fast low angle shot (FLASH), T1 weighted turbo spin echo (T1W-TSE), k-space weighted image constrast (KWIC), fast field echo - echo planar imaging (FFE-EPI), proton density (PD), undersampling factor (R), Resolution (Res.).

Author	Sequence	Contrast	Slice Thickness [mm]	Cycle Time [s]	Spat. Res. [mm]	Temp. Res. [Hz]	R
Chen 2000 [28]	FFE-EPI	PD	5	7	1.1	2	1.25
Abolmaali 2004 [1]	b-SSFP	T2/T1	7	40	1.2	4	2
Beer 2004 [11]	T1W-TSE	T1	5	12	1.6	3	1
Shimazaki 2007 [122]	b-SSFP	T2/T1	10	72	1.2	1.7	1
Wang 2007 [140]	HASTE	PD	7	35	1.0	0.9	1
Azuma 2009 [5]	b-SSFP	T2/T1	3	21	1.8	0.7	1.3
Zhang 2011 [157]	b-SSFP	T2/T1	5	50	0.75	0.6	1
Hopfgartner 2013 [60]	FLASH	T1	3	15	0.59	1.5	KWIC[†]

[†] KWIC filtered, frequency dependent

Chapter 3

Summary of Methods

3.1 Tiny Golden Angles

In the first part of this work, a sequence of angles $\psi_N = \pi/(\tau + N - 1)$ is introduced where $\tau = (1+\sqrt{5})/2$ is the golden angle Ψ_1 and the complementary small golden angle Ψ_2. The new angles $\Psi_{N>2}$ are called *Tiny Golden Angles* and numerical simulations are performed to show that these angles (49.750..°, 32.039... °, 27.198... °, 23.628...°, ...) have the same optimal sampling efficiency $SE_N^\Psi = SNR_\Psi/SNR_{uni}$ as the golden angle for an arbitrary reconstruction window $P > 2N$, where SNR_{uni} is the optimal signal to noise ratio for an uniform radial sampling scheme [143]. The peak sampling efficiencies are located at members of the generalized Fibonacci sequence $G_1^N = 1; G_2^N = N; G_n^N = G_{n-1}^N + G_{n-2}^N$.

To proof, that the tiny golden angles are a suitable small surrogate for the golden angle in time-resolved radial MRI, images of a standard test phantom, time-resolved images of the moving heart in short-axis view, and cine images of the moving TMJ were acquired. Images were acquired at 3 T using a balanced SSFP sequence in combination with a radial trajectory using the golden angle, and the new tiny golden angles. The resulting images were compared to reference images acquired with uniform radial sampling by the normalized root mean square error, and visually analyzed for the appearance of eddy

current induced image artifacts.

3.2 Tiny Golden Angle Radial Sparse Parallel MRI (tyGRASP)

In the second part of this work, the tiny golden angle trajectories are analyzed for their incoherence properties in relation to sparse imaging by means of their time-resolved point-spread functions. Then, *tiny golden angle radial sparse parallel MRI* (tyGRASP) is introduced, a variant of the iGRASP method (see Section 2.6.4) in combination with the tiny golden angle ordering scheme. To proof, that the new method reconstructs images with a comparable image quality, a simulation experiment is performed using the numerical cardiac phantom MRXCAT [145]. Further, to show that the smaller angular increments of the new method enables the combination of the iGRASP method with b-SFFP sequences, both methods are evaluated with two applications.

For the feasibility study time-resolved short axis cardiac datasets of five healthy volunteers were acquired using tyGRASP with the tiny golden angles ψ_1 to ψ_7 and a b-SSFP sequence. To analyze image quality, the coefficient of variation of the left ventricle was measured for all datasets. Further, sagittal time-resolved images of the TMJ of five healthy volunteers were acquired using tyGRASP and the tiny golden angles ψ_1 to ψ_7 a b-SSFP and a FLASH sequence. The coefficient of variation of the TMJ area was measured for all datasets.

3.3 Nonuniform Self-Gating

A new nonuniform self-gating method for cyclic motion trajectories with a nonuniform pace is proposed. A sequence of radial k-space profiles in tiny golden angle order is acquired during multiple cycles of the nonuniform motion. Sliding window reconstruction is used to reconstruct an initial undersampled image sequence m. The sequence m is

restricted to a region of interest around the condyle and the pairwise Pearson correlation [40] of all images in m is used to calculate a 2D gating matrix, that exhibits a typical rhombus-structure for a cyclic but nonuniform motion (Figure 13). Instead of finding peaks in a 1D gating signal, as in image-base self-gating [71], the proposed method finds contours in the 2D gating matrix. Smooth and continuous curves are fitted onto the line structures of the matrix using active contour matching [63]. For each row one frame of the cine image is reconstructed using all k-space profiles in a neighborhood around the intersections with the active contours.

For the feasibility study short axis time-resolved data sets were acquired from three patients with known severe cardiac arrhythmia. The cine images were reconstructed using the proposed nuSG method and for comparison by an image-based self-gating method (SG)[71] and the iGRASP [46] real-time method. Further, time-resolved images of the TMJ from 8 healthy volunteers and 7 patients with suspected TMJ derangement were scanned. The patients were instructed to continuously open and close the mouth within 8 seconds. Images were reconstructed with nuSG, SG and iGRASP. For each cine image, the sharpness was calculated along a profile that was placed for cardiac images over the septal myocardial wall, and for TMJ images over the condyle edge. Significance of sharpness increase was assessed using the one-sided Wilcoxon signed rank test. A quantitative analysis of the left ventricular blood pool area was done using standard software (Segment, Medviso, Lund, Sweden (24)).

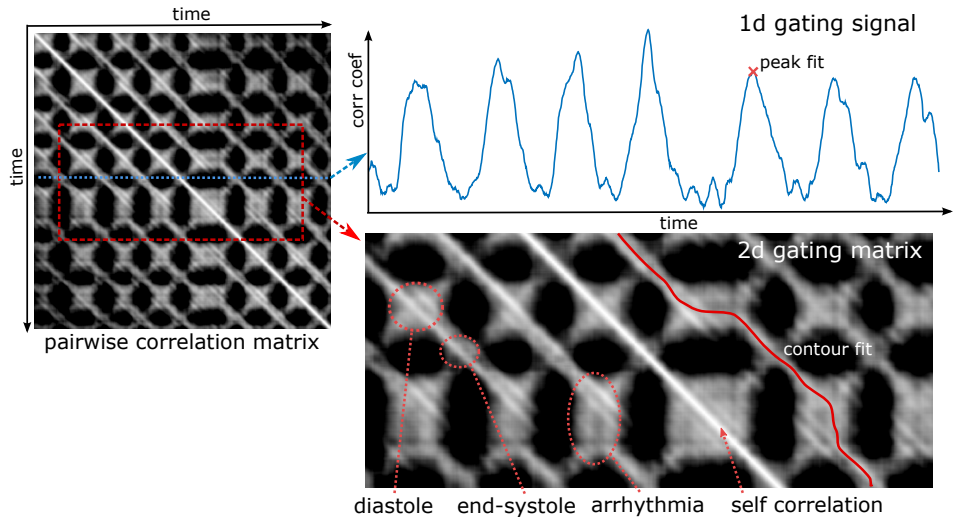

Figure 13: Structure of the pair-wise correlation matrix for an arrhythmic heart. Higher values indicate higher similarity of the template image (row) to the comparison image (column). The reference image is similar to images in the same position and same movement direction (lines parallel to the main diagonal) and in the same position and the opposite movement direction (lines orthogonal to the main diagonal). A row of the matrix equals the one-dimensional self-gating signal used in image-based self-gating (top). The peaks in the one-dimensional gating signal form curved lines in the two-dimensional gating matrix (bottom, red).

Chapter 4

A Small Surrogate for the Golden Angle in Time-Resolved Radial MRI Based on Generalized Fibonacci Sequences (reprinted article)

This article [153] was published as

Wundrak, S., Paul, J., Ulrici, J., Hell, E., and Rasche, V. A Small Surrogate for the Golden Angle in Time-Resolved Radial MRI Based on Generalized Fibonacci Sequences. *IEEE Transactions on Medical Imaging* 34.: 1262–1269, 2015

A Small Surrogate for the Golden Angle in Time-Resolved Radial MRI Based on Generalized Fibonacci Sequences

Stefan Wundrak*, Jan Paul, Johannes Ulrici, Erich Hell, and Volker Rasche

***Abstract*—In golden angle radial magnetic resonance imaging a constant azimuthal radial profile spacing of $111.246\ldots^\circ$ guarantees a nearly uniform azimuthal profile distribution in k-space for an arbitrary number of radial profiles. Even though this profile order is advantageous for various real-time imaging methods, in combination with balanced steady-state free precession (SSFP) sequences the large azimuthal angle increment may lead to strong image artifacts, due to the varying eddy currents introduced by the rapidly switching gradient scheme. Based on a generalized Fibonacci sequence, a new sequence of smaller irrational angles is introduced ($49.750\ldots^\circ, 32.039\ldots^\circ, 27.198\ldots^\circ, 23.628\ldots^\circ, \ldots$). The subsequent profile orders guarantee the same sampling efficiency as the golden angle if at least a minimum number of radial profiles is used for reconstruction. The suggested angular increments are applied for dynamic imaging of the heart and the temporomandibular joint. It is shown that for balanced SSFP sequences, trajectories using the smaller golden angle surrogates strongly reduce the image artifacts, while the free retrospective choice of the reconstruction window width is maintained.**

***Index Terms*—Golden angle, radial trajectory, real-time imaging.**

I. Introduction

IN RADIAL magnetic resonance imaging (MRI) the k-space is sampled with a set of radial profiles that each pass through the k-space center [1]. Radial k-space trajectories are less sensitive to artifacts introduced by motion and therefore are often used for imaging of dynamic physiological processes [2]. Additionally, compared to Cartesian trajectories, radial trajectories are known to be robust to a certain level of azimuthal undersampling, which is used in time-resolved imaging to increase the temporal resolution. Sliding window reconstruction [2] is used to further increase the image update rate. Using the normal radial sampling scheme, the width of the reconstruction window is fixed and must be selected before the acquisition is started. In most cases however, the optimal acquisition window size is not known *a priori*. Changing the acquisition window size requires rescanning of the subject with a differently spaced radial trajectory.

It was shown in [3] that if radial profiles are placed using the golden angle profile order which uses a consecutive profile spacing of $111.24\ldots^\circ$ (golden angle), a nearly uniform profile distribution is guaranteed for an arbitrary number of successively acquired profiles. This means that the number of profiles in the reconstruction window and thus the degree of undersampling can be adjusted retrospectively to adapt to different levels of motion. During the last years the golden angle ordering scheme has found widespread use in various applications from real-time imaging, over self-gated acquisition, to single scan T1- and T2-mapping [4]–[10]. In particular, radial trajectories with a golden angle ordering scheme have been used in combination with parallel imaging and compressed sensing [11]–[13] due to the intrinsic properties of this trajectory. First, the variable density sampling in k-space that oversamples the k-space center, second the flexibility in the degree of retrospective undersampling, and last the incoherent aliasing artifacts that are essential for compressed sensing [14], [15].

In this work we introduce a new sequence of angles that is based on a generalized Fibonacci sequences. We show that the smaller *tiny golden angles* exhibit properties that are very similar to the original golden angle.

We show the advantages of the newly introduced angles for dynamic MR imaging in combination with fully balanced steady-state free precession sequences (b-SSFP) [16]. The large angular increment of the golden angle profile order leads to a permanently and abruptly changing gradient scheme, which leads to rapidly changing eddy currents in the conducting part of the magnet, and in-turn to rapidly varying field inhomogeneities. The equilibrium of the b-SSFP sequence is especially sensitive for these varying eddy current effects and may exhibit strong signal fluctuations [17]. These image artifacts are avoided by the smaller angle increments of the new surrogate angles while preserving the inherent properties of the golden angle ordering scheme for dynamic imaging.

II. Theory

A. Golden Angle Trajectory

The golden angle $\psi_{\text{gold}} = \pi/\tau$ divides the semicircle by the golden ratio $\tau = (1+\sqrt{5})/2$. The *golden angle trajectory* is the radial k-space trajectory where successive radial profiles are

Manuscript received October 14, 2014; revised December 10, 2014; accepted December 10, 2014. Date of publication December 18, 2014; date of current version May 29, 2015. *Asterisk indicates corresponding author.*

*S. Wundrak is with the University Hospital Ulm, 89081 Ulm, Germany and Sirona Dental Systems, D-64625 Bensheim, Germany (e-mail: stefan.wundrak@sirona.com).

J. Paul and V. Rasche are with the University Hospital Ulm, 89081 Ulm, Germany (e-mail: jan.paul@uniklinik-ulm.de; volker.rasche@uniklinik-ulm.de).

J. Ulrici and E. Hell are with Sirona Dental Systems, D-64625 Bensheim, Germany (e-mail: johannes.ulrici@sirona.com; erich.hell@sirona.com).

Color versions of one or more of the figures in this paper are available online at http://ieeexplore.ieee.org.

Digital Object Identifier 10.1109/TMI.2014.2382572

placed using a successive angle increment of ψ_{gold}. Note, that in this work a full revolution is defined by π instead of 2π due to the symmetry of the center-through trajectory that is used for most radial MRI sequences. The uniform angle increment is defined by $\psi_{\text{uni}} = \pi/P$ and provides the most uniform radial sampling trajectory for a given number of radial profiles P. If P cannot be predetermined prior to the acquisition, it was shown that the golden angle trajectory guarantees a near-optimal radial distribution for an arbitrary number of profiles [3]. The golden angle increment successively divides one of the largest remaining azimuthal gaps by the golden ratio.

To compare the quality of different sampling trajectories the *sampling efficiency* is calculated. A nonuniform profile distribution has a nonuniform azimuthal sampling density, which affects the signal-to-noise ratio (SNR) of the reconstructed image. The SNR for a given trajectory can be derived directly from the sampling density of the k-space sampling schemes. The sampling efficiency SE_P^{ψ} for a given ψ and for P radial profiles equals the ratio of the SNR of the uniform sampling scheme SNR_{uni} and the SNR of the ψ sampling scheme SNR_{ψ} [18]. This leads to the following definition of the *sampling efficiency* proposed by Winkelmann *et al.* (see [3] for details)

$$SE_P^{\psi} = \frac{\text{SNR}_{\psi}}{\text{SNR}_{\text{uni}}} = \sqrt{\frac{\frac{\pi^2}{P}}{\sum_{i=0}^{P-1}(\Delta\Phi_i)^2}} \tag{1}$$

with $\Delta\Phi_i$ being the mean azimuthal distance of the ith profile to its two adjacent profiles. The sampling efficiency of the golden angle $SE_P^{\psi_{\text{gold}}}$ falls never below 0.9732 for all P and has its local maxima if P is a Fibonacci number [3].

B. Tiny Golden Angles

The aim of this work is to find smaller angles that exhibit similar properties as the golden angle. A geometric construction is used for a new sequence of angles (Fig. 1). If angle increments $0 < \psi < \pi$ are used the $(N+1)$th radial profile will have an angle larger than π if $N = \lfloor \pi/\psi \rfloor$. We define all angles ψ_N that divide the last azimuthal gap before reaching π by the golden ratio τ using the relation

$$\frac{\psi_N}{\pi - N\psi_N} = \tau. \tag{2}$$

Solving (2) for ψ_N using the known relation $1/\tau + 1 = \tau$ leads to the sequence of angles

$$\psi_N = \frac{\pi}{\tau + N - 1}. \tag{3}$$

The first two members for $N = 1$ and $N = 2$ of this sequence are the well-known golden angle and the complementary small golden angle

$$\begin{aligned} \psi_1 &= \frac{\pi}{\tau} \\ \psi_2 &= \frac{\pi}{(\tau+1)} = \pi - \psi_1. \end{aligned} \tag{4}$$

In this work we will call all ψ_N for $N > 2$ *tiny golden angles*. The first ten members of the sequence ψ_N are shown in Table I. Some of these angles are known to be found in the process of phyllotaxis of various plants [19], [20]. Fig. 2 shows the profile placement for a selection of angles and values for P. The sampling efficiency $SE_P^{\psi_N}$ has its local maxima if P is a member of the generalized Fibonacci sequence G^N [21], that is defined by

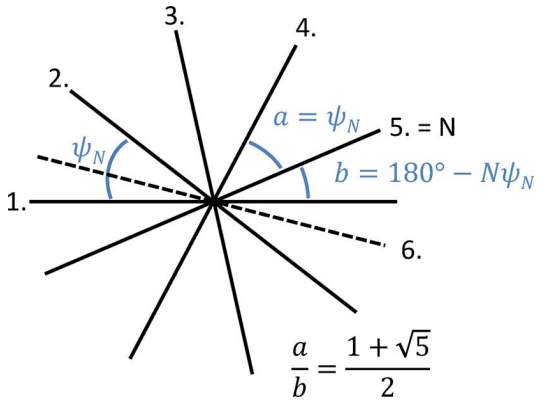

Fig. 1. Geometric construction of ψ_N for $N = 5$. Last gap before the profile angle gets lager than π, between the fourth and the first profile, is divided by the golden ratio. Sixth profile divides the next gap also by the golden ratio. Solving the relation $a/b = \tau$ leads to ψ_N.

TABLE I
FIRST 10 ELEMENTS OF THE SEQUENCE ψ_N

N	ψ_N	G_3^N	G_4^N	G_5^N	G_6^N	$SE_{P>2N}^{\psi_n}$
1	111.24611...°	2	3	5	8	[0.973, 0.996]
2	68.75388...°	3	5	8	13	[0.974, 0.996]
3	49.75077...°	4	7	11	18	[0.974, 0.997]
4	38.97762...°	5	9	14	23	[0.973, 0.997]
5	32.03967...°	6	11	17	28	[0.973, 0.998]
6	27.19840...°	7	13	20	33	[0.973, 0.998]
7	23.62814...°	8	15	23	38	[0.973, 0.998]
8	20.88643...°	9	17	26	44	[0.973, 0.999]
9	18.71484...°	10	19	29	48	[0.973, 0.999]
10	16.95229...°	11	21	32	53	[0.973, 0.999]

$$G_1^N = 1;\ \ G_2^N = N;\ \ G_n^N = G_{n-1}^N + G_{n-2}^N \tag{5}$$

where G^1 is the well-known Fibonacci sequence. In fact, the sequence ψ_N could be directly derived from the generalized Fibonacci sequences itself (see Appendix A).

If radial profiles are added successively spaced by the constant increment ψ_N, each additional profile after $P > N$ divides one of the currently largest azimuthal gaps by the golden ratio (see Appendix B for proof). The sampling efficiency is comparable to the sampling efficiency of the golden angle trajectory (Fig. 3) for $P > 2N$ and the bounds defined by the local minima and maxima of $SE_{P>2N}^{\psi_N}$ converge to the bounds of $SE_{P>2}^{\psi_{\text{gold}}}$. The guaranteed bounds for ψ_N were calculated numerically for the window $P \in [2N+1, 10^4]$ using (1) and are shown in Table I.

C. Beyond the Tiny Golden Angles

A radial trajectory using any constant irrational angle increment will exhibit at most three different gap sizes, and will successively divide one of the largest gaps (proven by Knuth [22]). Furthermore, any irrational number x can be expressed by a regular continued fraction [23] of the form

$$x = a_0 + \cfrac{1}{a_1 + \cfrac{1}{a_2 + \cfrac{1}{a_3 + \cdots}}} = [a_0, a_1, a_2, a_3, \ldots]. \tag{6}$$

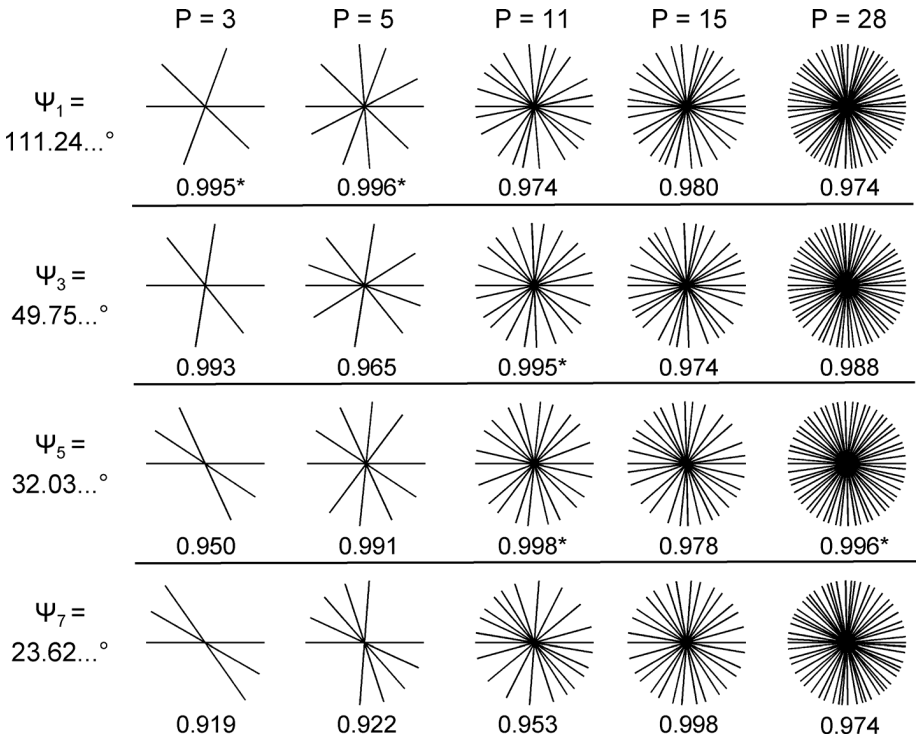

Fig. 2. Placements of the radial profiles using the tiny golden angle increments ψ_N for N $= 1, 3, 5,$ and 7. Sampling efficiency $SE_P^{\psi_N}$ is printed under each profile distribution. Profile distributions where P is an element of the generalized Fibonacci sequence G^N, are marked using the * sign.

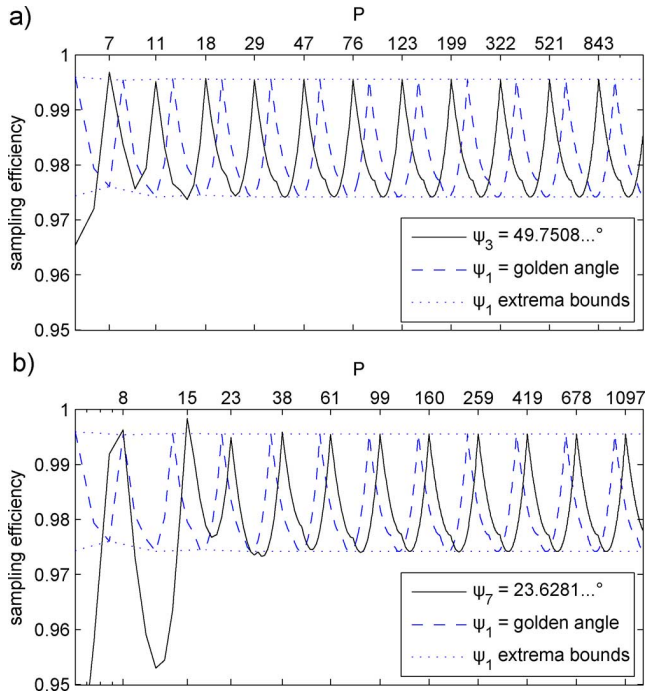

Fig. 3. Sampling efficiency for (a) ψ_3 and (b) ψ_7 compared to the golden angle increment $\psi_1 = 111.246\ldots°$. Logarithmic scale is used on the x-axis. Maximum sampling efficiencies are reached if P is a member of the generalized Fibonacci sequence $G_1^N = 1; G_2^N = N; G_n^N = G_{n-1}^N + G_{n-2}^N$. For $P > 2N$ (7, 15) the sampling efficiency stays practically within the extremal bounds of the golden angle. Plots for ψ_3 to ψ_{10} are provided as supplementary material.

Using this notation and the well-known definition of $\tau = [1, \overline{1}]$ [24], the angles ψ_N as defined in (3) can be expressed by the regular continued fraction

$$\psi_N = \frac{\pi}{N - 1 + [1, \overline{1}]} = \pi[0, N, \overline{1}]. \tag{7}$$

Fig. 4 shows a plot of the minimal sampling efficiency for all angle increments between 0 and π using the function

$$f(\alpha) = \min_{P \in [21;400]} SE_P^{\alpha}. \tag{8}$$

The arbitrary choice of $P \geq 21$ ensures on the one hand that for the first 10 angles $N > 2P$ (see Section II-B) which covers angles $> 17°$, and on the other hand $P = 21$ is still a small enough reconstruction window for most real-time applications. The plot shows clearly that all ψ_N are located at high local maxima of f. Note that the maxima for $\psi_{N>10}$ are not visible in this plot due to the choice of $P \geq 21$.

However, additional local maxima are visible in between the locations of ψ_N. Analog to the original geometric construction of ψ_N (Fig. 1), we define the set of angles $\psi_{N,M}$ by dividing the last segment using the ratio $M - 1 + \tau$ instead of τ. Analog to (2) the relation $a/b = M - 1 + \tau$ leads to the definition of

$$\psi_{N,M} = \frac{\pi}{N + \frac{1}{M-1+\tau}} = \pi[0, N, M, \overline{1}]. \tag{9}$$

The angles $\psi_{2,2}$, $\psi_{2,3}$, $\psi_{2,4}$, $\psi_{3,2}$, $\psi_{3,3}$, and $\psi_{3,4}$ specify the prominent maxima below 90° shown in Fig. 4 (dotted green lines) that were not covered by any ψ_N. Analog to (5) the generalized Fibonacci sequence that defines the peak sampling efficiencies for $\psi_{N,M}$ is

$$\begin{aligned} G_1^{N,M} &= 1 + (M-1)N; \;\; G_2^{N,M} = N \\ G_n^{N,M} &= G_{n-1}^{N,M} + G_{n-2}^{N,M}. \end{aligned} \tag{10}$$

Theoretically, one could extend this scheme to use more coefficients of the continued fraction to explore more angles in the set $\psi_{N,M_1,\ldots,M_k} = \pi[0, N, M_1, \ldots, M_k, \overline{1}]$. One would find more sub-optimal angles, but with increasing M and k the local

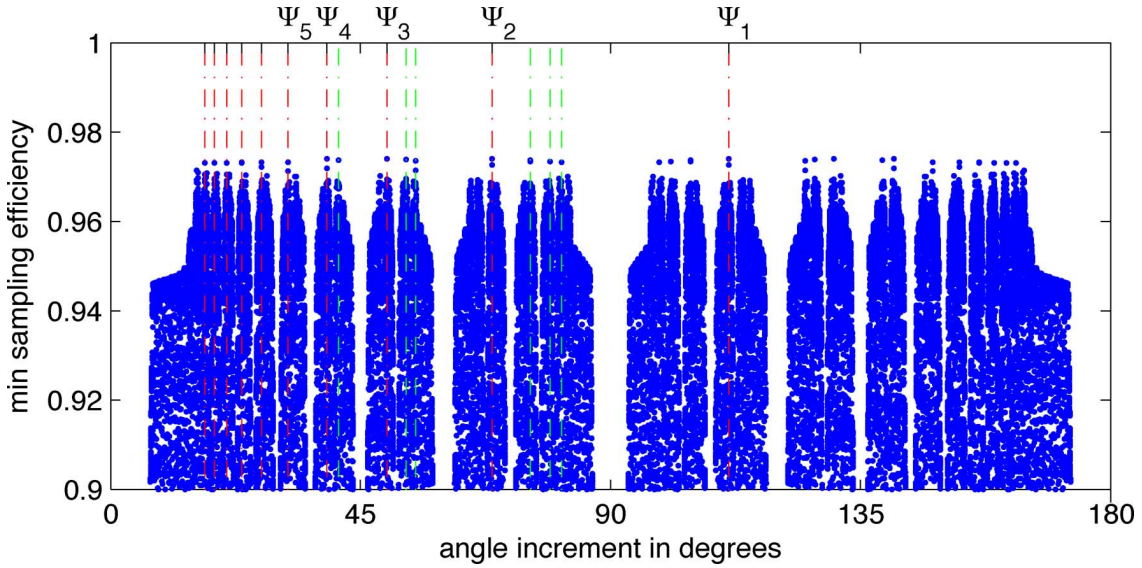

Fig. 4. Minimum sampling efficiency in the window $P \in [21; 400]$ for all angle increments in $[0; 180°]$ calculated with a resolution of $0.002°$. Dotted red lines are local maxima located at the sequence of the tiny golden angles ψ_N. Each tiny golden angle has side-maxima located at the set $\psi_{N,M}$ (dotted green lines, shown for ψ_4, ψ_3, and ψ_2 only). Plot is symmetrical to $90°$ due to the radial center-through trajectory. The maxima of ψ_N for $N > 10$ are not visible (left of $15°$) due to the arbitrary choice of $P > 20$.

maxima get less distant from each other and exhibit worse uniformity. Practically, two coefficients and $M < 5$ are sufficient to reach all relevant local maxima (compare Fig. 4).

III. Material and Methods

A. Experiments

1) Point Spread Function Analysis: Time-resolved sequences of two-dimensional point spread functions (PSF) were created using radial sampling patterns with a constant azimuthal increment of ψ_1 and ψ_5. For both the PSF were created using the optimal resolution for ψ_1 ($G_{10}^1 = 55$) and for ψ_5 ($G_8^5 = 73$). For all four sampling schemes the temporal maximum intensity projection (t-MIP) [15] was created by taking the maximum value of each pixel of the PSF sequence over time. The point spread functions were generated by an inverse gridding reconstruction followed by a successive gridding reconstruction of an image of 256×256 pixel that contained one single pixel with a signal intensity greater than zero.

2) Phantom Imaging: A standard test phantom (Philips, Best, The Netherlands) was scanned using a radial trajectory with a constant azimuthal increment using the golden angle ψ_1, as well as the tiny golden angles ψ_2 to ψ_7. In addition, a reference trajectory with a small azimuthal sampling increment of $0.5°$ was used that leads to a perfect uniform trajectory if a multiple of $P = 360$ radial profiles are used for the image reconstruction window. The acquisition parameters for the balanced SSFP sequence were $\mathrm{TR/TE} = 4.6/2.3$ ms, flip angle $= 48°$, pixel bandwidth of 934.8 Hz, a spatial resolution of $0.75 \times 0.75 \times 8$ mm^3, and a 320×320 pixel acquisition matrix.

3) Real-Time Cardiac Imaging: Dynamic short axis real-time cardiac data sets were acquired from a healthy volunteer using a radial trajectory with a constant azimuthal increment using the golden angle ψ_1, and the angles ψ_3, ψ_5, ψ_7. A reference image was acquired using a constant sampling increment of $3°$ which leads to an uniform trajectory if a multiple of $P = 60$ radial profiles are used for the image reconstruction window. A 32 channel cardiac coil was used during breathhold. The acquisition parameters for the balanced SSFP sequence were $\mathrm{TR/TE} = 2.3/1.15$ ms, flip angle $= 43°$, pixel bandwidth of 2688 Hz, spatial resolution of $2.74 \times 2.74 \times 8$ mm^3, and a 124×124 pixel acquisition matrix.

4) Dynamic Temporomandibular Joint Imaging: Dynamic images of the temporomandibular joint (TMJ) were acquired under a slow and continuous opening and closing motion of the mandibular. The volunteer was instructed to open and close the mouth continuously and as uniformly as possible within 20 s. The fully balanced SSFP sequence was used due to its T1/T2 contrast at short echo times which is essential for the fast imaging of the discus articularis [25]. A radial k-space trajectory with a constant angular increment using the tiny golden angle ψ_7 was used. The scan was repeated using the balanced SSFP sequence as well as a FLASH sequence [26]. A 2×4 channel carotid coil (Chenguang Medical Technologies, Shanghai, China) was used. The acquisition parameters for the balanced SSFP sequence were: in-phase, $\mathrm{TE/TR} = 2.3/4.6$ ms, flip angle $= 45°$, pixel bandwidth of 949 Hz, and spatial resolution of $0.75 \times 0.75 \times 5$ mm^3 with an acquisition matrix of 256×256 pixel. The acquisition parameters for the FLASH sequence were the same, except that the flip angle was reduced to $15°$.

All datasets were acquired on a Philips 3T Achieva system (Philips Healthcare, Best, The Netherlands). Written informed consent was obtained in all cases prior to examination.

B. Reconstruction

For all experiments the images were reconstructed using gridding convolution interpolation with a Kaiser-Bessel-window

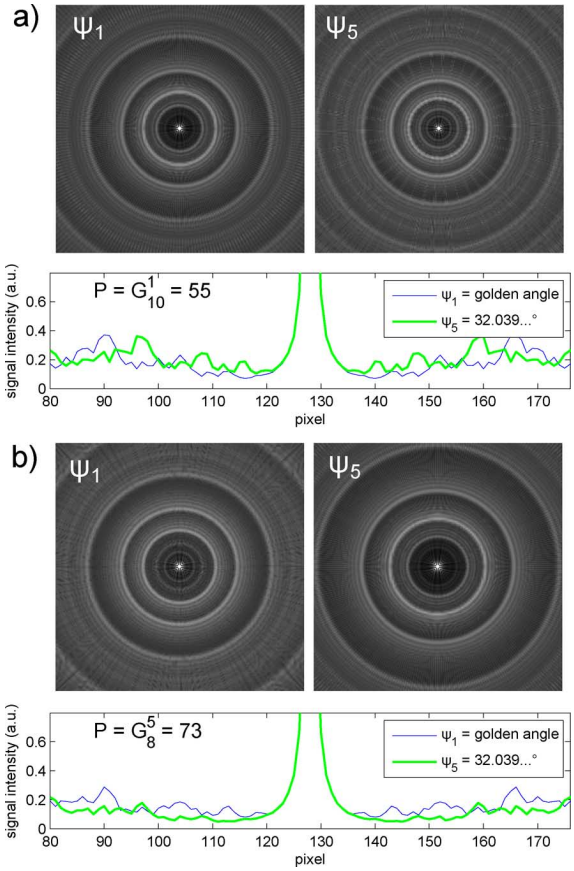

Fig. 5. Point spread function analysis using T-MIPs of ψ_1 and ψ_5 for a window width of (a) $P = 55$ radial profiles (optimal for ψ_1), and (b) $P = 73$ radial profiles (optimal for ψ_5). Plots display the signal intensity over 100 pixels across the horizontal central line of the T-MIPs.

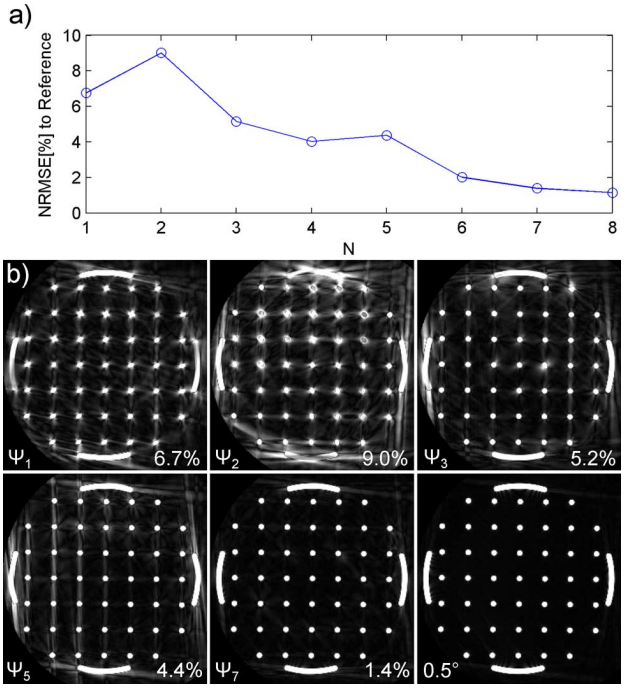

Fig. 6. NRMSE for images acquired with radial angle increments ψ_N and a b-SSFP sequence, in comparison to a reference image acquired with uniform sampling at 0.5° (a). Reconstructed images for a selection of radial angles ψ_N exhibit strong image artifacts for $N < 7$ (b). NRMSE is given in percent for each image. Signal intensity was scaled by a factor of two to accentuate the image artifacts.

width of five pixel [27]. The density compensation was adapted to compensate the variations of azimuthal gaps [3]. Prior to reconstruction, the k-space data was corrected for phase errors by identifying pairs of profiles that were measured in approximately opposite directions. For each pair a trajectory shift was estimated using linear regression of the profiles' phase deviation in image space as described in [28] and [29]. The cardiac image sequence was filtered using a total variation filter along the temporal dimension to remove the remaining incoherent streak artifacts [30], all other image sequences are unfiltered. All images were reconstructed using an in-house software package implemented with MATLAB (MathWorks, Natick, MA, USA).

IV. Results

A. Point Spread Function Analysis

Fig. 5 shows the result of the point spread function analysis. For 55 radial profiles ψ_1 shows lower aliasing lobes than ψ_5 [Fig. 5(a)]. This is explicable, since $P = 55 = G^1_{10}$ is a Fibonacci number which is optimal for the golden angle ψ_1 profile order, but not for the ψ_5 profile order. In case of $P = 73$ profiles, P is the generalized Fibonacci Number G^5_8, thus yielding lower aliasing lobes for the Ψ_5 acquisition order [Fig. 5(b)].

B. Phantom Imaging

The images taken from the test phantom using the tiny golden angles were compared to the reference image that were taken with a small angle increment of 0.5°. The normalized root mean square error (NRMSE) was used for comparison. Fig. 6(a) shows that with a decreasing azimuthal angle the error also tends to decrease. Despite the small local maxima at ψ_2 and ψ_5, for $N > 7$ the error falls below 1.4%. Fig. 6(b) shows a selection of the images that were used to create the plot in Fig. 6(a). The image artifacts are shown accentuated by scaling the image intensity by a factor of two. The image artifacts are clearly strongest with the large and the small golden angle ψ_1 and ψ_2 (NRMSE $> 6\%$), and are reduced for ψ_7 to a visually acceptable level in comparison to the reference image (NRMSE $= 1.4\%$).

C. Real-Time Cardiac Imaging

Fig. 7(a) shows short axis views of the heart in systolic state. The images were reconstructed from continuously acquired radial profiles using a retrospectively chosen reconstruction window width of $P = 60$ radial profiles. The image acquired with the golden angle azimuthal increment ψ_1 shows strong image artifacts, which decrease with decreasing angular increment. The image artifacts are reduced if the angle gets smaller (ψ_3, ψ_5). The image that was acquired with the smallest angle ψ_7 exhibits an artifact level visually comparable to the reference image. Since the resting phase of the heart in end-diastolic phase is significantly longer than the resting phase of the systole, the reconstruction window width could be increased

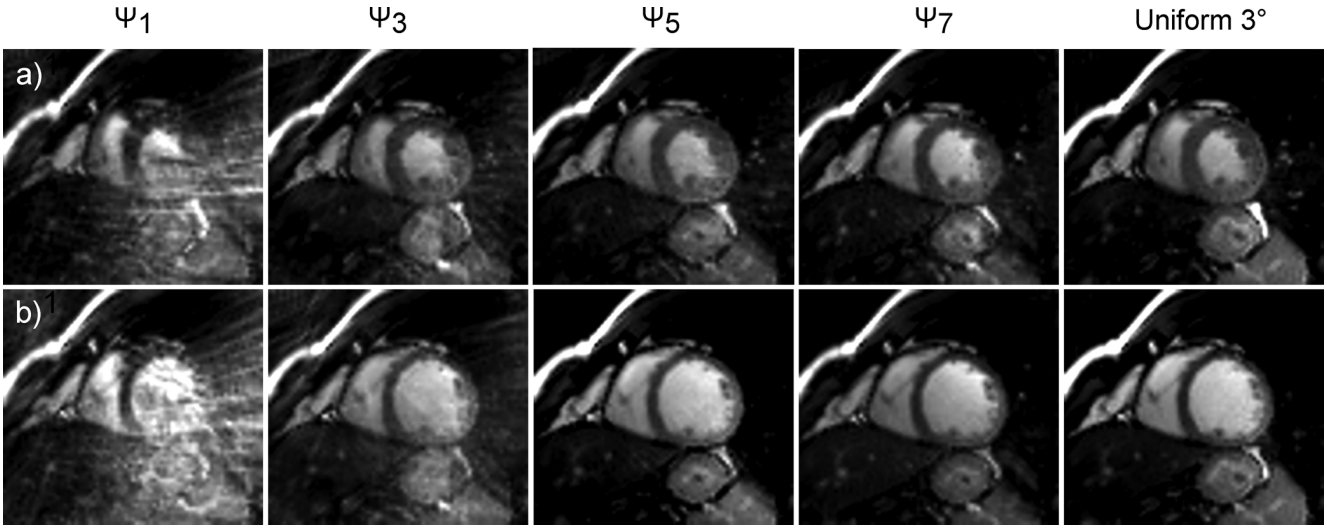

Fig. 7. Cardiac short-axis view scanned multiple times with different constant angle increments ψ_N and 3° using a b-SSFP sequence during breathhold. Systole was reconstructed with 60 radial profiles (a), the diastole with 120 profiles (b). Golden angle ψ_1 shows strong image artifacts due to the large angle increment and the resulting rapidly changing eddy currents.

to 120 radial profiles without introducing temporal blurring [Fig. 7(b)]. The image artifacts show similar behavior as for the systolic reconstructions.

D. Dynamic Temporomandibular Joint Imaging

The resulting images of the moving TMJ during its opening phase are shown in Fig. 8. The image that was reconstructed using the tiny golden angle ψ_7 has comparable image quality to the reference image that was acquired with the 3° uniform sampling scheme (middle row). The borders of the discus articularis are clearly visible (arrow) due to the T1/T2 contrast of the b-SSFP sequence. In contrast to the uniform sampling scheme, the tiny golden angles profile order allows the reconstructing using an arbitrary reconstruction window width without introducing additional artifacts due to a nonuniform sampling scheme (top row). Using the original golden angle profile order ψ_1 introduces strong image artifacts (bottom right). These perturbations are not visible if a FLASH sequence is used, but at the cost of reduced SNR and the reduced visibility of the discus articularis (bottom left, white arrows).

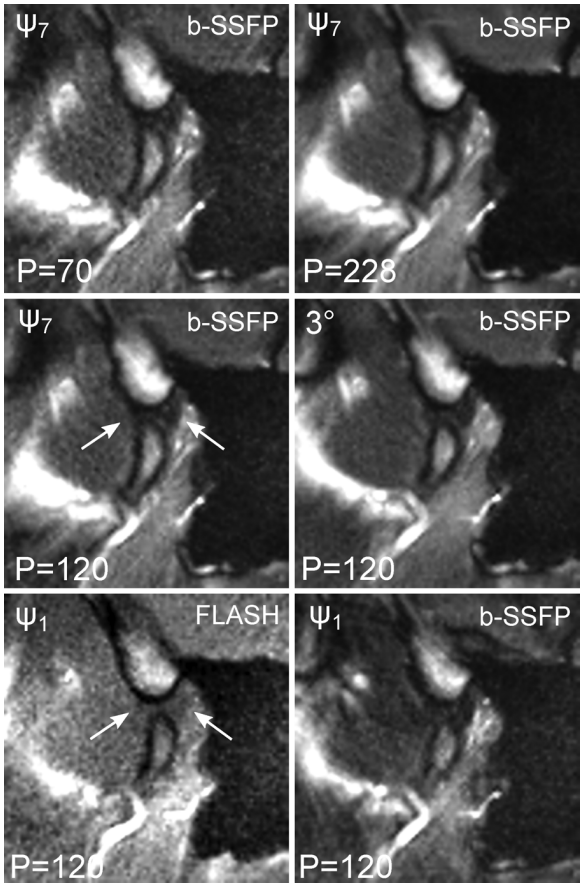

Fig. 8. Moving TMJ during its opening phase acquired with a b-SSFP and a FLASH sequence, using a radial trajectory with azimuthal increments of 3°, ψ_7, and ψ_1. Images acquired with ψ_7 were reconstructed with arbitrary window sizes of 70, 228, and 120 spokes (top row, center left) and show no additional artifacts compared to the reference image (center right). Image acquired with the golden angle ψ_1 and the b-SSFP sequence shows strong image artifacts (bottom right). Using the FLASH sequence the image artifacts disappear, at the cost of reduced SNR and reduced visibility of the discus (white arrows).

V. Discussion

In this work a modified golden ratio acquisition order using smaller angular increments has been introduced for radial MRI. The angular spacing is chosen according to a generalized Fibonacci sequence. It has been shown that the proposed order yields similar properties as the well-known golden angle acquisition order [3], but shows improved performance for balanced SSFP sequences with respect to eddy-current related artifacts. The existence of the tiny golden angles became evident in a numerical simulation of the sampling efficiency for all possible angular increments (Fig. 4). Similar results were reported previously in the field of theoretical biology using the distribution uniformity of leaves [19] and a shadow cast model [20] as objective functions.

It was shown previously that the golden angle increment guarantees a near uniform profile distribution for an arbitrary number of radial profiles. Using numerical simulation it was shown that for the practically relevant parameters the proposed

tiny golden angles guarantee a similar optimal sampling efficiency if at least a minimum of $2N+1$ radial profiles are used, thus enabling free choice of the retrospective reconstruction window.

For the reconstruction of extremely undersampled datasets from e.g., less than 8 radial k-space lines [4], the minimum of $2N+1$ radial profiles may seem like a limitation for $N = 5$ or higher. In this case however, selecting the first or second generalized Fibonacci number (e.g., $G_2^7 = 7$ or $G_3^7 = 8$) still guarantees a high sampling efficiency. In general, ψ_N has to be chosen application specific to ensure that N is large enough for a sufficiently small angular increment, and at the same time that N is small enough for a sufficiently small reconstruction window width.

One important application for the tiny golden angles that was examined in this work is time-resolved imaging with b-SSFP sequences. In combination with a b-SSFP sequence large angle increments may lead to strong image artifacts induced by rapidly changing eddy currents. An abrupt change of the field inhomogeneities generates deviations from the dynamic equilibrium and induces large signal fluctuations [17].

Through plane equilibration as described in [17] is to our experience not sufficient to fully compensate the large gradient steps involved with the golden angle ordering scheme. In the same work it was suggested to pair profiles that do approximately have the same angle. For time-resolved imaging this would however lead to a by a factor of two lowered temporal resolution.

The original publication by Winkelmann *et al.* also applied the golden angle ordering scheme to cardiac b-SSFP imaging on a 1.5T system. Despite the observations made by Bieri *et al.* [17], no severe image perturbations were observed in their work [3]. However, it is known that eddy-current effects are highly dependent on the MRI system and the actual gradient switching scheme. Their impact on the image quality in b-SSFP sequences is likely higher on 3T systems, which may explain the effects observed in this work. To our experience, eddy current effects due to large angle increments are also observable in b-SSFP images at 1.5T, but to a much lesser degree.

The experiments in this work showed that using the smaller azimuthal angle increments of the tiny golden angles significantly reduces the eddy current induced artifacts. The experiments showed that the strength of the image artifacts is difficult to predict. For instance, the artifacts in the cardiac experiment appeared much stronger than in the TMJ experiment. Furthermore, the phantom experiment showed that the image artifact level does not necessarily decrease strictly monotonic with decreasing angles [Fig. 6(b)]. However, in all cases an angle increment between ψ_5 and ψ_7 seemed sufficient to suppress most image artifacts to an acceptable level, which enables the combination of b-SSFP sequences with the tiny golden angle profile ordering.

In case of TMJ imaging, this result is important, since the T1/T2 contrast of the b-SSFP sequence is essential for imaging the discus articularis which in most cases is the main interest of the physician [31]. No fast sequence with a T2 dependent contrast is known that could replace the b-SSFP in this case.

In this work gridding reconstruction was used. In practical applications, parallel imaging [32], [33] and compressed sensing with an iterative reconstruction [14] could be used to increase the temporal resolution. The quasi-random property of the golden angle profile ordering with its incoherent aliasing artifacts [15] is essential for achieving a high temporal resolution in combination with compressed sensing bases approach, e.g., k-t SPARSE SENSE [4], [34]. The PSF analysis showed that the tiny golden angles exhibit similar incoherent point spread functions as the golden angle (Fig. 5) and should therefore work well with compressed sensing based approaches.

It should be possible to use most other applications that depend on the golden angle in conjunction with the introduced golden angle surrogates, e.g., time-resolved contrast enhancing [3], [10], single shot T1- or T2-mapping [9], [35], or self-gating [6], [7]. In future, other applications may be identified where a smaller surrogate for the golden angle may be beneficial, e.g., for the reduction of the acoustic noise during time-resolved acquisitions.

Appendix A

This work initially derived the tiny golden angles from a geometric construction. Alternatively, the angles could be derived directly from the generalized Fibonacci sequence using

$$\psi_N = \lim_{n\to\infty} \frac{\pi G_n^1}{G_{n+1}^N}.$$

Appendix B

Hypothesis: If n radial profiles are successively added spaced by the constant increment ψ_N, each additional profile after $n > N$ divides one of the currently largest azimuthal gaps by the golden ratio τ.

Lemma 1: All members of the sequence ψ_N are irrational.

Proof: All ψ_N can be expressed using an infinite continuous fraction and are thus irrational, see (7).

Lemma 2: If ψ_N is irrational, only two or three different gap sizes appear, and each additional profiles after $P > N$ divides one of the largest gaps.

The proof for Lemma 2 can be derived directly from the proof given by Knuth for any irrational angle ψ [22]. The following proofs the hypothesis using induction:

Invariant 1: Either three gap sizes a_n, b_n, c_n exist with $a_n/b_n = \tau$ and $b_n/c_n = \tau$ (which implies $a_n = b_n + c_n$), or two gap sizes a_n, b_n exist with $a_n/b_n = \tau$.

Proof by induction that Invariant 1 is valid for all $n \geq N$.

Induction Start: $n = N$: Two gap sizes exist, and Invariant 1 is clearly valid due to the definition of ψ_n through (2).

Inductive Step: If for the profile distribution n Invariant 1 is valid, show that for the profile distribution $n+1$ Invariant 1 is still valid.

Case 1: Three gap sizes a_n, b_n, c_n exist and a_n is not the last gap of its size.

Then the $(n+1)$th profile divides one of the largest gaps of size a_n (Lemma 2) into $a_n = b_n + c_n$ (no 4th gap size allowed due to Lemma 2 and $a_n \neq b_n + b_n$ due to Invariant 1).

$\Longrightarrow$ Three gap sizes $a_{n+1} = a_n$, $b_{n+1} = b_n$, and $c_{n+1} = c_n$ exists and Invariant 1 is valid for $n+1$.

Case 2: Three gap sizes a_n, b_n, c_n exist and a_n is the last gap of its size.
Then the $(n+1)$th profile divides the largest gap of size a_n (Lemma 2) still into $a_n = c_n + b_n$, since $a_n = d_n + b_n$ would imply $d_n = c_n$, and $a_n = d_n + e_n$ is not allowed due to Lemma 2.
$\Longrightarrow$ Two gap sizes $a_{n+1} = b_n$ and $b_{n+1} = c_n$ are left and Invariant 1 is valid for $n+1$.
Case 3: Two gap sizes a_n, b_n exist and a_n is not the last gap of its size.
Then the $(n+1)$th profile divides the largest gap of size a_n (Lemma 2) into $a_n = b_n + c_{n+1}$, since $a_n \neq b_n + b_n$ due to Invariant 1 and $a_n \neq c_{n+1} + c_{n+1}$ since ψ_n irrational. Since $a_{n+1} = a_n$ and $b_{n+1} = b_n$ follows:

$$\frac{b_{n+1}}{c_{n+1}} = \frac{b_n}{a_n - b_n} = \frac{b_n}{b_n\left(\frac{a_n}{b_n} - 1\right)} = \frac{1}{\frac{a_n}{b_n} - 1} = \frac{1}{\tau - 1} = \tau.$$

$\Longrightarrow$ Three gap sizes $a_{n+1} = a_n$, $b_{n+1} = b_n$, and $c_{n+1} = b_{n+1}/\tau$ exists and Invariant 1 is valid for $n+1$.
Case 4: Two gap sizes a_n, b_n exist and a_n is the last gap of its size.
This case never happens. For n to be of Case 3, $n-1$ had to be of Case 2. But Case 2 will always create at least two gaps of the size a_n.
$\Longrightarrow$ The Invariant 1 is valid for $n+1$ in all 3 cases. Together with Lemma 2 this proves the hypothesis.

REFERENCES

[1] P. C. Lauterbur, "Image formation by induced local interactions," *Nature*, vol. 242, no. 190, pp. 190–191, 1973.
[2] V. Rasche, R. de Boer, D. Holz, and R. Proksa, "Continuous radial data acquisition for dynamic MRI," *Magn. Reson. Med.*, vol. 34, no. 5, pp. 754–761, 1995.
[3] S. Winkelmann, T. Schaeffter, T. Koehler, H. Eggers, and O. Doessel, "An optimal radial profile order based on the Golden Ratio for time-resolved MRI," *IEEE Trans. Med. Imag.*, vol. 26, no. 1, pp. 68–76, Jan. 2007.
[4] L. Feng *et al.*, "Golden-angle radial sparse parallel MRI: Combination of compressed sensing, parallel imaging, and golden-angle radial sampling for fast and flexible dynamic volumetric MRI," *Magn. Reson. Med.*, vol. 72, no. 3, pp. 707–717, Sep. 2014.
[5] A. J. Hopfgartner *et al.*, "Dynamic MRI of the TMJ under physical load," *Dento Maxillo Facial Radiol.*, vol. 42, no. 9, Jan. 2013.
[6] J. Liu *et al.*, "Respiratory and cardiac self-gated free-breathing cardiac CINE imaging with multiecho 3D hybrid radial SSFP acquisition," *Magn. Reson. Med.*, vol. 63, pp. 1230–1237, May 2010.
[7] J. Paul *et al.*, "High-resolution respiratory self-gated golden angle cardiac MRI: Comparison of self-gating methods in combination with k-t SPARSE SENSE," *Magnet. Reson. Med.*, vol. 73, no. 1, pp. 292–298, Jan. 2015.
[8] A. D. Scott, R. Boubertakh, M. J. Birch, and M. E. Miquel, "Adaptive averaging applied to dynamic imaging of the soft palate," *Magn. Reson. Med.*, vol. 70, pp. 865–874, 2013.
[9] P. Ehses *et al.*, "IR TrueFISP with a golden-ratio-based radial readout: Fast quantification of T1, T2, and proton density," *Magn. Reson. Med.*, vol. 69, no. 1, pp. 71–81, Jan. 2013.
[10] H. K. Song and L. Dougherty, "k-space weighted image contrast (KWIC) for contrast manipulation in projection reconstruction MRI," *Magn. Reson. Med.*, vol. 44, no. 6, pp. 825–832, Dec. 2000.
[11] M. Doneva, "Advances in compressed sensing for magnetic resonance imaging," Ph.D. dissertation, Univ. Lübeck, Lübeck, Germany, 2011.
[12] M. Usman *et al.*, "Motion corrected compressed sensing for free-breathing dynamic cardiac MRI," *Magn. Reson. Med.*, vol. 70, pp. 504–516, 2013.
[13] M. Doneva, H. Eggers, J. Rahmer, P. Börnert, and A. Mertins, "Highly undersampled 3D golden ratio radial imaging with iterative reconstruction," in *Proc. Int. Soc. Mag. Reson. Med.*, 2008, vol. 16, p. 336.
[14] M. Lustig, D. L. Donoho, J. M. Santos, and J. M. Pauly, "Compressed sensing MRI," *IEEE Signal Process. Mag.*, vol. 25, no. 2, pp. 72–82, 2008.
[15] R. W. Chan, E. A. Ramsay, E. Y. Cheung, and D. B. Plewes, "The influence of radial undersampling schemes on compressed sensing reconstruction in breast MRI," *Magn. Reson. Med.*, vol. 67, pp. 363–377, 2012.
[16] A. Oppelt *et al.*, "FISP–A new fast MRI sequence," *Electromedia*, vol. 54, pp. 15–18, 1986.
[17] O. Bieri, M. Markl, and K. Scheffler, "Analysis and compensation of Eddy currents in balanced SSFP," *Magn. Reson. Med.*, vol. 54, pp. 129–137, 2005.
[18] C. M. Tsai and D. G. Nishimura, "Reduced aliasing artifacts using variable-density k-space sampling trajectories," *Magn. Reson. Med.*, vol. 43, pp. 452–458, Mar. 2000.
[19] C. Marzec and J. Kappraff, "Properties OT maximal spacing on a circle related to phyllotaxis and to the golden mean," *J. Theoret. Biol.*, vol. 103, pp. 201–226, 1983.
[20] S. King, F. Beck, and U. Lüttge, "On the mystery of the golden angle in phyllotaxis," *Plant, Cell Environ.*, vol. 27, pp. 685–695, 2004.
[21] A. F. Horadam, "A generalized fibonacci sequence," *Am. Math. Monthly*, vol. 69, no. 8, pp. 455–459, 1961.
[22] D. E. Knuth, *The Art of Computer Programming*. Palo Alto, CA: Addison-Wesley, 1973, vol. 3, p. 543.
[23] L. E. Dickson, *History of the Theory of Numbers, Vol. 1: Divisibility and Primality*. New York: Dover, 2005, pp. 393–411.
[24] S. Vajda, *Fibonacci and Lucas Numbers, and the Golden Section—Theory and Applications*. Chichester, U.K.: Ellis Horwood, 1989, p. 102.
[25] S. Zhang, N. Gersdorff, and J. Frahm, "Real-time magnetic resonance imaging of temporomandibular joint dynamics," *Open Med. Imag. J.*, vol. 5, pp. 1–7, 2011.
[26] A. Haase, D. Matthaei, W. Hänicke, and K.-D. Merboldt, "FLASH imaging. Rapid NMR imaging using low flip-angle pulses," *J. Magn. Reson.*, vol. 67, pp. 258–266, 1986.
[27] V. Rasche, R. Proska, R. Sinkus, P. Börnert, and H. Eggers, "Resampling of data between arbitrary grids using convolution interpolation," *IEEE Trans. Med. Imag.*, vol. 18, no. 5, pp. 385–392, May 1999.
[28] V. Rasche, D. Holz, and R. Proksa, "Multi-gradient-echo (prMGE) MRI," *Magn. Reson. Med.*, vol. 42, pp. 324–334, 1999.
[29] K. T. Block and M. Uecker, "Simple method for adaptive gradient-delay compensation in radial MRI," in *Proc. Int. Soc. Mag. Reson. Med.*, 2011, vol. 19, p. 2816.
[30] L. I. Rudin, S. Osher, and E. Fatemi, "Nonlinear total variation based noise removal algorithms," *Physica D*, vol. 60, pp. 259–268, 1992.
[31] S. J. Scrivani, D. a. Keith, and L. B. Kaban, "Temporomandibular disorders," *N. Eng. J. Med.*, vol. 359, no. 25, pp. 2693–2705, Dec. 2008.
[32] K. P. Pruessmann, M. Weiger, M. B. Scheidegger, and P. Boesiger, "SENSE: Sensitivity encoding for fast MRI," *Magn. Reson. Med.*, vol. 42, no. 5, pp. 952–962, Nov. 1999.
[33] M. A. Griswold *et al.*, "Generalized autocalibrating partially parallel acquisitions (GRAPPA)," *Magn. Reson. Med.*, vol. 47, no. 6, pp. 1202–1210, Jun. 2002.
[34] S. Wundrak, J. Paul, J. Ulrici, E. Hell, and V. Rasche, "Sparse dynamic MRI of the temporomandibular joint," in *Proc. Int. Soc. Mag. Reson. Med.*, 2014, vol. 9, p. 1267, 1.
[35] S. Winkelmann, T. Schaeffter, H. Eggers, T. Nielsen, and O. Doessel, "Single shot T1-Mapping, using a radial look-locker sequence and an optimal profile order determined by the golden cut," in *Proc. Int. Soc. Mag. Reson. Med.*, 2005, p. 2196.

Chapter 5

Golden Ratio Sparse MRI using Tiny Golden Angles (reprinted article)

This article [147] was published as

Wundrak, S., Paul, J., Ulrici, J., Hell, E., Geibel, M.-A., Bernhardt, P., Rottbauer, W., and Rasche, V. Golden Ratio Sparse MRI Using Tiny Golden Angles. *Magnetic Resonance in Medicine*: doi:10.1002/mrm.25831, 2015

NOTE

Magnetic Resonance in Medicine 00:00–00 (2015)

Golden Ratio Sparse MRI Using Tiny Golden Angles

Stefan Wundrak,[1,2]* Jan Paul,[1] Johannes Ulrici,[2] Erich Hell,[2] Margrit-Ann Geibel,[3] Peter Bernhardt,[1] Wolfgang Rottbauer,[1] and Volker Rasche[1]

Purpose: The combination of fully balanced SSFP sequences with iterative golden angle radial sparse parallel (iGRASP) MRI leads to strong image artifacts due to eddy currents caused by the large angular increment of the golden angle ordering. The purpose of this work is to enable the combination of iterative golden angle radial sparse parallel MRI with balanced SSFP using the recently presented tiny golden angles.

Methods: The tiny golden angle trajectories are analyzed for their incoherence properties in relation to sparse imaging using the time-resolved point-spread functions. Tiny golden angle radial sparse parallel (tyGRASP) MRI is introduced and evaluated with applications in cardiac imaging and dynamic imaging of the temporomandibular joint. The results are analyzed in detail for 3 T and verified for 1.5 T.

Results: The incoherence properties of the tiny golden angle trajectory are comparable to the incoherence properties of the golden angle trajectory and are well suited for sparse MRI reconstruction. The proposed tiny golden angle radial sparse parallel MRI method strongly reduces eddy current related artifacts for both applications.

Conclusion: This work enables sparse, golden-ratio-based imaging with balanced SSFP sequences. **Magn Reson Med 000:000–000, 2015. © 2015 Wiley Periodicals, Inc.**

Key words: cine; cardiac; TMJ; sparse MRI; golden angle; compressed sensing; iGRASP

INTRODUCTION

Balanced steady-state free precession sequences (b-SSFP) are known in MRI to provide very high signal-to-noise ratio and T2/T1-weighted image contrast. It has become the de facto standard for cardiovascular magnetic resonance imaging at 1.5 Tesla (1). Cardiac imaging benefits from the intrinsic flow compensation of b-SSFP, which reduces artifacts and enhances the signal of inflowing blood (2). Furthermore, the T2/T1-weighted contrast of b-SSFP sequences allows, for example, the imaging of the articular disc of the temporomandibular joint (TMJ) with short pulse repetition time (TR) (3). In particular, b-SSFP sequences are commonly used for real-time MR imaging (3–5).

[1]Department of Internal Medicine II, University Hospital of Ulm, Ulm, Germany.
[2]Sirona Dental Systems, Bensheim, Ulm, Germany.
[3]Department of Oral and Maxillofacial Surgery, University of Ulm, Ulm, Germany.

*Correspondence to: Stefan Wundrak, Dipl. Inf., Department of Internal Medicine II, University Hospital of Ulm, Germany. E-mail: stefan.wundrak@uni-ulm.de

Received 18 March 2015; revised 30 April 2015; accepted 26 May 2015
DOI 10.1002/mrm.25831
Published online 00 Month 2015 in Wiley Online Library (wileyonlinelibrary.com).

Sparse MRI (6) is an acceleration strategy that exploits spatial and temporal image sparsity to reconstruct the original signal from incoherently undersampled measurements using techniques known from compressed sensing (CS) (7). Various approaches for CS in MRI have been proposed (6,8,9). Recently, iterative golden angle radial sparse parallel MRI (iGRASP) was introduced (10), which uses sparse MRI in combination with parallel imaging (11). Golden angle radial k-space trajectories (12) are well suited for sparse MRI due to their incoherent aliasing artifacts (13,14) and their low sensitivity to motion (15). The iGRASP method is able to reconstruct time-resolved cardiovascular images from as low as 21 radial profiles per time frame.

The large angular increment (111.246°) of the golden angle trajectory leads to rapidly changing eddy currents in the conducting part of the magnet, and in turn to rapidly varying field inhomogeneities. The steady-state of the b-SSFP sequence is especially sensitive for these varying eddy current effects and may exhibit strong signal fluctuations (16). This effect often prohibits the combination of iGRASP with the b-SSFP sequence. In (17), a profile ordering using tiny golden angles was introduced that has comparable properties to the golden angle without rapid gradient changes.

The purpose of this work is to evaluate the combination of iGRASP with b-SSFP. First, the incoherence properties of the tiny golden angles are analyzed, then the tiny golden angle radial sparse parallel MRI (tyGRASP) method is introduced and verified with applications in cardiac imaging and imaging of the TMJ.

METHODS

Iterative Golden Angle Radial Sparse Parallel MRI

Sparse MRI requires a variable density sampling scheme that leads to incoherent aliasing (6,18). Radial trajectories naturally fulfill this requirement by densely sampling the k-space center. The radial golden angle profile ordering ensures an optimal sampling efficiency for an arbitrary number of consecutive profiles (12). Furthermore, the golden angle leads to a quasirandom distribution of radial profiles which leads to temporal incoherent aliasing artifacts (14) that is a fundamental requirement for CS (19). The iGRASP method combines golden angle radial sampling with CS and parallel imaging (10). In the following, the iGRASP technique is described as used in this work. First, radial k-space profiles are acquired continuously using the golden angle profile ordering and are sorted into a time-series of frames. Images are reconstructed iteratively by solving the nonlinear reconstruction problem

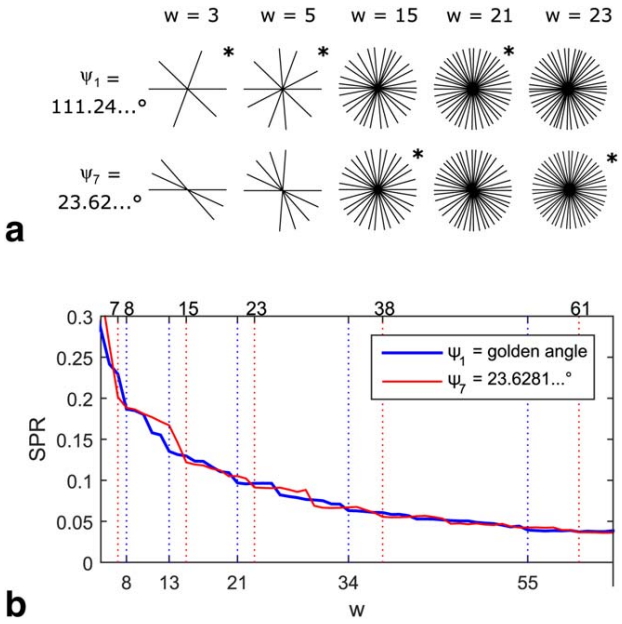

FIG. 1. Golden angle ordering ψ_1 compared to tiny golden angle ordering ψ_7. a: Both exhibit a near optimal radial profile distribution if $w > 2N$, especially if w is an element of the generalized Fibonacci sequence G^N (marked with $*$). b: Incoherence of the tiny golden angle sampling trajectory ψ_7 analyzed using the SPR in the time-resolved point spread functions. Red and blue dotted lines indicate the generalized Fibonacci numbers G^N. Both trajectories show similar SPRs, with a slightly better incoherence for ψ_N if $w \in G^N$.

$$\underset{x}{\operatorname{argmin}} ||F \cdot S \cdot x - b||_2^2 + \lambda_t ||\nabla_t x||_1 + \lambda_s ||\nabla_s x||_1, \quad [1]$$

$$b = \begin{bmatrix} b_1 \\ \vdots \\ b_c \end{bmatrix}, S = \begin{bmatrix} S_1 \\ \vdots \\ S_c \end{bmatrix}, F = \begin{pmatrix} \hat{F} & \dots & 0 \\ \vdots & \ddots & \vdots \\ 0 & \dots & \hat{F} \end{pmatrix} \quad [2]$$

where $\hat{F}$ is the nonuniform Fourier transformation from Cartesian $x - t$ to radial $k - t$ space and S contains the coil sensitivity maps for all c coils. The l_2-norm enforces data consistency between the $k - t$ space samples b and the reconstructed image sequence x in $x - t$ space. ∇_s and ∇_t denote the gradient operator along the spatial and temporal dimension, respectively. The combination of ∇ with the l_1-norm forms the total variation regularization, which exploits sparsity of $\nabla_s x$ and $\nabla_t x$ by assuming a piecewise constant signal function for each pixel in space and over time (20), resulting in most coefficients of $\nabla_t x$ and $\nabla_s x$ to be zero.

Tiny Golden Angles

Tiny golden angles (17) are small irrational angles that exhibit properties similar to the original golden angle. Tiny golden angles are defined using the golden ratio $\tau = (1 + \sqrt{5})/2$ and the sequence

$$\psi_N = \pi/(\tau + N - 1), \quad N = 1, 2, \dots . \quad [3]$$

The first two members of this sequence are the well-known golden angle $\psi_1 = 111.246...^\circ$ and the complementary small golden angle $\psi_2 = 180^\circ - 111.246...^\circ$. The angles $\psi_{N>2}$ are called tiny golden angles ($\psi_3 = 49.750...^\circ$, $\psi_4 = 38.977...^\circ$, $\psi_5 = 32.039...^\circ$, $\psi_6 = 27.198...^\circ$, $\psi_7 = 23.628...^\circ$, ...) which have the same optimal properties regarding the radial profile distribution for an arbitrary reconstruction window size w, if more than $2N$ radial profiles are used (Fig. 1a). The angle ψ_N leads to the most uniform distribution if w is an element of the generalized Fibonacci sequence (17)

$$G_1^N = 1; G_2^N = N; G_n^N = G_{n-1}^N + G_{n-2}^N \quad [4]$$

where the first sequence G^1 is the well known Fibonacci sequence and, for example, $G^7 = 1, 7, 8, 15, 23, 38, \dots$ the generalized Fibonacci sequence for ψ_7.

Incoherence Properties of the Tiny Golden Angles

Sparse MRI reconstruction presumes a sampling trajectory with incoherent aliasing artifacts (6). The less coherent aliasing of the golden angle sampling scheme compared with uniform radial sampling was previously shown in (21). To analyze the incoherence properties of the tiny golden angle sampling trajectories in comparison to the golden angle trajectory, the point spread functions (6) were calculated for a sequence of time frames using

$$PSF_{i,j} = e_j^H F^H F e_i \quad [5]$$

where e_i is the ith canonical basis vector. The point spread functions were calculated for ψ_1 to ψ_7, for a reconstruction window width w of 5 to 60, and a resolution of 256 × 256 pixel. The sidelobe-to-peak ratio (SPR) (6), which is directly related to the mutual incoherence (22), was used as a measure for coherence and was calculated for each frame using

$$\mathrm{SPR} = \max_{i \neq j} \left(\frac{\mathrm{PSF}_{i,j}}{\mathrm{PSF}_{i,i}} \right) \quad [6]$$

and combined along the temporal dimension using the maximum intensity projection (14). A lower SPR means lower coherence and better characteristic for the CS reconstruction (22).

Tiny Golden Angle Radial Sparse Parallel MRI

The proposed tyGRASP method is equivalent to iGRASP described by Eq. 1 with the difference that a tiny golden angle trajectory is used for the acquisition process. The angle ψ_7 was used in all experiments, as it was, on the one hand, sufficiently small to avoid most b-SSFP related artifacts and, on the other hand, the minimum window width $w > 2N + 1 = 15$ is still sufficiently small for fast imaging with a high temporal resolution.

The objective function (1) was minimized using a nonlinear conjugate gradient solver with corner rounding (6) for the gradient calculation of the $l1$-term and an inexact backtracking line search. The system was left-preconditioned using the square root of the k-space sampling density function (23) and the solver was terminated after 100 iterations in all cases. The k-space data

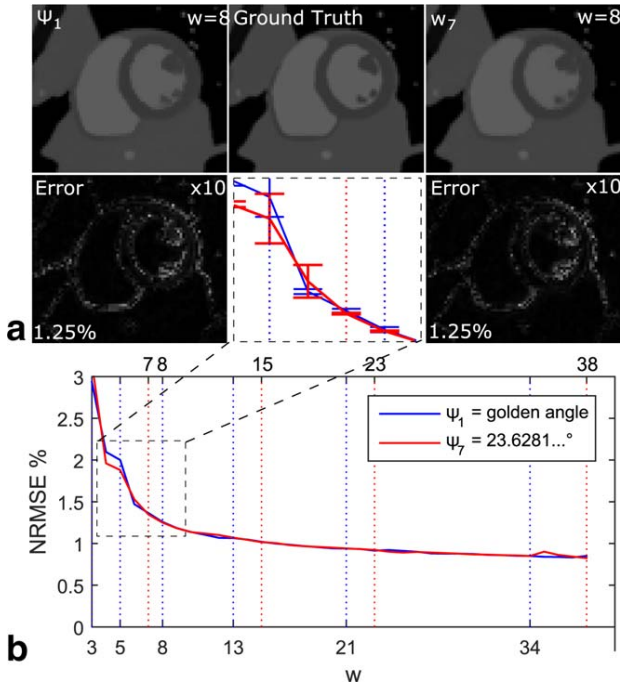

FIG. 2. Numerical heart phantom reconstructed with tyGRASP and varying window size *w*. a: Reconstruction with $w = 8$ spokes (cropped) shows highest errors at the moving myocardium border with no apparent difference in image quality between ψ_1 and the tiny golden angle ψ_7. b: Images show about the same NRMSE for both angles and all *w*. For $w < 8$, the solver did not converge reliably due to noise and high undersampling, leading to higher variance in NRMSE.

were normalized to an arbitrary l_2-norm of 100 multiplied by the number of time-frames.

Simulation

A simulation experiment was performed using the numerical cardiac phantom MRXCAT (24), the angles ψ_1 to ψ_7, and a varying window width *w* of 3 to 40 spokes per frame. Simulation parameters were: reconstruction matrix 256 × 256, 24 time frames, 16 coils, added Gaussian noise to yield an SNR of 35. The regularization was fixed to $\lambda_t = 0.005$ and $\lambda_s = 0.0005$, based on preliminary experiments to minimize the normalized root mean square error (NRMSE) for $w = 8$ and $w = 30$. The experiments were repeated ten times with a different random noise seed. For the resulting images the NRMSE to the noise free ground truth was calculated.

Volunteer Studies

The tyGRASP method was verified in volunteer studies for cardiovascular magnetic resonance imaging and imaging of the TMJ. All studies were approved by the local ethics committee and written informed consent was obtained prior to the examination. All scans were performed on a Philips 3T Achieva system (Philips Healthcare, Best, The Netherlands). As a measure for the noise level and residual artifacts, the signal variation was estimated from the magnitude in all images and averaged. The coefficients of variation were calculated as the standard deviation divided by the mean value in 5 × 5 pixel masks over all time frames.

Cardiac Experiment

Dynamic short axis time-resolved cardiac data sets were acquired from five healthy volunteers during a 2.3 s breathhold. A radial trajectory with the the radial angle increments ψ_1 and ψ_7 was used in combination with a b-SSFP and a FLASH sequence. The parameters for the b-SSFP sequence were: TR/TE = 2.3/1.15 ms, flip angle 43°, resolution 2.3 × 2.3 mm^2, slice thickness 8 mm, acquisition matrix 148 × 148. The FLASH sequence was used with the same parameters, except for TR/TE = 2.3/1.6 ms and flip angle = 15°. Coil sensitivity maps for the 32 coils where acquired using a separate calibration scan. The regularization parameter were set manually to $w = 23$, $\lambda_t = 0.04$ and $\lambda_s = 0.001$ based on experiments to optimize the perceived image quality. A verification data set was acquired on a second MR system (Philips 1.5T Ingenia) to account for the system dependent influence of eddy currents, using the same parameters as on the 3T system.

TMJ Experiment

Sagittal images of the TMJ of five healthy volunteers were acquired by means of a 2 × 4 channel carotid coil (Chenguang Medical Technologies, Shanghai, China) using a b-SSFP and a FLASH sequence. The parameters for the b-SSFP sequence were: TR/TE = 4.6/2.3 ms, flip angle 48°, resolution 0.75 × 0.75 mm^2, slice thickness 5 mm, acquisition matrix 256 × 256. The FLASH sequence was used with the same parameters, except for TR/TE = 4.8/2.3 ms, flip angle 20°. The data were acquired using the radial angle increments ψ_1 and ψ_7. The reconstruction parameters were set manually to $w = 38$, $\lambda_t = 0.05$ and $\lambda_s = 0.002$ after experiments to reach the best perceived image quality. The volunteers were instructed to open the mouth in about 4 s, as uniformly as possible, and to close it again in about 4 s.

RESULTS

Coherence Analysis

Figure 1b shows the SPR of ψ_1 and ψ_7 as a function of the window width *w*. The plots for ψ_3 to ψ_9 can be found in the Supporting Information (Supporting Information Fig. S6). Generally, for $w \in G^1$ the ψ_1 are more incoherent (blue dotted lines) and for $w \in G^N$ the ψ_N are more incoherent (red dotted lines). For $w < 2N$ the golden angle is better than ψ_N, except if $w \in G^N$. The mean SPR difference between ψ_N and ψ_1 with $w > 2N$ is below 0.002, the minimum and maximum difference is in the range $[-0.018; 0.019]$. This means, that for $w > 2N$, all angles ψ_N define a sampling trajectory that has a similar level of incoherence as the original golden angle trajectory.

Simulation

Figure 2a shows the numerical phantom reconstructed with tyGRASP using radial trajectories and angular

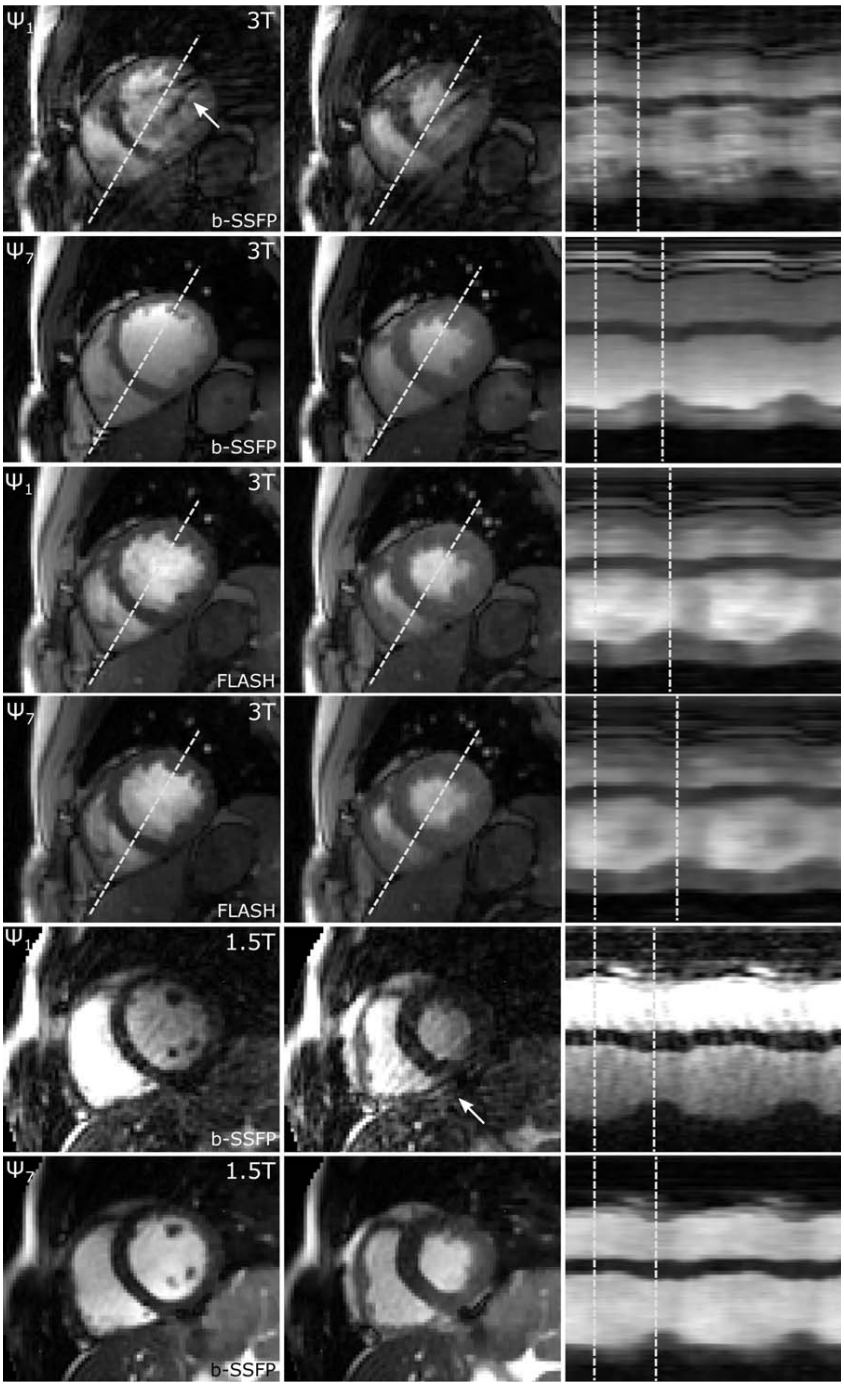

FIG. 3. Diastole (left), systole (middle), and M-mode plots of cardiac short-axis views reconstructed with tyGRASP and $w = 23$ profiles. The balanced sequence at 3 T shows very strong eddy current related artifacts (arrow—top row). The artifacts disappear if the smaller tiny golden angle ψ_7 is used (second row). FLASH in combination with the golden angle sequence does not show similar artifacts (fourth row). Similar artifacts are observed for the 1.5 T system (fifth and sixth row).

increments of ψ_1 and ψ_7, as well as a window width of $w = 8$. Both images exhibit the same image quality with artifacts mainly around the moving myocard, and the same NRMSE of 1.25%. Figure 2b shows the NRMSE for ψ_1 and ψ_7 for a range of window width w. Both angles led to about the same NRMSE for all w. Increased error ranges occurred for $w < 8$ as the combination of noise and high undersampling led to a lower convergence. In contrast to the point spread function analysis, there is no improvement for $w \in G^N$.

Cardiac Experiment

Figure 3 shows short axis views of the heart in systolic and diastolic state and corresponding M-mode plots. The images acquired with the golden angle ψ_1 and the b-SSFP sequence show strong eddy current and aliasing artifacts. The images acquired using ψ_7 exhibit a clearly improved image quality and show no apparent eddy current or aliasing artifacts. The FLASH sequence shows about the same level of artifacts for ψ_1 and ψ_7. For b-

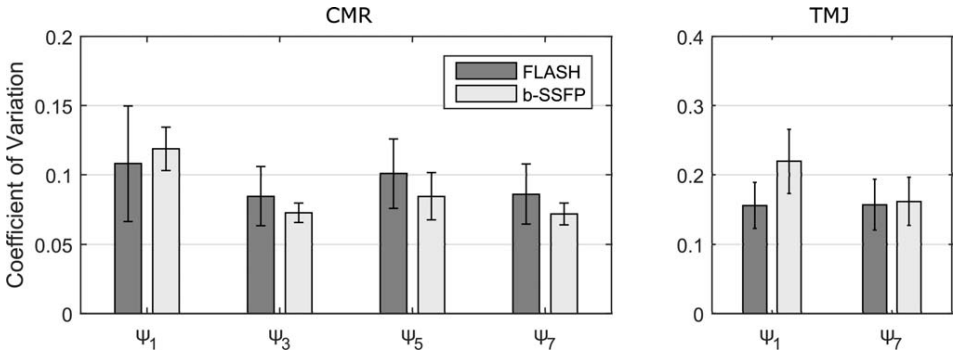

FIG. 4. Coefficient of variation of the left ventricle (left) and the TMJ (right) for all acquisitions. Lower signal variation indicates less image artifacts. The angular increment of the golden ratio trajectory has a strong influence on the signal variation.

SSFP sequence, the mean coefficient of variation of the left ventricle (blood pool and myocardium) is reduced from 0.12 $\pm$0.02 for ψ_1 to 0.07 $\pm$0.01 for ψ_7 (Fig. 4). The effect is stronger for b-SSFP than for FLASH sequences. Videos of this data set and of more volunteers can be found in the Supporting Information (Supporting Information Video S1 and S2). Similar effects appear for the second 1.5T MR system. The ψ_1 scan shows strong image artifacts that do not appear for ψ_7 (Fig. 3 bottom, Supporting Information Video S3).

TMJ Experiment

Figure 5 shows sagittal views of the TMJ in opened and in moving state, and M-mode plots of a profile through the moving condyle head. The images acquired with ψ_1 and b-SSFP show eddy current artifacts, which are particularly strong for the articular disc (arrow). The images at ψ_7 show clearly improved image quality with no apparent eddy current artifacts. The mean coefficient of variation is reduced from 0.22 $\pm$0.05 for ψ_1 to 0.16 $\pm$0.03 for

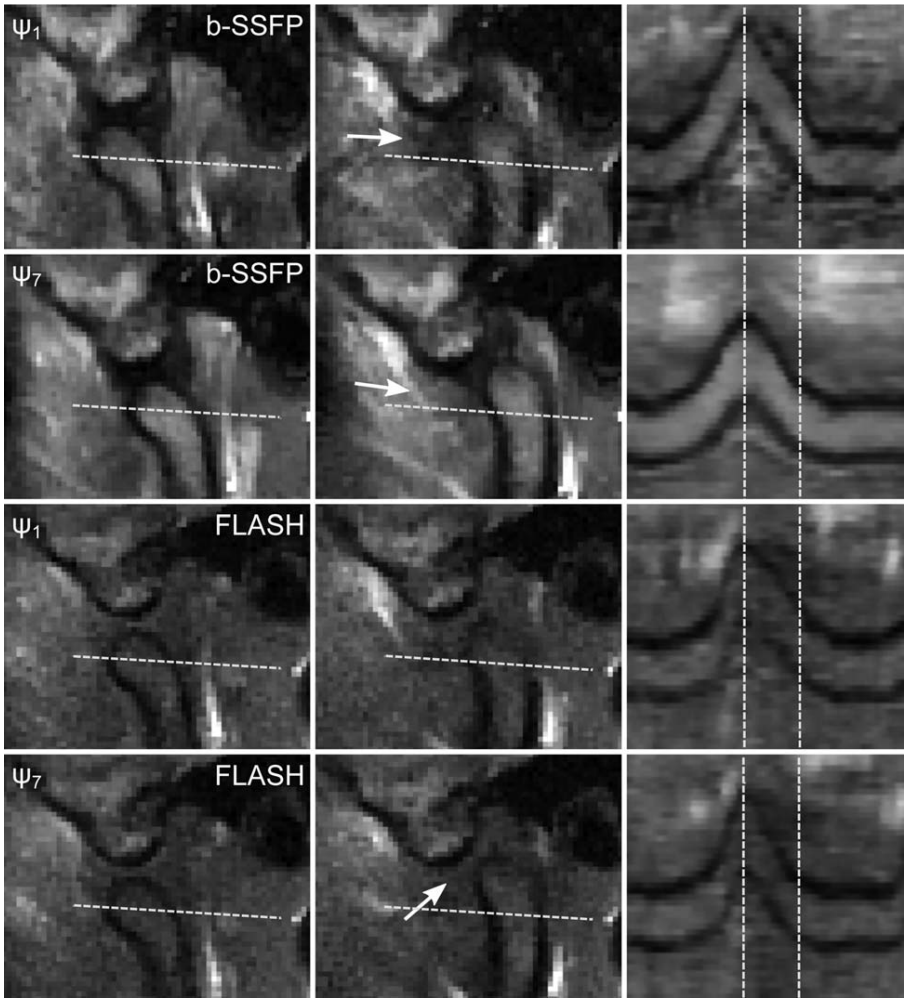

FIG. 5. Moving TMJ reconstructed using tyGRASP with a golden angle and a tiny golden angle trajectory: in closed condyle position (left), during condyle movement (middle), and M-mode plots (right). The golden angle trajectory leads to strong image artifacts (top row, arrow) that do not occur with the tiny golden angle ψ_7 (second row). The FLASH sequence does not show artifacts at the cost of SNR and the visibility of the discus articularis (bottom row, arrow).

ψ_7 (Fig. 4). The condyle head remains sharp through all motion phases. The images acquired with the FLASH sequence are not affected by eddy current artifacts, but at the cost of visibility of the articular disc [see (25)] and lower SNR. Videos are part of the supporting material (Supporting Information Video S4 and S5).

DISCUSSION

The aim of this work was to combine iterative golden angle radial parallel MRI with balanced SSFP on 3T systems. So far, the combination of both methods was not feasible, as the large angular increment of the golden angle led to eddy current related artifacts. Therefore, it was evaluated if the tiny golden angles are sufficient to replace the golden angle ordering in iterative golden angle radial sparse parallel MRI.

The incoherence analysis showed that the tiny golden angle trajectories exhibit comparable incoherence to the golden angle if the window width is $w > 2N$. Simulations using a numerical phantom and the tyGRASP reconstruction confirmed that the tiny golden angles and the golden angle led to comparable results. There was no noticeable visual difference, no significant difference in NRMSE, and no difference in convergence between ψ_1 and the smaller angles if $w > 2N$. This suggests that the tiny golden angles are a good surrogate for ψ_1 in golden ratio based sparse MRI.

For the rest of the work, we focused on ψ_7, which is sufficiently small to avoid most eddy current related artifacts (17), while still being large enough to ensure a window width of $2N + 1 = 15$ that is sufficient for most real-time applications. If a smaller window size is needed, the first or second generalized Fibonacci number ($w = G_2^7 = 7$, $w = G_3^7 = 8$) still guarantees good sampling efficiency and better incoherence than ψ_1 (see Fig. 1). Fewer than 7 radial profiles per window are usually not used; however, a window width of 5 or 6 could be achieved with the second generalized Fibonacci number of ψ_5 and ψ_6.

Due to the more stable steady-state of FLASH sequences, the large angular increment did not show any apparent eddy current related artifacts. For cardiac images, the coefficient of variation however decreased for tiny golden angles (Fig. 4). Similar effects for FLASH sequences were already reported (26) and are related to gradient spoilers that are rotated with the projection direction. The large angular increment reduces the spoiler efficiency and leads to artifacts caused by incomplete spoiling. In previous work, these spoiling related artifacts appeared in combination with CG-SENSE and could be reduced (27) using the previously known small golden angle $\psi_2 = 68.75^\circ$.

In combination with the less stable steady-state of the b-SSFP sequence the images were strongly affected and showed strong eddy current artifacts and convergence problems. This was previously described for permanently and abruptly changing gradient schemes (16,17). Iterative reconstruction could not suppress these image artifacts, as not undersampling, but inconsistencies in k-space data are the source of artifacts. This is evident, as the artifacts in Figure 3 (arrow) were also visible in the fully sampled images. These artifacts could also not be caused by static off-resonance ("banding artifacts") (2), as these artifacts would also appear for ψ_7.

Due to through plane motion and through plane flow in both applications, parts of the images are likely measured in transient state (28). To exclude the possibility, that transient signal oscillation is the dominating cause for the observed differences between the ψ_1 and ψ_7 trajectories, a resting TMJ was scanned. Even though steady state conditions were certainly reached, a similar dependence of image artifacts was observed (see Supporting Information Fig. S7).

Previous work reported a varying appearance and strength of eddy-current effects with b-SSFP sequences (16,17,29–31), likely due to the strong system dependent appearance of eddy-currents. Even though the reduction of image artifacts by the smaller angle ψ_7 was verified on a second MRI system (Fig. 3), eddy current effects remain generally hard to predict.

The results from cardiac imaging were also confirmed for TMJ imaging. This result is important for time-resolved imaging of the TMJ, as the T2/T1 contrast of the b-SSFP sequence is essential for imaging of the discus articularis which usually is the main interest of the physician (32). No fast sequence with a T2 dependent contrast is known that could replace b-SSFP in this case.

In conclusion, the tiny golden angles enable b-SSFP imaging in combination with the advantages of golden ratio based iterative image reconstruction.

ACKNOWLEDGMENT

The authors thank Dr. Uta Denzel and Dr. Andreas Niedermayr for patient guidance.

REFERENCES

1. Plein S, Bloomer TN, Ridgway JP, Jones TR, Bainbridge GJ, Sivananthan MU. Steady-state free precession magnetic resonance imaging of the heart: comparison with segmented k-space gradient-echo imaging. J Magn Reson Imaging 2001;14:230–236.
2. Bieri O, Scheffler K. Fundamentals of balanced steady state free precession MRI. J Magn Reson Imaging 2013;11:2–11.
3. Zhang S, Uecker M, Voit D, Merboldt KD, Frahm J. Real-time cardiovascular magnetic resonance at high temporal resolution: radial FLASH with nonlinear inverse reconstruction. J Cardiovasc Magn Reson 2010;12:39–37.
4. Voit D, Zhang S, Unterberg-Buchwald C, Sohns JM, Lotz J, Frahm J. Real-time cardiovascular magnetic resonance at 1.5 T using balanced SSFP and 40 ms resolution. J Cardiovasc Magn Reson 2013;15:79
5. Aandal G, Nadig V, Yeh V, Rajiah P, Jenkins T, Sattar A, Griswold M, Gulani V, Gilkeson RC, Seiberlich N. Evaluation of left ventricular ejection fraction using through-time radial GRAPPA. J Cardiovasc Magn Reson 2014;16:1–13.
6. Lustig M, Donoho D, Pauly JM. Sparse MRI: the application of compressed sensing for rapid MR imaging. Magn Reson Med 2007;58: 1182–1195.
7. Donoho DL. Compressed sensing. IEEE Trans Inf Theory 2006;52: 1289–1306.
8. Gamper U, Boesiger P, Kozerke S. Compressed sensing in dynamic MRI. Magn Reson Med 2008;59:365–373.
9. Otazo R, Sodickson DK. Distributed compressed sensing for accelerated MRI. In Proceedings of International Society for Magnetic Resonance in Medicine, Honolulu, 2009, vol 17. p. 378.
10. Feng L, Grimm R, Tobias Block K, Chandarana H, Kim S, Xu J, Axel L, Sodickson DK, Otazo R. Golden-angle radial sparse parallel MRI: combination of compressed sensing, parallel imaging, and golden-

angle radial sampling for fast and flexible dynamic volumetric MRI. Magn Reson Med 2013;72:707–717.
11. Blaimer M, Breuer F, Mueller M, Heidemann RM, Griswold M, Jakob PM. SMASH, SENSE, PILS, GRAPPA - how to choose the optimal method. Top Magn Reson Imaging 2004;15:223–236.
12. Winkelmann S, Schaeffter T, Koehler T, Eggers H, Doessel O. An optimal radial profile order based on the golden ratio for time-resolved MRI. IEEE Trans Med Imaging 2007;26:68–76.
13. Block KT, Uecker M, Frahm J. Undersampled radial MRI with multiple coils. Iterative image reconstruction using a total variation constraint. Magn Reson Med 2007;57:1086–1098.
14. Chan RW, Ramsay EA, Cheung EY, Plewes DB. The influence of radial undersampling schemes on compressed sensing reconstruction in breast MRI. Magn Reson Med 2012;67:363–377.
15. Rasche V, de Boer R, Holz D, Proksa R. Continuous radial data acquisition for dynamic MRI. Magn Reson Med 1995;34:754–761.
16. Bieri O, Markl M, Scheffler K. Analysis and compensation of eddy currents in balanced SSFP. Magn Reson Med 2005;54:129–137.
17. Wundrak S, Paul J, Ulrici J, Hell E, Rasche V. A small surrogate for the golden angle in time-resolved radial MRI based on generalized fibonacci sequences. IEEE Trans Med Imaging 2014;34.
18. Adcock B, Hansen AC, Poon C, Roman B. Breaking the coherence barrier: a new theory for compressed sensing. arXiv 2014:1302.0561v.
19. Candès EJ, Wakin MB. An introduction to compressive sampling. IEEE Signal Process Mag 2008;25:21–30.
20. Adluru G, McGann C, Speier P, Kholmovski EG, Shaaban A, Dibella EVR. Acquisition and reconstruction of undersampled radial data for myocardial perfusion magnetic resonance imaging. J Magn Reson Imaging 2009;29:466–473.
21. Doneva M. Advances in compressed sensing for magnetic resonance imaging. Ph.D. thesis. Universität zu Lübeck, Washington, 2011.
22. Haldar JP, Member S, Hernando D, Liang Zp. Compressed-sensing MRI with random encoding. IEEE Trans Med Imaging 2011;30:893–903.
23. Pruessmann KP, Weiger M, Börnert P, Boesiger P. Advances in sensitivity encoding with arbitrary k-space trajectories. Magn Reson Med 2001;46:638–651.
24. Wissmann L, Santelli C, Segars WP, Kozerke S. MRXCAT: realistic numerical phantoms for cardiovascular magnetic resonance. J Cardiovasc Magn Reson 2014;16:2–11.
25. Zhang S, Gersdorff N, Frahm J. Real-time magnetic resonance imaging of temporomandibular joint dynamics. Open Med Imaging J 2011;5:1–7.
26. Vakil P, Ansari SA, Hurley MC, Bhat H, Batjer HH, Bendok BR, Carroll TJ. Magentization spoiling in radial FLASH contrast enhanced MR digital subtraction angiography. J Magn Reson Imaging 2012;36:249–258.
27. Speier P, Hansen MS. A Golden Angle of 68.75° improves gradient spoiling in radial GRE. In Proceedings of International Society for Magnetic Resonance in Medicine, Milan, 2014, vol 22. p. 4245.
28. Scheffler K. On the transient phase of balanced SSFP sequences. Magn Reson Med 2003;49:781–783.
29. Winkelmann S, Schaeffter T, Eggers H, Nielsen T, Doessel O. Single shot T1-mapping, using a radial look-locker sequence and an optimal profile order determined by the golden cut. In Proceedings of International Society for Magnetic Resonance in Medicine, Miami, 2005, p. 2196.
30. Nielsen Jf, Nayak KS. Interleaved balanced SSFP imaging: artifact reduction using gradient waveform grouping. J Magn Reson Imaging 2009;29:745–750.
31. Sayin O, Derbyshire Ja, McVeigh E, Herzka D. Through-slice dephasing for eddy current artifact reduction in bSSFP. J Cardiovasc Magn Reson 2012;14:271.
32. Scrivani SJ, Keith DA, Kaban LB. Temporomandibular disorders. New Eng J Med 2008;359:2693–2705.

SUPPORTING INFORMATION

Additional Supporting Information may be found in the online version of this article.

Supporting Video S1: This video supports Figure 3 and shows the short-axis view acquired with ψ_1 and ψ_7 at 3T.

Supporting Video S2: This video shows another volunteer in short-axis view acquired with ψ_1 and ψ_7 at 3T.

Supporting Video S3: This video shows another volunteer in short-axis view acquired with ψ_1 and ψ_7 at 1.5T.

Supporting Video S4: This video supports Figure 3 and shows the moving TMJ acquired with ψ_1 and ψ_7.

Supporting Video S5: This video of the moving TMJ shows another volunteer acquired with ψ_1 and ψ_7.

Supporting Figure S6: This figure supports Figure 1 and shows the SPR for the tiny golden angles ψ_3 to ψ_9.

Supporting Figure S7: Non-moving TMJ scanned at 3T using a b-SSFP sequence and the angles ψ_1 and ψ_1.

Chapter 6

A Self-Gating Method for Time-Resolved Imaging of Nonuniform Motion (reprinted article)

This article [146] was published as

Wundrak, S., Paul, J., Ulrici, J., Hell, E., Geibel, M.-A., Bernhardt, P., Rottbauer, W., and Rasche, V. A Self-Gating Method for Time-Resolved Imaging of Nonuniform Motion. *Magnetic Resonance in Medicine*: doi:10.1002/mrm.26000, 2015

NOTE

Magnetic Resonance in Medicine 00:00–00 (2015)

A Self-Gating Method for Time-Resolved Imaging of Nonuniform Motion

Stefan Wundrak,[1,2]* Jan Paul,[1] Johannes Ulrici,[2] Erich Hell,[2] Margrit-Ann Geibel,[3] Peter Bernhardt,[1] Wolfgang Rottbauer,[1] and Volker Rasche[1]

Purpose: To develop a self-gating method capable of assessing nonuniform motion, e.g., in cardiovascular magnetic resonance imaging of patients with severe arrhythmia, or for imaging of the temporomandibular joint.
Methods: The proposed method allows cyclic motion trajectories with a nonuniform pace by replacing the one-dimensional gating signal of conventional image-based self-gating with a two-dimensional gating matrix. The resulting image quality is compared with conventional self-gating and real-time MRI.
Results: Nonuniform self-gating resulted in superior image quality compared with conventional self-gating and the feasibility study showed significantly improved image sharpness ($P < 0.01$). Further, improvements in image quality were shown compared with golden angle radial parallel sparse MRI.
Conclusion: A new self-gating method was proposed that allows cardiovascular magnetic resonance of arrhythmic patients, which is a common problem in clinical practice. Further, the proposed method enables self-gated imaging of the temporomandibular joint. **Magn Reson Med 000:000–000, 2015.** © **2015 Wiley Periodicals, Inc.**

Key words: self-gating; cine; cardiac; cardiovascular magnetic resonance; temporomandibular joint; arrhythmia

INTRODUCTION

Prospective electrocardiogram (ECG) triggered acquisition has become the de facto standard for cardiovascular magnetic resonance imaging. Despite the use of rapid, accelerated real-time cine imaging (1,2), ECG gated (3) or retrospective self-gated techniques for cine imaging (4–6) achieve better image quality in terms of signal-to-noise ratio (SNR) for a comparable temporal and spatial resolution provided that no additional artifacts occur due to wrong binning caused by irregular heart beats or patient movement.

Gating methods usually identify a reference (zero-phase) position (e.g., R wave) for each cycle. Under the assumption that all cycles show identical motion, a fully sampled k-space dataset is compiled from k-space data acquired during multiple motion cycles.

In case of e.g., cardiac arrhythmia the assumption of identical motion cycles is not valid, as the contraction of the myocardium is a complex, nonlinear movement, and cardiac motion phases show a highly nonlinear relation to the heart rate (7,8). Therefore, simple linear rescaling of the cardiac motion phases to the ECG signal will lead to wrong binning and artifacts or temporal blurring. In current practice, cycles deviating substantially from the mean interval are discarded. This leads to increased acquisition time and often degraded image quality. Furthermore, information about the arrhythmic motion is lost.

While real-time imaging was successfully used for cardiovascular imaging, in particular in case of arrhythmia, the clinical evaluation is still ongoing. More specifically, all real-time methods that achieve the necessary temporal resolution of 20–50 ms use temporal regularization or filtering and the impact on the effective temporal resolution/functional parameters is still under debate. For example, Voit et al. (1) reported a 10% lower ejection fraction for real-time imaging compared with breath-hold ECG gated imaging, which was confirmed by our preliminary results (9). In contrast, Aandal et al. (2) did not report any deviations in global functional parameters. A gating method capable of imaging arrhythmia might circumvent these challenges and will fit well into the existing clinical routine of gated acquisitions.

Similar to cardiac arrhythmia, self-gated imaging of active joint motion is prevented by the usually not perfectly reproducible motion cycles, e.g., for imaging of the moving temporomandibular joint (TMJ) (10,11).

In this work, we propose a self-gating method that uses a two-dimensional gating matrix without presuming identical motion cycles, but motion cycles that at least partially follow the same motion trajectory, possibly at a different pace.

METHODS

Image-Based Self-Gating

Larson et al. (5) suggested to reconstruct a preliminary image series m with low spatial and high temporal resolution using a sliding window reconstruction with window width w. The image series m is restricted to a region of interest containing the myocardial wall. The one-dimensional self-gating signal g is defined using the Pearson correlation ρ (12) of all images m_n to a selected template image m_t

$$g_n = \rho(m_t, m_n). \quad [1]$$

This technique performs well in comparison to other self gating methods (13,14) and was selected as reference

[1]Department of Internal Medicine II, University Hospital of Ulm, Germany.
[2]Sirona Dental Systems, Imaging Systems, Bensheim, Germany.
[3]Department of Oral and Maxillofacial Surgery, University of Ulm, Germany.
*Correspondence to: Stefan Wundrak; Dipl. Inf. Department of Internal Medicine II, University Hospital of Ulm, Germany. E-mail: stefan.wundrak@uni-ulm.de

Received 10 June 2015; revised 1 September 2015; accepted 1 September 2015
DOI 10.1002/mrm.26000
Published online 00 Month 2015 in Wiley Online Library (wileyonlinelibrary.com).

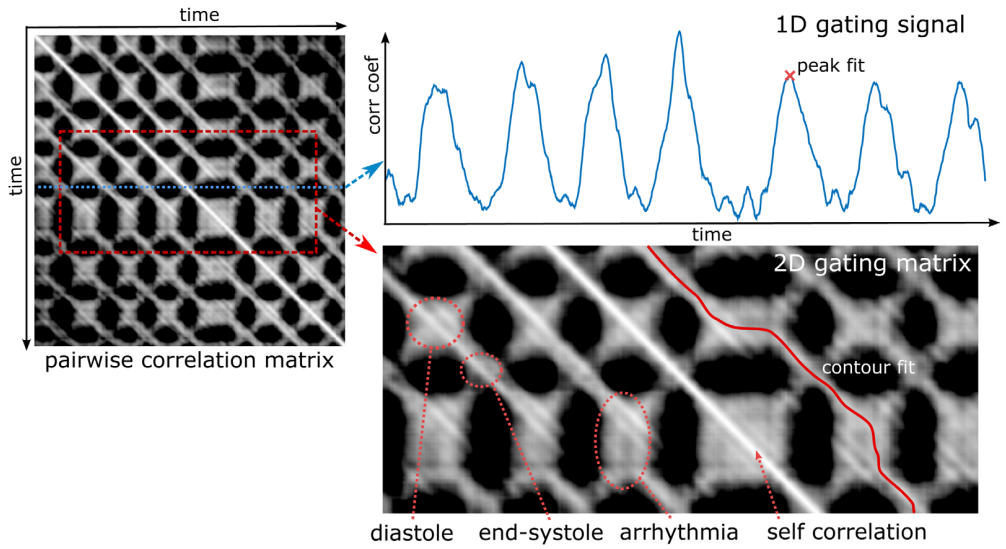

FIG. 1. Structure of the pair-wise correlation matrix D for an arrhythmic heart. Higher values indicate higher similarity of the template image (row) to the comparison image (column). The reference image is similar to images in the same position and same movement direction (lines parallel to the main diagonal) and in the same position and the opposite movement direction (lines orthogonal to the main diagonal). A row of the matrix equals the one-dimensional self-gating signal used in image-based self-gating (top). The peaks in the one-dimensional gating signal form curved lines in the two-dimensional gating matrix (bottom—red).

method for this work. The one-dimensional gating signal g is low-pass filtered using a temporal median filter with width σ. Peaks are detected to identify the zero-phase (trigger point) of each motion cycle. The k-space profiles are sorted into time frames based on the time interval to the neighboring peaks. The time frames are reconstructed frame-by-frame using gridding reconstruction. Cycles differing by more than $\Delta = 30\%$ in length from the mean cycle interval are rejected. The method is referenced as SG in the rest of this work.

Nonuniform Self-Gating

Overview

In case of nonreproducible motion cycles the SG method is not suitable, since k-space profiles of different motion phases will be sorted into the same bin. A nonuniform self-gating method (nuSG) with a weaker precondition is proposed, that presumes motion cycles that at least partially follow the same motion trajectory, possibly at a different pace. This motion model is expressed by curved line structures in a two-dimensional correlation matrix (see Fig. 1 and the following section). The suggested method comprises the following steps (see Fig. 2):

1. Acquire N golden angle radial k-space profiles
2. Reconstruct low spatial, high temporal resolution image series m
3. Restrict image series m to region of interest covering the moving anatomy of interest
4. Calculate pair-wise correlation matrix D for image series m
5. Fit active contours on line structures in D that indicate similar motion stages
6. Grow contours and detect gaps
7. Reconstruct cine images from k-space data selected by the active contours
8. Filter remaining streak artifacts

Contours in the Correlation Matrix

The $N \times N$ correlation matrix D is calculated using the pairwise Pearson correlation of all images in m, restricted to the region-of-interest region of interest.

$$D = (d_{r,c}); d_{r,c} = \rho(m_r, m_c). \quad [2]$$

Thus, each row r of D contains the one-dimensional gating signal from Eq. [1] using the template image m_r (Fig. 1). The two-dimensional gating matrix D for a cyclic moving object exhibits the rhombus structure shown in Figure 1. High correlation values indicate images in the same motion state as the reference image. The bright and straight main diagonal of the matrix result from the perfect similarity of each reference image to itself. If the object moved in identical cycles the matrix would exhibit perfectly straight lines parallel to the main diagonal. The nonuniform motion leads to curved lines that are only approximately parallel to the main diagonal. Lines approximately orthogonal to the main diagonal indicate images in the same motion state, but in the opposite motion direction of the reference image (e.g., *contraction* instead of *relaxation*).

Contour Fitting

If two motion cycles at least partially follow the same motion trajectory, possibly at a different pace, the correlation matrix exhibits a continuous and smooth line approximately parallel to the main diagonal. Therefore, smooth and continuous curves are fitted onto the line structures of D using active contour matching (15). The

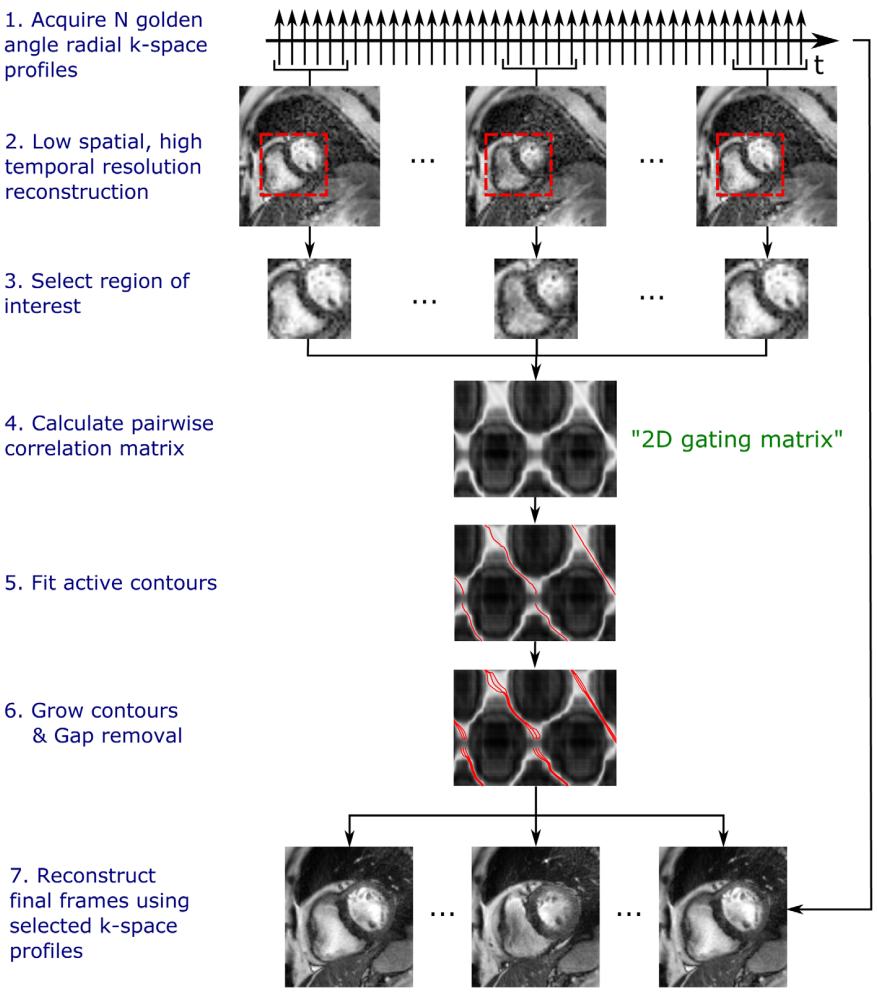

FIG. 2. Schematic overview of the proposed nuSG method.

one-dimensional parametric open active contour $v(r)$ specifies the column position for each row r of D.

$$E_{\text{cont}} = \sum_{r=1}^{N} E_{\text{int}}(v,r) + E_{\text{img}}(v,r) \qquad [3]$$

where the external energy term $E_{\text{img}}(v,r) = -d_{r,v(r)}$ forces the active contour toward the maxima of the correlation matrix D and the internal energy term E_{int} models the continuity and smoothness of the contour using the first- and second-order derivatives $E_{\text{int}}(v,r) = (\alpha|v'(r)|^2 + \beta|v''(r)|^2)/2$. The parameters α and β balance the tension and stiffness of the active contour. The active contour is relaxed using the Euler-Lagrange equation (see (16) for details).

Image Reconstruction

Each image x_r^* is reconstructed using all k-space profiles in a neighborhood w^* around the intersections $v_k(r)$ of all K contour lines with the row r of the correlation matrix D. In detail

$$x_r^* = \sum_{k=1}^{K} \sum_{n=v_k(r)-\frac{w^*}{2}}^{v_k(r)+\frac{w^*}{2}} G_n s_n \ , \qquad [4]$$

where G_n describes the linear gridding operator for the n^{th} radial profile of a golden ratio trajectory (17), and s_n the corresponding sampling values. Due to the golden ratio acquisition scheme, the window w^* can be chosen independently from the window width w that was used to generate the undersampled images of the distance matrix D. The neighborhood w^* may be set to a fixed value to directly define the temporal resolution, or may be adapted such that the reconstructed images x_r^* are sampled using $w^* = \pi Pm/(2C)$, where C is the actual number of cycles, m is the width of the acquisition matrix, and P the user defined sampling density. Remaining streak artifacts are filtered using a temporal total variation filter (18).

Grow Contours and Detect Gaps

If the motion path partially deviates from cycle to cycle, e.g., if in end-systole the myocardium did not fully contract, or the mandibula was not fully opened, or the TMJ exhibits "clicks," the line structures exhibit gaps (see Figs. 2 and 5). These gaps are detected by excluding values of the contour that are below a threshold γ relative to the mean of all correlation coefficients along the contour line.

If two frames have a similar ordering of radial profiles, the aliasing artifacts correlate and exhibit structures in the correlation matrix D parallel to the main diagonal. To avoid "locking" of the active contours during fitting to these superimposed structures in regions with broad correlation peaks (e.g., during a long resting phase), the neighborhood w^* is locally increased to cover δ percent of the correlation peak, where δ is a user defined parameter.

Feasibility Studies

The feasibility of the nuSG method was shown for the reconstruction of cardiac MRI data from patients with severe arrhythmia, and for assessment of the active motion of the TMJ. All studies were approved by the local ethics committee and written informed consent was obtained prior to the examination. All images were reconstructed using an in-house software package implemented with MATLAB (The MathWorks, MA).

For all scans a radial golden ratio profile ordering (17) was used, which proved to be beneficial for self-gating (13,19) by allowing a sliding window reconstruction with flexibility in the choice of the window width. Instead of the golden angle $\approx 111.246^\circ$ the smaller tiny golden angle $\approx 23.628^\circ$ was used (20) to avoid eddy current artifacts in combination with the balanced steady-state free precession sequence.

The parameters α and β for the active contours were optimized to fit the contour lines in all experiments as accurately as possible. The window width w was chosen to reach a trade-off between contrast and resolution in the gating matrix. The temporal median filter width was set to $\sigma = 2w$, which is a good trade-off between reduction of undersampling artifacts and temporal blurring. The grow threshold was set to $\delta = 95\%$ that prevented the locking to artifact correlation without influencing the temporal resolution during fast motion.

All datasets were additionally reconstructed using the real-time method *golden angle radial sparse parallel MRI* (GRASP) (21,22). The temporal regularization parameter λ was set to the smallest value that removed the radial undersampling artifacts in the region of interest.

Cardiac Experiment

Dynamic short axis time-resolved cardiac datasets were acquired from three patients (2 women, 1 man, aged 79–83 years) with known severe cardiac arrhythmia resulting in varying cardiac cycle length even during a short 6.3 s breathhold. Datasets were acquired on a Philips 1.5T Ingenia system (Philips Healthcare, Best, The Netherlands) with a 32-element cardiac coil. The acquisition parameters were: balanced steady-state free precession sequence, TR/TE = 2.6/1.3 ms, flip angle = 60°, resolution 1.7×1.7 mm^2, slice thickness 8 mm, acquisition matrix 212×212. The reconstruction parameters were 50 ms bin size for SG, $w = 23$, sampling window size $w^* = 20$, $\alpha = 0.001$, $\beta = 0.005$, and $\gamma = 66\%$ for nuSG. The reconstruction window of GRASP was also set to $w^* = 20$ profiles which equals a temporal resolution of 52 ms.

TMJ Experiment

Datasets from eight healthy volunteers (three women, five men, aged 21–51 years) were acquired. Further, seven patients with suspected TMJ derangement were scanned (six women, one man, aged 31–49 years). Sagittal images were acquired on a Philips 3T Achieva system (Philips Healthcare, Best, The Netherlands) using a 2×4 channel carotid coil (Chenguang Medical Technologies, Shanghai, China). The acquisition parameters were: in-phase balanced steady-state free precession, TE/TR = 2.3/4.6 ms, flip angle = 48°, pixel bandwidth of 949 Hz, spatial resolution of $0.75 \times 0.75 \times 5\,\text{mm}^3$, 256×256 pixel acquisition matrix, and a scan time of 60 s. The patients were instructed to continuously open and close the mouth within 8 s during the acquisition. The reconstruction parameters were 45 phases for SG, $w = 38$, $P = 75\%$, $\alpha = 0.001$, $\beta = 0.2$, and $\gamma = 66\%$ for nuSG. The window size of GRASP was set to w^* to achieve the same temporal resolution as nuSG.

Image Analysis

For each reconstructed image sequence, the image sharpness was calculated. For cardiac images, a profile was placed over the septal myocardial wall in the end-diastole frame as shown in Figure 3. For TMJ images the profile was placed over the condyle edge, in the center-frame between the open and the closed position. Edge sharpness was calculated as the mean intensity slope between the 20% and 80% signal level of the profile similar to (23). Significance of sharpness increase was assessed for TMJ using the one-sided Wilcoxon signed rank test. No significance tests were performed for cardiovascular magnetic resonance due to the small number of cases. A quantitative analysis of the left ventricular blood pool area was done using one short axis slice cine and standard software [Segment, Medviso, Lund, Sweden (24)].

RESULTS

Cardiac Experiment

Reconstructions were performed successfully in all cases. The number of rejected/detected cardiac cycles in SG was 2/5, 2/8, and 1/7, for the three patients, respectively.

A comparison between SG, nuSG, and GRASP reconstructions is provided in Figure 3 and as cardiac cines in the Supporting Information. The M-mode of SG clearly shows that the arrhythmic cycles are concealed, while for nuSG and GRASP all cycles are visible (asterisk). Visually, the images from SG have more residual streaking artifacts, especially in patient 1, and appear less sharp than the images from nuSG. The visual impression of increased wall sharpness in nuSG over SG is confirmed by quantitative evaluation (see Fig. 5), showing an increase of 80% on average for the three patients. In comparison to GRASP, nuSG also appears less noisy, as can be appreciated from the M-Mode plots, and sharpness is increased by 96% on average. The end-diastolic left ventricular blood pool area was on average 19.6 ± 2.9, 19.5 ± 1.4, $19.6 \pm 2.6\,\text{cm}^2$ for SG, nuSG,

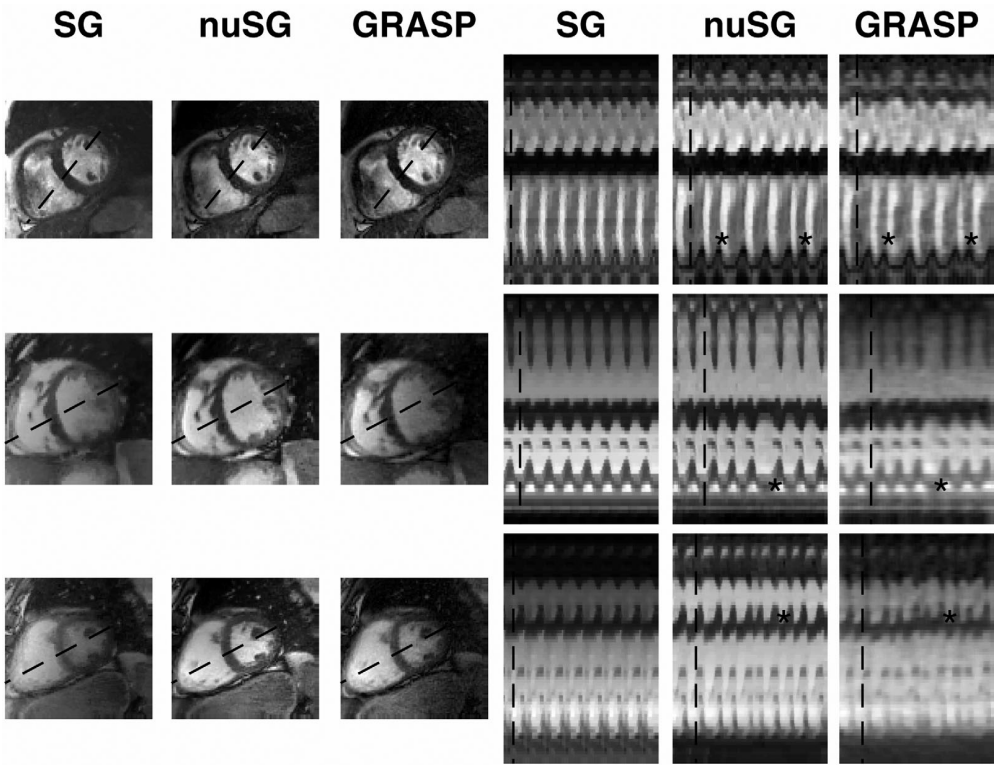

FIG. 3. Comparison of images (left columns) and M-modes (right columns) for the three reconstruction methods and for all arrhythmia patients (rows). The M-modes of the cardiac cine reconstructions (SG) (replicated for better visualization), indicates a single cyclic motion, while cardiac cycles of different length due to arrhythmia (asterisks) can be appreciated in the M-modes of nuSG and GRASP. Images from nuSG appear less noisy than from SG, as more k-space data was used for reconstruction, whereas in SG the cardiac cycles with arrhythmia had to be excluded from reconstruction. In GRASP only the k-space data of the current cardiac phase is used for reconstruction leading to increased noise, and due to temporal regularization to some temporal blurring. Cardiac cines for this figure are available as Supporting Information.

GRASP, respectively. The end-systolic area was on average 9.6 ± 3.1, 10.5 ± 1.4, $13.8 \pm 1.6\,\mathrm{cm}^2$, respectively.

TMJ Experiment

In comparison to SG, the proposed method resulted in improved image quality in all cases. Figure 4 shows four frames during the opening movement of the TMJ. Visual comparison of the two methods shows a clear improvement in image quality by nuSG for the moving condyle over SG and GRASP. The nuSG reconstruction provided sharp edges even during the phase of the fast condyle movement. In contrast, the SG reconstruction leads to strong blurring of the condyle. The M-mode plots show that the nuSG reconstruction is able to reproduce a higher temporal fidelity than SG and GRASP. Movies of the moving TMJ for volunteers and patients are available as Supporting Information.

Figure 5 summarizes the increase of image sharpness over the SG reconstructed images during the phase of condyle movement. The sharpness of the moving condyle edge was significantly increased by nuSG over SG for both groups ($P < 0.01$). The effective mean open/closing time was 4.2 ± 0.9 s for the volunteers and 3.9 ± 1.9 s for the patients. The temporal resolution based on the window width w^* was 180 ± 48 ms for the volunteers, and 176 ± 87 ms for the patients.

DISCUSSION

The poor results of the SG method show the limited feasibility of image-based self-gating methods in case of nonuniform motion. Even though only one self-gating variant was tested in this work, other variants like *center of mass kymogram* or *echo peak signal* (25) will likely lead to a similar result, as the underlying model of uniform motion cycles is not fulfilled.

In case of cardiac imaging, a rejection threshold is set to exclude arrhythmic cycles. Therefore, from the remaining uniform cycles, SG is usually still able to reconstruct cine images, however, with incomplete k-space data. The rejection threshold Δ, is a trade off between SNR and image sharpness. A low threshold excludes many cycles which leads to a low SNR or incomplete k-space. A high threshold keeps cycles that do not match which leads to image blurring and image artifacts. For example, patient 1 (Fig. 3) showed frequent extra-systoles and 40% of the cycles were rejected leading to low SNR and aliasing artifacts. Increasing the acquisition time was not an option due to breathhold limitations. In case of patient 3, the motion was even more irregular (fast and very irregular systoles) and the separation into valid and invalid cycles was not possible. In this case, SG is not able to reproduce any usable images (Fig. 3). In contrast, nuSG is able to use a larger

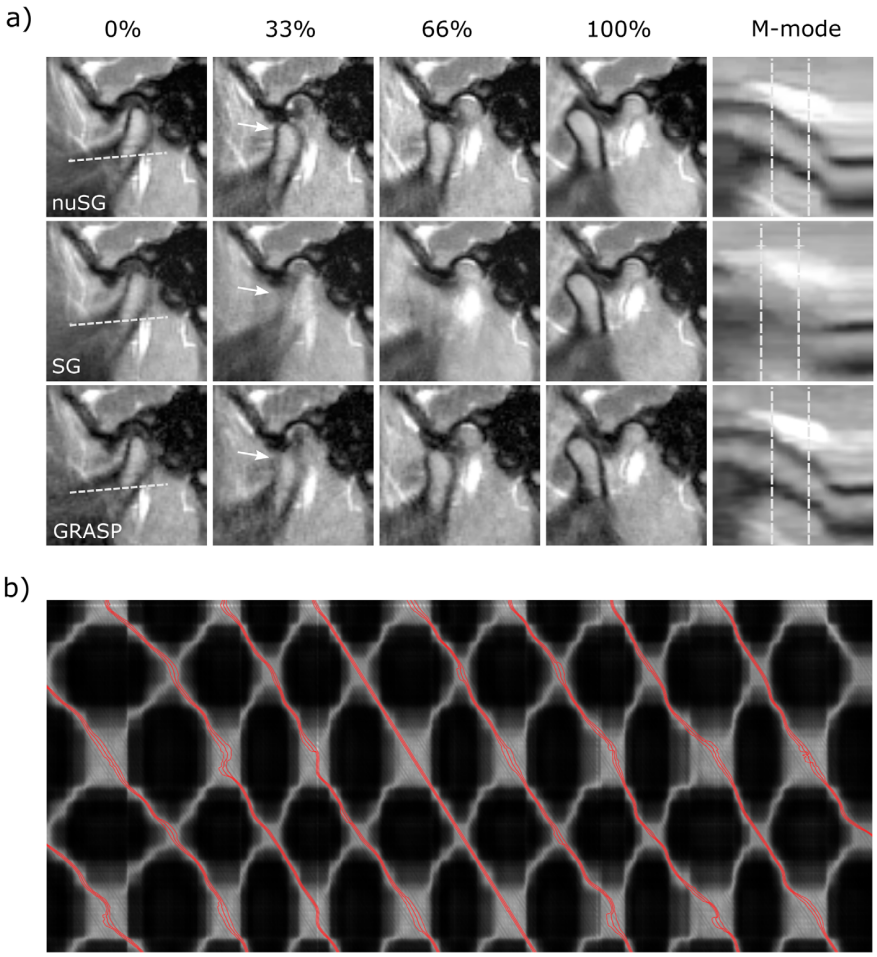

FIG. 4. **a**: Four equally spaced frames and M-mode plots of the opening TMJ reconstructed with nuSG, SG, and GRASP. The volunteer was opening the mouth within 3.4 s. The SG and iterative GRASP reconstruction show temporal blurring of the condyle (arrow). **b**: two-dimensional gating matrix of the same volunteer with active contours (red).

fraction of the acquired data, which leads to less aliasing and higher image sharpness.

As in the cine images reconstructed with GRASP, nuSG allows full appreciation of the arrhythmic heartbeats and shows all distinct cardiac cycles. In contrast, the SG method might misleadingly suggest a rhythmic heart. Even though real-time cine methods allow the acquisition without breath-hold, breath-hold acquisitions are day-to-day clinical routine and are justified for our method by the improved image quality of nuSG over GRASP.

The average end-diastolic volume was similar across the three methods, the end-systolic volume was overestimated by GRASP, which may be due to temporal regularization and leads to an underestimation of ejection fraction. Even though the number of cases were too small for any significance calculation, these results are in line with (9) and (1). In our experience, the proposed nuSG method is significantly less complex to implement, needs less computing power and is easier to parameterize than iterative real-time reconstruction methods.

In case of TMJ imaging, the proposed method allows the measurement of the TMJ opening/closing movement at a pace of about 8 s at $0.75 \times 0.75 \times 5\,\mathrm{mm}^3$ with little or no temporal blurring. Compared with previous work (26) where the same spatial resolution was used, this work shows about the same acquisition length and the same image quality, but a 9-fold increase in the nominal temporal resolution ($\approx$ 180 ms instead of 1655 ms). The effective temporal resolution may be lower, due to inaccuracy of the contour fitting. It still has to be evaluated how the method performs in case of sudden motion, like TMJ clicks (27), or in case of mastication under load (11).

Adaptive averaging methods (28,29) are related to image-based self-gating, in a sense that an image similarity function is used to identify subsets of images in an image sequence to be averaged. However, in adaptive

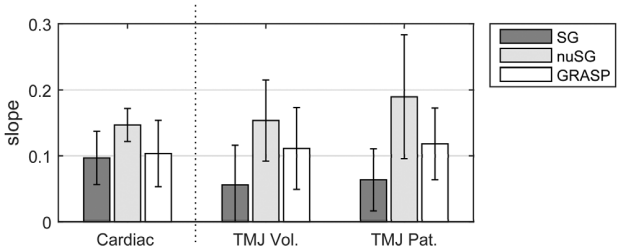

FIG. 5. Sharpness measured for three cardiac patients (on myocard wall), eight TMJ volunteers and seven TMJ patients (on condyle edge). TMJ sharpness for nuSG was significantly increased ($P < 0.01$) over SG; for cardiovascular magnetic resonance no significance was calculated due to the limited number of patients.

averaging no model of cyclic motion is used, and fully sampled images instead of partially sampled k-space views are combined.

In conclusion, a new self-gating method was proposed that allows cardiovascular magnetic resonance imaging of arrhythmic patients which is a common problem in clinical practice. Further, the proposed method enables SG imaging of the moving TMJ. More applications may be possible, e.g., SG imaging of the knee or wrist joint, or imaging of the soft palate.

ACKNOWLEDGMENTS

The authors thank Dr. Uta Denzel and Dr. Andreas Niedermayr for patient guidance. Stefan Wundrak and Jan Paul contributed equally to this work.

REFERENCES

1. Voit D, Zhang S, Unterberg-Buchwald C, Sohns JM, Lotz J, Frahm J. Real-time cardiovascular magnetic resonance at 1.5 T using balanced SSFP and 40 ms resolution. J Cardiovasc Magn Reson 2013;15:79.
2. Aandal G, Nadig V, Yeh V, Rajiah P, Jenkins T, Sattar A, Griswold M, Gulani V, Gilkeson RC, Seiberlich N. Evaluation of left ventricular ejection fraction using through-time radial GRAPPA. J Cardiovasc Magn Reson 2014;16:1–13.
3. Lanzer P, Barta C, Botvinick EH, Wiesendanger HUD, Higgins CB. ECG-synchronized cardiac MR imaging: method and evaluation. Radiology 1985;155:681–686.
4. Spraggins TA. Wireless retrospective gating: application to cine cardiac imaging. Magn Reson Imaging 1990;8:675–681.
5. Larson AC, White RD, Laub G, Mcveigh ER, Simonetti OP. Self-gated cardiac cine MRI. Magn Reson Med 2004;51:93–102.
6. Kellman P, Chefd'hotel C, Lorenz CH, Mancini C, Arai AE, McVeigh ER. High spatial and temporal resolution cardiac cine MRI from retrospective reconstruction of data acquired in real time using motion correction and resorting. Magn Reson Med 2009;62:1557–1564.
7. Krogh-Madsen T, Christin DJ. Nonlinear dynamics in cardiology. Ann Rev Biomed Eng 2012;14:179–203.
8. Webber CL. Nonlinear cardiac dynamics. In: Roka A, editor. Current issues and recent advances in pacemaker therapy. Rijeka: Intech; 2012. pp 233–246.
9. Wundrak S, Paul J, Ulrici J, Hell E, Rasche V. Does temporal regularization lead to systematic underestimation of ejection fraction? In: Proc Int Soc Magn Reson Med, Vol. 15. p 4380, Proceedings of the 22th Annual Meeting of ISMRM, Milano, 2014.
10. Burnett KR, Davis CL, Read J. Dynamic display of the temporomandibular joint meniscus by using 'fast-scan' mr imaging. Am J Roentgenol 1987;149:959–962.
11. Hopfgartner AJ, Tymofiyeva O, Ehses P, Rottner K, Boldt J, Richter EJ, Jakob PM. Dynamic MRI of the TMJ under physical load. Dentomaxillofac Radiol 2013;42.
12. Edwards AL. An introduction to linear regression and correlation. San Francisco, CA: W. H. Freeman, pp. 33–46, 1976.
13. Paul J, Divkovic E, Wundrak S, Bernhardt P, Rottbauer W, Neumann H, Rasche V. High-resolution respiratory self-gated golden angle cardiac MRI: comparison of self-gating methods in combination with k-t SPARSE SENSE. Magn Reson Med 2015;73:292–298.
14. Tibiletti M, Paul J, Bianchi A, Wundrak S, Rottbauer W, Stiller D, Rasche V, Multistage Three-Dimensional UTE Lung imaging by image-based self-gating. Magn Reson Med, doi:10.1002/mrm.25673.
15. Kass M, Witkin A, Terzopoulos D. Snakes: active contour models. Int J Comput Vis 1988;1:321–331.
16. Ivins J, Porril J. Everything you always wanted to know about Snakes (but were afraid to ask). Technical Report July 1993. Artificial Intelligence Vision Research Unit, University of Sheffield 2000.
17. Winkelmann S, Schaeffter T, Koehler T, Eggers H, Doessel O. An optimal radial profile order based on the golden ratio for time-resolved MRI. IEEE Trans Med Imaging 2007;26:68–76.
18. Rudin LI, Osher S, Fatemi E. Nonlinear total variation based noise removal algorithms. Phys D 1992;60:259–268.
19. Buerger C, Clough RE, King AP, Schaeffter T, Prieto C. Nonrigid motion modeling of the liver from 3-D undersampled self-gated golden-radial phase encoded MRI. IEEE Trans Med Imaging 2012;31:805–815.
20. Wundrak S, Paul J, Ulrici J, Hell E, Rasche VA. Small surrogate for the golden angle in time-resolved radial MRI based on generalized fibonacci sequences. IEEE Trans Med Imaging 2014;34.
21. Feng L, Grimm R, Tobias Block K, Chandarana H, Kim S, Xu J, Axel L, Sodickson DK, Otazo R. Golden-angle radial sparse parallel MRI: combination of compressed sensing, parallel imaging, and golden-angle radial sampling for fast and flexible dynamic volumetric MRI. Magn Reson Med 2013;72:707–717.
22. Wundrak S, Paul J, Ulrici J, Hell E, Geibel MA, Bernhardt P, Rottbauer W, Rasche V. Golden ratio sparse MRI using tiny golden angles. Magn Reson Med, doi:10.1002/mrm.25831.
23. Larson AC, Kellman P, Arai A, Hirsch GA, Mcveigh E, Li D, Simonetti OP. Preliminary investigation of respiratory self-gating for free- breathing segmented cine MRI. Magn Reson Med 2005;53:159–168.
24. Heiberg E, Sjögren J, Ugander M, Carlsson M, Engblom H, Arheden HK. Design and validation of Segment—freely available software for cardiovascular image analysis. BMC Med Imaging 2010;10:1–13.
25. Hardy CJ, Zhao L, Zong X, Saranathan M, Yucel EK. Coronary MR angiography: respiratory motion correction with BACSPIN. J Magn Reson Imaging 2003;17:170–176.
26. Zhang S, Gersdorff N, Frahm J. Real-time magnetic resonance imaging of temporomandibular joint dynamics. Open Med Imaging J 2011;5:1–7.
27. Scrivani SJ, Keith DA, Kaban LB. Temporomandibular disorders. N Engl J Med 2008;359:2693–2705.
28. Hardy CJ, Saranathan M, Zhu Y, Darrow RD. Coronary angiography by real-time MRI with adaptive averaging. Magn Reson Med 2000;44:940–946.
29. Scott AD, Boubertakh R, Birch MJ, Miquel ME. Adaptive averaging applied to dynamic imaging of the soft palate. Magn Reson Med 2013;70:865–874.

SUPPORTING INFORMATION

Additional Supporting Information may be found in the online version of this article.

Supporting Video 1: This supporting video shows the comparison of SG, nuSG, and GRASP for cardiac arrhythmia patient 1 from Figure 3.

Supporting Video 2: This supporting video shows the comparison of SG, nuSG, and GRASP for cardiac arrhythmia patient 2 from Figure 3.

Supporting Video 3: This supporting video shows the comparison of SG, nuSG, and GRASP for cardiac arrhythmia patient 3 from Figure 3.

Supporting Video S4: This supporting video shows the comparison of SG and nuSG for the TMJ reconstruction shown in Figure 4.

Supporting Videos S5 to S7: These supporting videos show the comparison of SG and nuSG for three TMJ patients. The first patient exhibits an anterior displacement of the disc without reposition at a flattened articular tubercle with an unphysiological and limited movement pattern. The second patient exhibits thinned structures between the condyle and the fossa articularis without recognizable physiological structure of the discus and a limited movement sequence. The third case exhibits an anatomical inconspicuous discus condyle relation. The movement terminates at the zenith of the articular tubercle.

Chapter 7

Summarized Results

In the first part, this work generalized the golden angle and introduced the series of tiny golden angles ($\psi_N = \frac{\pi}{\tau+N-1}$)[1], whose first two members are the well known golden angle $\psi_1 = 111.246...^\circ$ and the small golden angle $\psi_2 = 68.753...^\circ$. The series continues with decreasing angles (49.750...°, 38.977...°, 32.039...°, 27.198...°, and 23.628...° ...). It was shown, that similar to the golden angle, the tiny golden angles guarantee a near uniform distribution for an arbitrary number of radial profiles. Using numerical simulations it was proven that the proposed tiny golden angles guarantee a similar optimal sampling efficiency if at least a minimum number of $2N + 1$ radial profiles are used. Experiments showed that the smaller azimuthal angle increments of the tiny golden angles significantly reduce the eddy current induced artifacts (Figure 14). This was demonstrated for phantom, cardiac and TMJ imaging. In all cases an angle increment between ψ_5 and ψ_7 seemed sufficient to suppress the eddy current induced image artifacts to an acceptable level.

In the second part of this work it was shown that the newly introduced tiny golden angles are well suited for sparse MRI imaging. The incoherence analysis showed that tiny golden angle trajectories exhibit comparable incoherence to the golden angle if the window width is $P > 2N$. Simulations (without the consideration of eddy current effects)

[1] where τ is the golden ratio $\frac{1+\sqrt{5}}{2}$

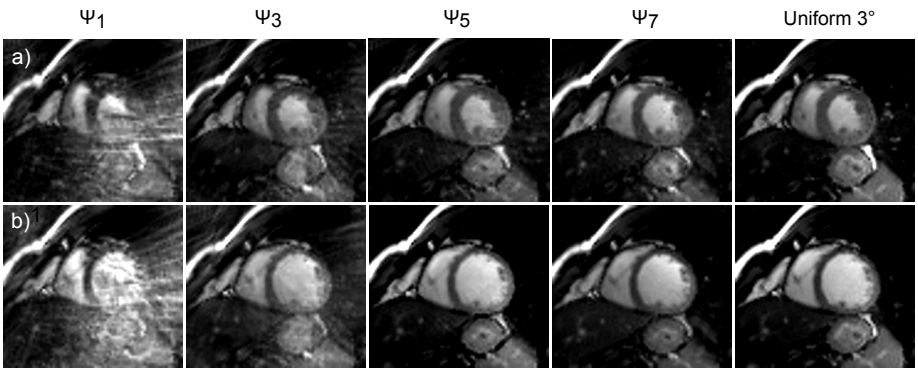

Figure 14: a) The systole reconstructed with 60 radial profiles. The image acquired with the golden angle azimuthal increment ψ_1 shows strong image artifacts. Image artifacts are reduced if the angle gets smaller. b) The enddiastolic phase was reconstructed with 120 radial profiles (due to the longer resting phase).

using a numerical phantom and the proposed tyGRASP reconstruction confirmed that the tiny golden angles and the golden angle lead to comparable image quality. For in-vivo cardiac imaging at a temporal resolution of $53ms$ using the b-SFFP sequence, eddy current related image artifacts were clearly reduced for tyGRASP using ψ_7 compared to GRASP. These effects could be shown on two different MRI system (1.5 T and 3 T) and were quantified showing a significant reduction of the coefficient of variation. The same results could be shown for in-vivo dynamic imaging of the TMJ. In particular, the combination of tiny golden angle imaging and b-SFFP allowed to depict the moving articular disc at high temporal ($175ms$) and spatial ($0.75 \times 0.75 \times 5mm^3$) resolution without eddy current induced artifacts (Figure 15).

In the third part of this work a new self-gating approach for nonuniform motion was introduced. The proposed method (nuSG) replaces the 1D gating signal of conventional self-gating with a 2D gating matrix to allow motion cycles that at least partially follow the same motion trajectory, possibly in a different pace. The proposed method was able to depict patients with severe cardiac arrhythmia despite the non-linear relation between heart rate and cardiac motion phases. Further nuSG was able to depict the nonuniform motion of the moving TMJ. NuSG resulted in superior image quality compared to con-

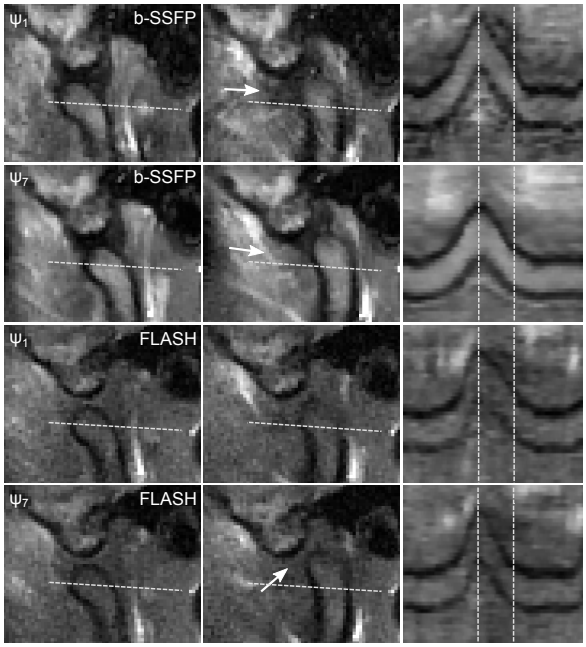

Figure 15: Moving temporomandibular joint reconstructed using tyGRASP with a golden angle and a tiny golden angle trajectory: in closed condyle position (left), during condyle movement (middle), and M-mode plots (right). The golden angle trajectory leads to strong image artifacts (top row, arrow) that do not occur with the tiny golden angle ψ_7 (second row). The FLASH sequence does not show artifacts at the cost of signal-to-noise ratio and the visibility of the discus articularis (bottom row, arrow). Abbreviations: fast low angle shot (FLASH), balanced steady state free precession (b-SSFP).

ventional self-gating (Figure 16). The feasibility study for three patients with severe arrhythmia showed significantly improved image sharpness of the myocardial wall. In direct comparison to tyGRASP the average end-diastolic volume was similar to nuSG. However, the end-systolic volume was overestimated by tyGRASP, which may be due to temporal regularization and leads to an underestimation of ejection fraction. These results are in line with the observations of [139], [151], and [30] regarding temporal regularization. Improvements in image quality were also shown for the moving condyle edge during TMJ imaging. Compared to real-time cine imaging and conventional self-gating, nuSG showed significantly improved image sharpness ($p < 0.01$) of the moving condyle edge.

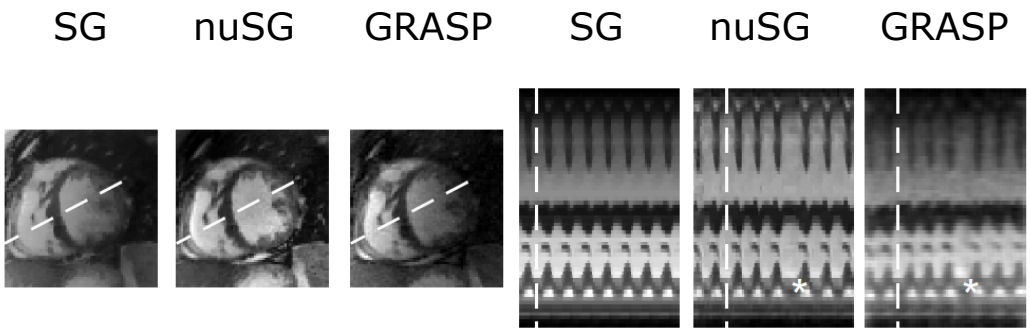

Figure 16: Comparison of the resulting images (left columns) and M-modes (right columns) for a patient with severe arrhythmia. The M-modes of the conventional self-gated reconstructions (SG) (replicated for better visualization), indicate a single cyclic motion, while cardiac cycles of different length due to arrhythmia (asterisks) can be appreciated in the M-modes of nuSG and GRASP. The GRASP reconstruction shows increased noise, and due to the temporal regularization some temporal blurring. Abbreviations: self-gated (SG), nonuniform self-gated (nuSG), golden angle radial sparse parallel MRI (GRASP).

Chapter 8

Discussion and Conclusion

In this work a modified golden ratio acquisition order using smaller angular increments has been introduced for radial MRI. It has been shown that the proposed order yields similar properties as the well-known golden angle acquisition order [3] regarding the uniformity for an arbitrary number of radial profiles, but shows improved performance for b-SSFP sequences with respect to eddy-current related artifacts.

Interestingly, similar results regarding the uniformity of a radial distribution using some of the tiny golden angles were reported previously in the field of theoretical biology, explaining the distribution uniformity of leaves [86], and independently by King et al. for a shadow cast model [67]. However, in the presented form these angles were previously not known, in particular for MR imaging.

The image artifacts caused by the combination of golden angle ordering and b-SSFP sequences were verified on two Philips MRI systems for 1.5 T and 3 T, and were recently confirmed for one 1.5 T Siemens MRI system by [59]. While these artifacts were previously known from step-wise changing phase-encoding gradients [14] and interleaved imaging [87], no artifacts were found in the work of Winkelmann et al. [143]. Further, Speier et al. [126] showed less severe artifacts also for a spoiled gradient echo sequences, that could not be observed in this work. However, it is known that eddy-current effects are highly dependent on the MRI system and the actual gradient switching scheme, are

hard to predict, and vary from system to system.

The tiny golden angles enable the combination of b-SSFP sequences with golden ratio profile ordering. In case of TMJ imaging, this result is highly relevant, since the T1/T2 contrast of the b-SSFP sequence is essential for imaging the discus articularis, which in most cases is the main interest of the physician [31]. No fast sequence with a T2 dependent contrast is known that could replace the b-SSFP in this case.

While there was much previous work on sparse MRI using the principles of compressed sensing in combination with radial golden angle trajectories [33, 26, 46], the GRASP method was predominantly used for dynamic contrast enhanced MRI [65, 46, 43] and no work using GRASP with b-SSFP was published so far. This is likely due to the eddy current induce image artifacts described in this work. Note, that in case of a 3D stack-of-stars acquisition this problem may be circumvented by sequentially acquiring a profile for each stack before advancing to the angular position, which basically equals the golden angle grouping technique describe by [87].

Despite the recent progress in real-time methods, including the tyGRASP method presented in this work, ECG gated imaging is still considered the gold standard in clinical practice for cardiac imaging and is used in day-to-day clinical practice. In general, breath-hold ECG gated imaging or self-gating will achieve better image quality in terms of SNR at comparable temporal & spatial resolution than real-time imaging, provided that no additional artifacts occur due to wrong binning caused by irregular heart beats.

For example, to avoid compromises in temporal and spatial resolution, decent real-time methods employ temporal regularization or filtering to achieve a nominal temporal resolution of 20 - 50ms. The impact on the effective temporal resolution and the functional parameters is still under debate. For instance, Voit et al. [139] reported a 10% lower ejection fraction for real-time imaging compared to breath-hold ECG gated imaging, which was confirmed by preliminary results in [151] and further discussed in [30].

The strongest advantages of real-time cardiac imaging over gated imaging are the ac-

quisition during free-breathing, and the inherent robustness to arrhythmia. While work has been done towards self-gated free-breathing acquisitions using additional self-gating of the respiratory motion and motion compensation [73], the latter problem has not yet been approached. In this work, the self-gated acquisition of severe cardiac arrhythmia was shown for the first time using the proposed nuSG method.

As in the cine images reconstructed with tyGRASP, nuSG allows full appreciation of the arrhythmic heartbeats and shows all distinct cardiac cycles. In contrast, the conventional self-gating methods will misleadingly suggest a rhythmic heart with identical motion cycles. Even though real-time cine methods have the advantage of free-breathing acquisitions, breath hold acquisitions are day-to-day clinical routine and are justified for nuSG by the improved image quality in comparison to tyGRASP.

Further, to our experience, the proposed nuSG method is significantly less complex to implement than advanced real-time methods, needs less computing power and is easier to parameterize than iterative real-time reconstruction methods.

In case of TMJ imaging, the proposed nuSG method allows the measurement of the TMJ opening / closing movement at a pace of about 8 seconds at $0.75 \times 0.75 \times 5mm^3$ with little or no temporal blurring. Compared to previous work (28) where the same spatial resolution was used, this work shows about the same acquisition length and the same image quality, but a 9-fold increase in the nominal temporal resolution (180 ms instead of 1655 ms). The effective temporal resolution may be lower, due to inaccuracy of the contour fitting.

Future research could be directed to combine the two proposed methods, e.g. by using tyGRASP reconstruction for the reconstruction of the resorted profiles from nuSG. Alternatively one could separate the cardiac motion from the breathing motion using nuSG and exploit the increased sparsity along both dynamic dimensions, similar to the XG-GRASP method recently proposed by Feng et al. [44].

In conclusion, this thesis proposed solutions to two severe problems in time-resolved imaging of nonuniform motion: a golden angle real-time cine method that does not

affect the steady state of the b-SSFP sequence, and a retrospectively nonuniform gating method that works with the nonuniform motion of severe cardiac arrhythmia and the moving TMJ.

Bibliography

[1] Abolmaali, N. D., Schmitt, J., Schwarz, W., Toll, D. E., Hinterwimmer, S., and Vogl, T. J. Visualization of the Articular Disk of the Temporomandibular Joint in Near-Real-Time MRI: Feasibility Study. *European Radiology* 14: 1889–94, 2004.

[2] Adcock, B., Hansen, A. C., Poon, C., and Roman, B. Breaking the coherence barrier: A new theory for compressed sensing. *preprint*: arXiv:1302.0561v4, 2014.

[3] Adluru, G., McGann, C., Speier, P., Kholmovski, E. G., Shaaban, A., and Dibella, E. V. R. Acquisition and Reconstruction of Undersampled Radial Data for Myocardial Perfusion Magnetic Resonance Imaging. *Journal of Magnetic Resonance Imaging* 29: 466–473, 2009.

[4] Allison, M. J., Ramani, S., and Fessler, J. A. Accelerated Regularized Estimation of MR Coil Sensitivities Using Augmented Lagrangian Methods. *IEEE Transactions on Medical Imaging* 32: 556–564, 2012.

[5] Azuma, T., Ito, J., Kutsuki, M., and Nakai, R. Analysis of the Mandibular Movement by Simultaneous Multisection Continuous Ultrafast MRI. *Magnetic Resonance Imaging* 27: 423–433, 2009.

[6] Beatty, P. J. and Brau, A. C. Understanding the GRAPPA Paradox. *Proceedings of the 14th Annual Meeting of ISMRM*. Vol. 14. Seattle, Washington, 2006: 2467.

[7] Beatty, P. J. Fast Image Reconstruction from Non-Cartesian Data. *Proc. Intl. Soc. Mag. Res. Med.* Honolulu, 2009: 1701.

[8] Beatty, P. J., Nishimura, D. G., and Pauly, J. M. Rapid Gridding Reconstruction with a Minimal Oversampling Ratio. *IEEE Transactions on Medical Imaging* 24: 799–808, 2005.

[9] Beck, A. and Teboulle, M. A Fast Iterative Shrinkage-Thresholding Algorithm for Linear Inverse Problems. *SIAM Journal on Imaging Sciences* 2: 183–202, 2009.

[10] Beck, A. and Teboulle, M. Fast Gradient-Based Algorithms for Constrained Total Variation Image Denoising and Deblurring Problems. *IEEE Transactions on Image Processing* 18: 2419–2434, 2009.

[11] Beer, A., Kolk, A., Neff, A., Hof, N., Treumann, T., and Rummeny, E. Cine-MRT des Kiefergelenks im Vergleich zur Konventionellen MRT und Achsiographie. *RoeFo - Fortschritte auf dem Gebiete der Roentgenstrahlen und der Bildgebenden Verfahren* 176: 506–512, 2004.

[12] Behr, M., Held, P., Leibrock, A., Fellner, C., and Handel, G. Diagnostic Potential of Pseudo-Dynamic MRI (CINE mode) for Evaluation of Internal Derangement of the TMJ. *European Journal of Radiology* 23: 212–215, 1996.

[13] Bernstein, M. A., King, K. F., and Zhou, X. J. *Handbook of MRI Pulse Sequences.* Elsevier Academic Press, 2004.

[14] Bieri, O., Markl, M., and Scheffler, K. Analysis and Compensation of Eddy Currents in Balanced SSFP. *Magnetic Resonance in Medicine* 54: 129–137, 2005.

[15] Bieri, O. and Scheffler, K. Fundamentals of Balanced Steady State Free Precession MRI. *Journal of Magnetic Resonance Imaging* 11: 2–11, 2013.

[16] Börnert, P., Schomberg, H., Aldefeld, B., and Groen, J. Improvements in Spiral MR Imaging. *Magnetic Resonance Materials in Physics, Biology and Medicine* 9: 29–41, 1999.

[17] Boutin, R. D., Buonocore, M. H., Immerman, I., Ashwell, Z., Sonico, G. J., Szabo, R. M., and Chaudhari, A. J. Real-Time Magnetic Resonance Imaging (MRI) during Active Wrist Motion - Initial Observations. *PloS ONE* 8: doi:10.1371/journal.pone.0084004, 2013.

[18] Brown, R. W., Cheng, Y.-C. N., Haacke, E. M., Thompson, M. R., and Venkatesan, R. *Magnetic Resonance Imaging: Physical Principles and Sequence Design.* Chichester, UK: 2nd Edition, John Wiley & Sons, 2014.

[19] Brummer, M. E., Moratal-Pérez, D., Hong, C.-Y., Pettigrew, R. I., Millet-Roig, J., and Dixon, W. T. Noquist: Reduced Field-of-View Imaging by Direct Fourier Inversion. *Magnetic Resonance in Medicine* 51: 331–342, 2004.

[20] Burnett, K. R., Davis, C. L., and Read, J. Dynamic Display of the Temporomandibular Joint Meniscus by Using 'Fast-Scan' MR Imaging. *American Journal of Roentgenology* 149: 959–962, 1987.

[21] Candès, E. and Romberg, J. l1-MAGIC: Recovery of Sparse Signals via Convex Programming: URL http://users.ece.gatech.edu/ ˜justin/l1magic/#, 2005.

[22] Candès, E. and Romberg, J. Practical Signal Recovery from Random Projections. *Proceedings of SPIE*. 2005: 5674.

[23] Candes, E., Romberg, J., and Tao, T. Robust Uncertainty Principles : Exact Signal Reconstruction from Highly Incomplete Frequency Information. *IEEE Transactions on Information Theory* 52: 489–509, 2005.

[24] Candes, E., Romberg, J., and Tao, T. Stable Signal Recovery from Incomplete and Inaccurate Measurements. *Communications on Pure and Applied Mathematics* 59: 1207–1223, 2006.

[25] Candes, E. and Tao, T. Decoding by Linear Programming. *IEEE Transactions on Information Theory* 51: 4203–4215, 2005.

[26] Chan, R. W., Ramsay, E. A., Cheung, E. Y., and Plewes, D. B. The Influence of Radial Undersampling Schemes on Compressed Sensing Reconstruction in Breast MRI. *Magnetic Resonance in Medicine* 67: 363–377, 2012.

[27] Chen, S. S., Donoho, D. L., and Saunders, M. A. Atomic Decomposition by Basis Pursuit. *SIAM Review* 43: 129–159, 2001.

[28] Chen, Y.-J., Gallo, L. M., Meier, D., and Palla, S. Dynamic Magnetic Resonance Imaging Technique for the Study of the Temporomandibular Joint. *Journal of Orofacial Pain* 14: 65–73, 2000.

[29] Chung, C. B., Du, J., Bae, W., Statum, S., Znamirowski, R., and Takahashi, A. Ultrashort TE (UTE) Imaging of the Temporomandibular Joint (TMJ) at 3T. *Proceedings of the 16th Annual Meeting of ISMRM*. Toronto, 2008: 738.

[30] Contijoch, F., Witschey, W. R. T., Rogers, K., Rears, H., Hansen, M., Yushkevich, P., Gorman, J., Gorman, R. C., and Han, Y. User-Initialized Active Contour Segmentation and Golden-Angle Real-Time Cardiovascular Magnetic Resonance Enable Accurate Assessment of LV Function in Patients with Sinus Rhythm and Arrhythmias. *Journal of Cardiovascular Magnetic Resonance* 17: doi:10.1186/s12968–015–0146–9, 2015.

[31] Conway, F., Hayes, C. W., and Campbell, R. L. Dynamic Magnetic Resonance Imaging of the Temporomandibular Joint Using FLASH Sequences. *Journal of Oral Maxillofacial Surgery* 46: 930–937, 1988.

[32] De Mot, B., Casselman, J., and DeBoever, J. Pseudodynamic Magnetic Resonance Imaging in the Diagnosis of Temporomandibular Joint Dysfunction. *The Journal of Prosthetic Dentistry* 72: 309–313, 1994.

[33] Doneva, M. Advances in Compressed Sensing for Magnetic Resonance Imaging. PhD thesis. Universität zu Lübeck, 2011.

[34] Doneva, M., Eggers, H., Rahmer, J., Börnert, P., and Mertins, A. Highly Undersampled 3D Golden Ratio Radial Imaging with Iterative Reconstruction. *Proceedings of the 16th Annual Meeting of ISMRM*. Vol. 16. Toronto, 2008: 336.

[35] Donoho, D. L. Compressed Sensing. *IEEE Transactions on Information Theory* 52: 1289–1306, 2006.

[36] Donoho, D. L. For Most Large Underdetermined Systems of Equations the Minimal l1-Norm Near-Solution Approximates the Sparsest Near-Solution. *Communications on Pure and Applied Mathematics* 59: 907–934, 2006.

[37] Donoho, D. L. and Huo, X. Uncertainty Principles and Ideal Atomic Decomposition. *IEEE Transactions on Information Theory* 47: 2845–2862, 2001.

[38] Dössel, O. *Bildegebende Verfahren in der Medizin*. Berlin: Springer, 2000.

[39] Eberhard, D., Bantleon, H.-P., and Steger, W. Functional Magnetic Resonance Imaging of Temporomandibular Joint Disorders. *European Journal of Orthodontics* 22: 489–497, 2000.

[40] Edwards, A. L. *An Introduction to Linear Regression and Correlation*. New York: W.H.Freeman & Co Ltd, 1976: pp. 33–46.

[41] Ehses, P., Seiberlich, N., Ma, D., Breuer, F. a., Jakob, P. M., Griswold, M. a., and Gulani, V. IR TrueFISP with a Golden-Ratio-based Radial Readout: Fast Quantification of T1, T2, and Proton Density. *Magnetic Resonance in Medicine* 69: 71–81, 2013.

[42] Elster, A. D. and Burdette, J. H. *Questions & Answers in Magnetic Resonancen Imaging*. Mosby, 2nd edition, 2001.

[43] Espagnet, M. C. R., Bangiyev, X. L., Haber, M., Block, K. T., Babb, J., Ruggiero, V., Boada, F., Gonen, O., and Fatterpekar, G. M. High-Resolution DCE-MRI of the Pituitary Gland Using Radial k -Space Acquisition with Compressed Sensing Reconstruction. *American Journal of Neuroradiology*: doi:10.3174/ajnr.A4324, 2015.

[44] Feng, L., Axel, L., Chandarana, H., Block, K. T., Sodickson, D. K., and Otazo, R. XD-GRASP: Golden-angle radial MRI with reconstruction of extra motion-state dimensions using compressed sensing. *Magnetic Resonance in Medicine*: doi:10.1002/mrm.25665, 2015.

[45] Feng, L., Chandarana, H., Xu, J., Block, K. T., Sodickson, D. K., and Otazo, R. K-t Radial SPARSE-SENSE: Combination of Compressed Sensing and Parallel Imaging with Golden Angle Radial Sampling for Highly Accelerated Volumetric Dynamic MRI. *Proc. Intl. Soc. Mag. Reson. Med.* 2011: 1117.

[46] Feng, L., Grimm, R., Tobias Block, K., Chandarana, H., Kim, S., Xu, J., Axel, L., Sodickson, D. K., and Otazo, R. Golden-angle radial sparse parallel MRI: Combination of compressed sensing, parallel imaging, and golden-angle radial sampling for fast and flexible dynamic volumetric MRI. *Magnetic Resonance in Medicine* 72: 707–717, 2013.

[47] Feng, L., Srichai, M. B., Lim, R. P., Harrison, A., King, W., Adluru, G., Dibella, E. V. R., Sodickson, D. K., Otazo, R., and Kim, D. Highly Accelerated Real-Time Cardiac Cine MRI using k-t SPARSE-SENSE. *Magnetic Resonance in Medicine* 70: 64–74, 2013.

[48] Fessler, J. A. On NUFFT-based Gridding for Non-Cartesian MRI. *Journal of Magnetic Resonance* 188: 191–195, 2007.

[49] Fessler, J. A. and Sutton, B. P. Nonuniform Fast Fourier Transforms Using Min-Max Interpolation. *IEEE Transactions on Signal Processing* 51: 560–574, 2002.

[50] Gamper, U., Boesiger, P., and Kozerke, S. Compressed sensing in dynamic MRI. *Magnetic Resonance in Medicine* 59: 365–373, 2008.

[51] Ge, D., Jiang, X., and Ye, Y. A Note on the Complexity of Lp Minimization. *Mathematical Programming* 129: 285–299, 2011.

[52] Goldstein, T. and Osher, S. The Split Bregman Method for L1-Regularized Problems. *SIAM Journal on Imaging Sciences* 2: 323–343, 2009.

[53] Grist, T. M., Mistretta, C. A., Strother, C. M., and Turski, P. A. Time-Resolved Angiography : Past, Present, and Future. *Journal of Magnetic Resonance Imaging* 36: 1273–1286, 2012.

[54] Griswold, M., Walsh, D., Heidemann, R., Haase, A., and Jakob, P. The Use of an Adaptive Reconstruction for Array Coil Sensitivity Mapping and Intensity Normalization. *Proceedings of the 10th Annual Meeting of ISMRM*. Vol. 43. Honolulu, Hawai, 2002: 2410.

[55] Guralnick, W., Kaban, L., and Merrill, R. Temporomandibular-Joint Afflictions. *The New England Journal of Medicine* 299: 123–129, 1978.

[56] Haase, A., Matthaei, D., Hänicke, W., and Merboldt, K.-D. FLASH Imaging. Rapid NMR Imaging Using Low Flip-Angle Pulses. *Journal of Magnetic Resonance* 67: 258–266, 1986.

[57] Hahn, E. L. Spin Echoes. *Physical Review* 80: 580–594, 1950.

[58] Hamilton, L. H., Fabregat, J. A., Moratal, D., Ramamurthy, S., Lerakis, S., Parks, W. J., Sallee, D., and Brummer, M. E. "PINOT": Time-Resolved Parallel Magnetic Resonance Imaging with a Reduced Dynamic Field of View. *Magnetic Resonance in Medicine* 65: 1062–1074, 2011.

[59] Han, F., Zhou, Z., Rapacchi, S., Nguyen, K.-L., Finn, J. P., and Hu, P. Segmented Golden Ratio Radial Reordering with Variable Temporal Resolution for Dynamic Cardiac MRI. *Magnetic Resonance in Medicine*: doi: 10.1002/mrm.25861, 2015.

[60] Hopfgartner, A. J., Tymofiyeva, O., Ehses, P., Rottner, K., Boldt, J., Richter, E.-J., and Jakob, P. M. Dynamic MRI of the TMJ Under Physical Load. *Dentomaxillofacial Radiology* 42: doi:10.1259/dmfr.20120436, 2013.

[61] Jackson, J. I., Meyer, C. H., Nishimura, D. G., and Macovski, A. Selection of a Convolution Function for Fourier Inversion Using Gridding. *IEEE Transactions on Medical Imaging* 10: 473–478, 1991.

[62] Kaiser, J., Bradford, R., Johnson, K., Wieben, O., and Thelen, D. G. Measurement of Tibiofemoral Kinematics using Highly Accelerated 3D Radial Sampling. *Magnetic Resonance in Medicine* 69: 1310–1316, 2012.

[63] Kass, M., Witkin, A., and Terzopoulos, D. Snakes: Active Contour Models. *International Journal of Computer Vision* 1: 321–331, 1988.

[64] Kellman, P., Epstein, F. H., and Mcveigh, E. R. Adaptive Sensitivity Encoding Incorporating Temporal Filtering (TSENSE). *Magnetic Resonance in Medicine* 45: 846–852, 2001.

[65] Kim, S. G., Feng, L., Grimm, R., Freed, M., Block, K. T., Sodickson, D. K., Moy, L., and Otazo, R. Influence of Temporal Regularization and Radial Undersampling Factor on Compressed Sensing Reconstruction in Dynamic Contrast Enhanced MRI of the Breast. *Journal of Magnetic Resonance Imaging*: doi:10.1002/jmri.24961, 2015.

[66] King, K. F. and Angelos, L. SENSE Image Quality Improvement Using Matrix Regularization. *Proceedings of the 9th Annual Meeting of ISMRM*. Vol. 9. Glasgow, Scotland, 2001: 1771.

[67] King, S., Beck, F., and Lüttge, U. On the Mystery of the Golden Angle in Phyllotaxis. *Plant, Cell and Environment* 27: 685–695, 2004.

[68] Krahmer, F. and Ward, R. Stable and Robust Sampling Strategies for Compressive Imaging. *IEEE Transactions on Information Theory* 23: 612–622, 2014.

[69] Landes, C. A., Goral, W. A., Sader, R., and Mack, M. G. 3-d Sonography for Diagnosis of Disk Dislocation of the Temporomandibular Joint Compared with MRI. *Ultrasound in Medicine and Biology* 32: 633–639, 2006.

[70] Lanzer, P., Barta, C., Botvinick, E. H., Wiesendanger, H. U. D., and Higgins, C. B. ECG-Synchronized Cardiac MR Imaging: Method and Evaluation. *Radiology* 155: 681–686, 1985.

[71] Larson, A. C., White, R. D., Laub, G., Mcveigh, E. R., and Simonetti, O. P. Self-Gated Cardiac Cine MRI. *Magnetic Resonance in Medicine* 51: 93–102, 2004.

[72] Lauterbur, P. C. Image Formation by Induced Local Interactions: Examples Employing Nuclear Magnetic Resonance. *Nature* 242: 190–191, 1973.

[73] Leung, A. O., Paterson, I., and Thompson, R. B. Free-Breathing Cine MRI. *Magnetic Resonance in Medicine* 60: 709–717, 2008.

[74] Liang, Z.-P., Bammer, R., Ji, J., Pelc, N. J., and Glover, G. H. Making Better SENSE: Wavelet Denoising, Tikhonov Regularization, and Total Least Squares. *Proceedings of the 10th Annual Meeting of ISMRM*. Vol. 10. Honolulu, Hawai, 2002: 2388.

[75] Liu, B., King, K., Steckner, M., Xie, J., Sheng, J., and Ying, L. Regularized Sensitivity Encoding (SENSE) Reconstruction using Bregman Iterations. *Magnetic Resonance in Medicine* 61: 145–152, 2009.

[76] Liu, J., Spincemaille, P., Codella, N. C. F., Nguyen, T. D., Prince, M. R., and Wang, Y. Respiratory and Cardiac Self-Gated Free-Breathing Cardiac CINE imaging with Multiecho 3D Hybrid Radial SSFP Acquisition. *Magnetic Resonance in Medicine* 63: 1230–1237, 2010.

[77] Logothetis, N. K. What we can do and what we cannot do with fMRI. *Nature* 453: 869–878, 2008.

[78] Lustig, M., Santos, J. M., Donoho, D. L., and Pauly, J. M. k-t SPARSE : High Frame Rate Dynamic MRI Exploiting Spatio-Temporal Sparsity. *Proceedings of the 13th Annual Meeting of ISMRM*. 2006: 2420.

[79] Lustig, M. Sparse MRI. PhD thesis. Stanford University, 2008.

[80] Lustig, M., Donoho, D. L., Santos, J. M., and Pauly, J. M. Compressed Sensing MRI. *Signal Processing Magazine, IEEE* 25: 72–82, 2008.

[81] Lustig, M., Donoho, D., and Pauly, J. M. Sparse MRI: The Application of Compressed Sensing for Rapid MR Imaging. *Magnetic Resonance in Medicine* 58: 1182–95, 2007.

[82] Macovski, A. Volumetric NMR Imaging with Time-Varying Gradients. *Magnetic Resonance in Medicine* 2: 29–40, 1985.

[83] Madore, B., Glover, G. H., and Pelc, N. J. Unaliasing by Fourier-Encoding the Overlaps Using the Temporal Dimension (UNFOLD), Applied to Cardiac Imaging and fMRI. *Magnetic Resonance in Medicine* 42: 813–828, 1999.

[84] Maeda, A., Sano, K., and Yokoyama, T. Reconstruction by Weighted Correlation for MRI with Time-Varying Gradients. *IEEE Transactions on Medical Imaging* 7: 26–31, 1988.

[85] Manfredini, D. and Guarda-Nardini, L. Ultrasonography of the Temporomandibular Joint: a Literature Review. *International Journal of Oral and Maxillofacial Surgery* 38: 1229–1236, 2009.

[86] Marzec, C. and Kappraff, J. Properties of Maximal Spacing on a Circle Related to Phyllotaxis and to the Golden Mean. *Journal of Theoretical Biology* 103: 201–226, 1983.

[87] Nielsen, J.-F. and Nayak, K. S. Interleaved Balanced SSFP Imaging : Artifact Reduction Using Gradient Waveform Grouping. *Journal of Magneitc Resonance Imaging* 29: 745–750, 2009.

[88] Nocedal, J. and Wright, S. J. *Numerical Optimization*. Second Edition, Springer, 2006: p. 121.

[89] Noll, D. C. and Sutton, B. P. *Gridding Procedures for Non-Cartesian K-space Trajectories*. Tech. rep. University of Michigan, Dept. of Biomedial Engineering, 2006.

[90] Oppelt, A., Graumann, R., Barfuss, H., Fischer, H., Hartl, W., and Schajor, W. FISP - a New Fast MRI Sequence. *Electromedia* 54: 15–18, 1986.

[91] O'Sullivan, J. D. Fast Sinc Function Gridding Algorithm for Fourier Inversion in Computer Tomography. *IEEE Transactions on Medical Imaging* 4: 200–207, 1985.

[92] Paul, J., Divkovic, E., Wundrak, S., Bernhardt, P., Rottbauer, W., Neumann, H., and Rasche, V. High Resolution Respiratory Self-Gated Golden Angle Cardiac MRI: Comparison of Self-Gating Methods in Combination with k-t SPARSE SENSE. *Proceedings of the 22th Annual Meeting of ISMRM*. Milano, 2014: 4361.

[93] Paul, J., Divkovic, E., Wundrak, S., Bernhardt, P., Rottbauer, W., Neumann, H., and Rasche, V. High-Resolution Respiratory Self-Gated Golden Angle Cardiac MRI: Comparison of Self-Gating Methods in Combination with k-t SPARSE SENSE. *Magnetic Resonance in Medicine* 73: 292–298, 2015.

[94] Paul, J., Wundrak, S., Bernhardt, P., Rottbauer, W., Neumann, H., and Rasche, V. Self-Gated Tissue Phase Mapping Using Golden Angle Radial Sparse SENSE. *Magnetic Resonance in Medicine*: doi:10.1002/mrm.25669, 2015.

[95] Paul, J., Wundrak, S., Bernhardt, P., Rottbauer, W., Neumann, H., and Rasche, V. Self-Gated Tissue Phase Mapping using Golden Angle Radial Sparse SENSE. *Proceedings of the 23th Annual Meeting of ISMRM*. Toronto, 2015: 1052.

[96] Paul, J., Wundrak, S., Bernhardt, P., Rottbauer, W., and Rasche, V. Accelerated Radially Encoded Tissue Phase Mapping. *Journal of Cardiovascular Magnetic Resonance*. 2014: doi:10.1186/1532–429X–16–S1–W21.

[97] Paul, J., Wundrak, S., Neumann, H., and Rasche, V. Coil Array Compression for Tissue Phase Mapping. *Proceedings of the 23th Annual Meeting of ISMRM*. Toronto, 2015: 1040.

[98] Paul, J., Wundrak, S., Neumann, H., and Rasche, V. Motion-Corrected Radial Golden Angle Tissue Phase Mapping: A Phantom Study. *Proceedings of the 23th Annual Meeting of ISMRM*. Toronto, 2015: 1051.

[99] Paul, J., Wundrak, S., Neumann, H., and Rasche, V. Motion-Correction for Increase Gating Efficieny in Tissue Phase Mapping MRI. *Proceedings of the 23th Annual Meeting of ISMRM*. Toronto, 2015: 1691.

[100] Paul, J., Wundrak, S., Neumann, H., and Rasche, V. Sub-Milimeter Motion-Corrected Tissue Phase Mapping for Transmural Analysis of LV Motion. *Proceedings of the 23th Annual Meeting of ISMRM*. Toronto, 2015: 1047.

[101] Paul, J., Wundrak, S., and Rasche, V. Comparison of Inflow Effects in Cartesian and Radial Tissue Phase Mapping. *Proceedings of the 22th Annual Meeting of ISMRM*. Milano, 2014: 269.

[102] Pedersen, H., Kozerke, S., Ringgaard, S., Nehrke, K., and Kim, W. Y. k-t PCA : Temporally Constrained k-t BLAST Reconstruction Using Principal Component Analysis. *Magnetic Resonance in Medicine* 62: 706–716, 2009.

[103] Pennell, D. J. Cardiovascular Magnetic Resonance. *Circulation* 121: 692–705, 2010.

[104] Piehslinger, E., Celar, A. G., Celar, R. M., and Slavicek, R. Computerized Axiography: Principles and Methods. *Cranio* 9: 344–355, 1991.

[105] Plein, S., Bloomer, T. N., Ridgway, J. P., Jones, T. R., Bainbridge, G. J., and Sivananthan, M. U. Steady-State Free Precession Magnetic Resonance Imaging of the Heart : Comparison With Segmented K-Space Gradient-Echo Imaging. *Journal of Magneitc Resonance Imaging* 14: 230–236, 2001.

[106] Pruessmann, K. P., Weiger, M., Börnert, P., and Boesiger, P. Advances in Sensitivity Encoding with Arbitrary k-Space Trajectories. *Magnetic Resonance in Medicine* 46: 638–651, 2001.

[107] Pruessmann, K. P., Weiger, M., Scheidegger, M. B., and Boesiger, P. SENSE: Sensitivity Encoding for Fast MRI. *Magnetic Resonance in Medicine* 42: 952–962, 1999.

[108] Ramani, S. and Fessler, J. A. An Accelerated Iterative Reweighted Least Squares Algorithm for Compressed Sensing MRI. *Biomedical Imaging: From Nano to Macro, 2010 IEEE International Symposium on*. Rotterdam, 2010: 257–260.

[109] Ramani, S. and Fessler, J. A. Parallel MR Image Reconstruction Using Augmented Lagrangian Methods. *IEEE Transactions of Medical Imaging* 30: 694–706, 2011.

[110] Ramani, S. and Fessler, J. A. A Splitting-Based Iterative Algorithm for Accelerated Statistical X-Ray CT Reconstruciton. *IEEE Transactions on Medical Imaging* 31: 677–688, 2013.

[111] Rasche, V., Boer, R. de, Holz, D., and Proksa, R. Continuous Radial Data Acquisition for Dynamic MRI. *Magnetic Resonance in Medicine* 34: 754–761, 1995.

[112] Rasche, V., Proska, R., Sinkus, R., Börnert, P., and Eggers, H. Resampling of Data Between Arbitrary Grids Using Convolution Interpolation. *IEEE Transactions on Medical Imaging* 18: 385–392, 1999.

[113] Ridgway, J. P. Cardiovascular Magnetic Resonance Physics for Clinicians: Part I. *Journal of Cardiovascular Magnetic Resonance* 12: doi:10.1186/1532–429X–12–71, 2010.

[114] Scheffler, K. and Lehnhardt, S. Principles and applications of balanced SSFP techniques. *European Radiology* 13: 2409–2418, 2003.

[115] Schmid-Schwap, M., Bristela, M., Pittschieler, E., Skolka, A., Szomolanyi, P., Weber, M., Piehslinger, E., and Trattnig, S. Biochemical Analysis of the Articular Disc of the Temporomandibular Joint with Magnetic Resonance T2 Mapping: a Feasibility Study. *Clinical Oral Investigations* 18: 1865–1871, 2013.

[116] Schomberg, H. and Timmer, J. The Gridding Method for Image Reconstruction by Fourier Transformation. *IEEE Transactions on Medical Imaging* 14: 596–607, 1995.

[117] Scott, A. D., Boubertakh, R., Birch, M. J., and Miquel, M. E. Adaptive Averaging Applied to Dynamic Imaging of the Soft Palate. *Magnetic Resonance in Medicine* 70: 865–874, 2013.

[118] Scrivani, S. J., Keith, D. A., and Kaban, L. B. Temporomandibular Disorders. *The New England Journal of Medicine* 359: 2693–2705, 2008.

[119] Selvanayagam, J. B., Robson, M. D., Francis, J. M., and Neubauer, S. Cardiovascular Magnetic Resonance: Basic Principles Methods and Techniques. *Cardiac CT, PET and MR, Second Edition*. Ed. by Vasken Dilsizian, G. M. P. 2010: 30–71.

[120] Sha, L., Guo, H., and Song, A. W. An Improved Gridding Method for Spiral MRI using Nonuniform Fast Fourier transform. *Journal of Magnetic Resonance* 162: 250–258, 2003.

[121] Shannon, C. E. Communication in the Presence of Noise. *Proceedings of the IEEE* 86: 447–457, 1998.

[122] Shimazaki, Y., Saito, K., Matsukawa, S., Onizawa, R., Kotake, F., Nishio, R., and Abe, K. Image Quality Using Dynamic MR Imaging of the Temporomandibular Joint with True-FISP Sequence. *Magnetic Resonance in Medical Science* 6: 15–20, 2007.

[123] Slichter, C. *Principles of Magnetic Resonance Imaging*. Berlin: Third Edition, Springer, 1990: p. 19.

[124] Solberg, W. K., Woo, M. W., and Houston, J. B. Prevalence of Mandibular Dysfunction in Young Adults. *The Journal of the American Dental Association* 98: 25–34, 1979.

[125] Song, H. K. and Dougherty, L. k-Space Weighted Image Contrast (KWIC) for Contrast Manipulation in Projection Reconstruction MRI. *Magnetic Resonance in Medicine* 44: 825–832, 2000.

[126] Speier, P. and Hansen, M. S. A Golden Angle of 68.75° Improves Gradient Spoiling in Radial GRE. *Proceedings of the 22th Annual Meeting of ISMRM*. Milano, 2014: 4245.

[127] Spraggins, T. A. Wireless Retrospective Gating: Application to Cine Cardiac Imaging. *Magnetic Resonance Imaging* 8: 675–681, 1990.

[128] Taubman, D. S. and Marcellin, M. *Jpeg2000 Image Compression Fundamentals, Standards and Practice*. Kluwer International Series in Engineering & Computer Science, 2001.

[129] Tibiletti, M., Paul, J., Bianchi, A., Wundrak, S., Rottbauer, W., Stiller, D., and Rasche, V. Multi-Stage Three-Dimensional UTE Lung Imaging by Image-Based Self-Gating. *Proceedings of the 23th Annual Meeting of ISMRM*. Toronto, 2015: 1475.

[130] Tibiletti, M., Paul, J., Bianchi, A., Wundrak, S., Rottbauer, W., Stiller, D., and Rasche, V. Multistage Three-Dimensional UTE Lung Imaging by Image-Based Self-Gating. *Magnetic Resonance in Medicine*: doi:10.1002/mrm.25673, 2015.

[131] Tikhonov, A., Goncharsky, A., Stepanov, V., and Yagola, A. *Numerical Methods for the Solution of Ill-Posed Problems*. Berlin: Springer, 1995.

[132] Tsao, J., Boesiger, P., and Pruessmann, K. P. k-t BLAST and k-t SENSE : Dynamic MRI With High Frame Rate Exploiting Spatiotemporal Correlations. *Magnetic Resonance in Medicine* 50: 1031–1042, 2003.

[133] Uecker, M., Hohage, T., Block, K. T., and Frahm, J. Image Reconstruction by Regularized Nonlinear Inversion - Joint Estimation of Coil Sensitivities and Image Content. *Magnetic Resonance in Medicine* 60: 674–682, 2008.

[134] Uecker, M., Lai, P., Murphy, M. J., Virtue, P., Elad, M., Pauly, J. M., Vasanawala, S. S., and Lustig, M. ESPIRiT – An Eigenvalue Approach to Autocalibrating Parallel MRI : Where SENSE meets GRAPPA. *Magnetic Resonance in Medicine* 71: 990–1001, 2012.

[135] Uecker, M., Zhang, S., Voit, D., Karaus, A., Merboldt, K.-D., and Frahm, J. Real-Time MRI at a Resolution of 20 ms. *NMR in Biomedicine* 23: 986–994, 2010.

[136] Usman, M., Atkinson, D., Odille, F., Kolbitsch, C., Vaillant, G., Schaeffter, T., Batchelor, P. G., and Prieto, C. Motion Corrected Compressed Sensing for Free-Breathing Dynamic Cardiac MRI. *Magnetic Resonance in Medicine* 70: 504–516, 2013.

[137] Vemuri, P., Kholmovski, E. G., Parker, D. L., and Chapman, B. E. Coil Sensitivity Estimation for Optimal SNR Reconstruction and Intensity Inhomogeneity Correction in Phased Array MR Imaging. *Information Processing in Medical Imaging* 19: 603–614, 2005.

[138] Ventura, S. M. R. Towards Dynamic Magnetic Resonance Imaging of the Vocal Tract during Speech Production. *Journal of Voice* 24: 511–518, 2011.

[139] Voit, D., Zhang, S., Unterberg-Buchwald, C., Sohns, J. M., Lotz, J., and Frahm, J. Real-time cardiovascular magnetic resonance at 1.5 T using balanced SSFP and 40 ms resolution. *Journal of cardiovascular magnetic resonance* 15: doi:10.1186/1532–429X–15–79, 2013.

[140] Wang, E. Y., Mulholland, T. P., Pramanik, B. K., Nusbaum, A. O., Babb, J., Pavone, A. G., and Fleisher, K. E. Dynamic Sagittal Half-Fourier Acquired Single-Shot Turbo Spin-Echo MR Imaging of the Temporomandibular joint: Initial Experience and Comparison with Sagittal Oblique Proton-Attenuation Images. *American Journal of Neuroradiology* 28: 1126–1132, 2007.

[141] Wang, E. Y. and Fleisher, K. A. MRI of Temporomandibular Joint Disorders. *Applied Radiology* 37: 17–25, 2008.

[142] Wikipedia and Contributors. *Overview of Generalized Tikhonov Regularization.* 2015. URL: `https://en.wikipedia.org/wiki/Tikhonov%5C_regularization` (visited on 10/01/2015).

[143] Winkelmann, S., Schaeffter, T., Eggers, H., Nielsen, T., and Doessel, O. Single Shot T1-Mapping, using a Radial Look-Locker Sequence and an Optimal Profile Order Determined by the Golden Cut. *Proceedings of the 13th Annual Meeting of ISMRM.* Miami, 2005: 2196.

[144] Winkelmann, S., Schaeffter, T., Koehler, T., Eggers, H., and Doessel, O. An Optimal Radial Profile Order Based on the Golden Ratio for Time-Resolved MRI. *IEEE Transactions on Medical Imaging* 26: 68–76, 2007.

[145] Wissmann, L., Santelli, C., Segars, W. P., and Kozerke, S. MRXCAT: Realistic numerical phantoms for cardiovascular magnetic resonance. *Journal of cardiovascular magnetic resonance* 16: 2–11, 2014.

[146] Wundrak, S., Paul, J., Ulrici, J., Hell, E., Geibel, M.-A., Bernhardt, P., Rottbauer, W., and Rasche, V. A Self-Gating Method for Time-Resolved Imaging of Nonuniform Motion. *Magnetic Resonance in Medicine*: doi:10.1002/mrm.26000, 2015.

[147] Wundrak, S., Paul, J., Ulrici, J., Hell, E., Geibel, M.-A., Bernhardt, P., Rottbauer, W., and Rasche, V. Golden Ratio Sparse MRI Using Tiny Golden Angles. *Magnetic Resonance in Medicine*: doi:10.1002/mrm.25831, 2015.

[148] Wundrak, S., Paul, J., Ulrici, J., Hell, E., Geibel, M.-A., and Rasche, V. MRI of the moving TMJ using Contour Fitting in the Correlation Matrix (CoFi-CoMa). *Proceedings of the 23th Annual Meeting of ISMRM.* Toronto, 2015: 2085.

[149] Wundrak, S., Paul, J., Ulrici, J., Hell, E., Kozerke, S., and Rasche, V. Sparse Dynamic MRI with an Adaptive Temporal Sparsity Prior for Cardiovascular Imaging. *Proceedings of the 22th Annual Meeting of ISMRM*. Milano, 2014: 4384.

[150] Wundrak, S., Paul, J., Ulrici, J., Hell, E., and Rasche, V. Retrospective Self-Gated MRI of the TMJ Dynamics During Mastication. *Proceedings of the 21th Annual Meeting of ISMRM*. Salt Lake City, 2013: 3837.

[151] Wundrak, S., Paul, J., Ulrici, J., Hell, E., and Rasche, V. Does Temporal Regularization Lead to Systematic Underestimation of Ejection Fraction? *Proceedings of the 22th Annual Meeting of ISMRM*. Milano, 2014: 4380.

[152] Wundrak, S., Paul, J., Ulrici, J., Hell, E., and Rasche, V. Sparse Dynamic MRI of the Temporomandibular Joint. *Proceedings of the 22th Annual Meeting of ISMRM*. Milano, 2014: 1267.

[153] Wundrak, S., Paul, J., Ulrici, J., Hell, E., and Rasche, V. A Small Surrogate for the Golden Angle in Time-Resolved Radial MRI Based on Generalized Fibonacci Sequences. *IEEE Transactions on Medical Imaging* 34: 1262–1269, 2015.

[154] Wundrak, S., Paul, J., Ulrici, J., Hell, E., and Rasche, V. Tiny Golden Angles: A Small Surrogate for the Radial Golden Angle Profile Order. *Proceedings of the 23th Annual Meeting of ISMRM*. Toronoto, 2015: 2083.

[155] Xu, D., King, K. F., and Liang, Z.-P. Improving k - t SENSE by Adaptive Regularization. *Magnetic Resonance in Medicine* 57: 918–930, 2007.

[156] Ying, L. and Sheng, J. Joint Image Reconstruction and Sensitivity Estimation in SENSE (JSENSE). *Magnetic Resonance in Medicine* 57: 1196–1202, 2007.

[157] Zhang, S., Gersdorff, N., and Frahm, J. Real-Time Magnetic Resonance Imaging of Temporomandibular Joint Dynamics. *The Open Medical Imaging Journal* 5: 1–9, 2011.

[158] Zhang, S., Uecker, M., Voit, D., Merboldt, K.-D., and Frahm, J. Real-Time Cardiovascular Magnetic Resonance at High Temporal Resolution: Radial FLASH with Nonlinear Inverse Reconstruction. *Journal of Cardiovascular Magnetic Resonance* 12: doi:10.1186/1532–429X–12–39, 2010.

List of Figures

List of Tables

Acknowledgments

I would like to express my sincere gratitude to my supervisor Prof. Volker Rasche for the outstanding support of my research. I could not imagine a better advisor during the last years. His doors were always open when I ran into trouble and he would always pause whatever he was doing for a challenging MR problem.

I am very thankful to Dr. Erich Hell and Dr. Johannes Ulrici for the great support of my research at Sirona Dental Systems.

Many thanks to Prof. Margrit-Ann Geibel, for patient guidance and sharing her knowledge about temporomandibular joint dysfunctions with me.

Many thanks to Jan Paul for fruitful discussions on image reconstruction and for congenial hacking session. Many thanks also to Anna-Katinka Bracher who wrote the initial version of our reconstruction framework.

Thank you to all colleagues at the ExCaVI group at the Ulm University Hospital who received me warmhearted in their group. Thank you Michael Eder, Daniel Kammer, Anne Subgang, Marta Tibiletti, Ina Vernikouskaya, Alireza Abaei, Zuo Zhi, Anna-Katinka Bracher, and Jan Paul.

Thank you to all my colleagues at Sirona in Bensheim for creating such a great working environment. Many thanks to Jakob Schluttig, Michael Elvers, Kai Stannigel, and Kai Lindenberg for showing interest in MRI during our daily coffee breaks.

Also I would like to thank my old friends and fellow students Björn, Thomas, Moritz and Frank who are a constant source of inspiration since a long time.

Many thanks to my mother and father for introducing me to computers and science early.

Most of all I would like to thank my wonderful wife Nadine and my three children Hanna-Lotta, Marie and Ida for their patience, love, and for always getting my focus back to the things that matter.

List of Related Publications

Journal Contributions

1. Wundrak, S., Paul, J., Ulrici, J., Hell, E., and Rasche, V. A Small Surrogate for the Golden Angle in Time-Resolved Radial MRI Based on Generalized Fibonacci Sequences. *IEEE Transactions on Medical Imaging* 34.: 1262–1269, 2015

2. Wundrak, S., Paul, J., Ulrici, J., Hell, E., Geibel, M.-A., Bernhardt, P., Rottbauer, W., and Rasche, V. Golden Ratio Sparse MRI Using Tiny Golden Angles. *Magnetic Resonance in Medicine*: doi:10.1002/mrm.25831, 2015

3. Wundrak, S., Paul, J., Ulrici, J., Hell, E., Geibel, M.-A., Bernhardt, P., Rottbauer, W., and Rasche, V. A Self-Gating Method for Time-Resolved Imaging of Nonuniform Motion. *Magnetic Resonance in Medicine*: doi:10.1002/mrm.26000, 2015

4. Paul, J., Divkovic, E., Wundrak, S., Bernhardt, P., Rottbauer, W., Neumann, H., and Rasche, V. High-Resolution Respiratory Self-Gated Golden Angle Cardiac MRI: Comparison of Self-Gating Methods in Combination with k-t SPARSE SENSE. *Magnetic Resonance in Medicine* 73: 292–298, 2015

5. Paul, J., Wundrak, S., Bernhardt, P., Rottbauer, W., Neumann, H., and Rasche, V. Self-Gated Tissue Phase Mapping Using Golden Angle Radial Sparse SENSE. *Magnetic Resonance in Medicine*: doi:10.1002/mrm.25669, 2015

6. Tibiletti, M., Paul, J., Bianchi, A., Wundrak, S., Rottbauer, W., Stiller, D., and

Rasche, V. Multistage Three-Dimensional UTE Lung Imaging by Image-Based Self-Gating. *Magnetic Resonance in Medicine*: doi:10.1002/mrm.25673, 2015

Conference Contributions

1. Wundrak, S., Paul, J., Ulrici, J., Hell, E., and Rasche, V. Retrospective Self-Gated MRI of the TMJ Dynamics During Mastication. *Proceedings of the 21th Annual Meeting of ISMRM*. Salt Lake City, 2013: 3837

2. Wundrak, S., Paul, J., Ulrici, J., Hell, E., Kozerke, S., and Rasche, V. Sparse Dynamic MRI with an Adaptive Temporal Sparsity Prior for Cardiovascular Imaging. *Proceedings of the 22th Annual Meeting of ISMRM*. Milano, 2014: 4384

3. Wundrak, S., Paul, J., Ulrici, J., Hell, E., and Rasche, V. Does Temporal Regularization Lead to Systematic Underestimation of Ejection Fraction? *Proceedings of the 22th Annual Meeting of ISMRM*. Milano, 2014: 4380

4. Wundrak, S., Paul, J., Ulrici, J., Hell, E., and Rasche, V. Sparse Dynamic MRI of the Temporomandibular Joint. *Proceedings of the 22th Annual Meeting of ISMRM*. Milano, 2014: 1267

5. Paul, J., Wundrak, S., and Rasche, V. Comparison of Inflow Effects in Cartesian and Radial Tissue Phase Mapping. *Proceedings of the 22th Annual Meeting of ISMRM*. Milano, 2014: 269

6. Paul, J., Divkovic, E., Wundrak, S., Bernhardt, P., Rottbauer, W., Neumann, H., and Rasche, V. High Resolution Respiratory Self-Gated Golden Angle Cardiac MRI: Comparison of Self-Gating Methods in Combination with k-t SPARSE SENSE. *Proceedings of the 22th Annual Meeting of ISMRM*. Milano, 2014: 4361

7. Paul, J., Wundrak, S., Bernhardt, P., Rottbauer, W., and Rasche, V. Accelerated Radially Encoded Tissue Phase Mapping. *Journal of Cardiovascular Magnetic Resonance*. 2014: doi:10.1186/1532–429X–16–S1–W21

8. Wundrak, S., Paul, J., Ulrici, J., Hell, E., and Rasche, V. Tiny Golden Angles: A Small Surrogate for the Radial Golden Angle Profile Order. *Proceedings of the 23th Annual Meeting of ISMRM*. Toronoto, 2015: 2083

9. Wundrak, S., Paul, J., Ulrici, J., Hell, E., Geibel, M.-A., and Rasche, V. MRI of the moving TMJ using Contour Fitting in the Correlation Matrix (CoFi-CoMa). *Proceedings of the 23th Annual Meeting of ISMRM*. Toronto, 2015: 2085

10. Paul, J., Wundrak, S., Neumann, H., and Rasche, V. Motion-Corrected Radial Golden Angle Tissue Phase Mapping: A Phantom Study. *Proceedings of the 23th Annual Meeting of ISMRM*. Toronto, 2015: 1051

11. Paul, J., Wundrak, S., Neumann, H., and Rasche, V. Sub-Milimeter Motion-Corrected Tissue Phase Mapping for Transmural Analysis of LV Motion. *Proceedings of the 23th Annual Meeting of ISMRM*. Toronto, 2015: 1047

12. Paul, J., Wundrak, S., Neumann, H., and Rasche, V. Coil Array Compression for Tissue Phase Mapping. *Proceedings of the 23th Annual Meeting of ISMRM*. Toronto, 2015: 1040

13. Paul, J., Wundrak, S., Neumann, H., and Rasche, V. Motion-Correction for Increase Gating Efficieny in Tissue Phase Mapping MRI. *Proceedings of the 23th Annual Meeting of ISMRM*. Toronto, 2015: 1691

14. Paul, J., Wundrak, S., Bernhardt, P., Rottbauer, W., Neumann, H., and Rasche, V. Self-Gated Tissue Phase Mapping using Golden Angle Radial Sparse SENSE. *Proceedings of the 23th Annual Meeting of ISMRM*. Toronto, 2015: 1052

15. Tibiletti, M., Paul, J., Bianchi, A., Wundrak, S., Rottbauer, W., Stiller, D., and Rasche, V. Multi-Stage Three-Dimensional UTE Lung Imaging by Image-Based Self-Gating. *Proceedings of the 23th Annual Meeting of ISMRM*. Toronto, 2015: 1475

Curriculum Vitae

The curriculum vitae has been removed due to data privacy protection.